Design of a Marine Wireless Sensor Network for Seawater Quality Monitoring

Department of Electrical and Information Engineering
Electrical and Information Engineering
Ph.D. Program
SSD: ING-INF/07– Electric and electronic measurements

Final Dissertation

Design of a Marine Wireless Sensor Network for Seawater Quality Monitoring

---

by
Carlo Guarnieri Calò Carducci

Referees:

Prof. Roberto Ferrero

Prof. José Juan Santana Rodríguez

Supervisors:

Prof. Filippo Attivissimo

Coordinator of Ph.D Program:

Prof. Vittorio M. N. Passaro

XXIX cycle, 2014-2016

ABSTRACT

A solid investigation of all the building blocks of a versatile Wireless Sensor Network for seawater monitoring applications is presented in this thesis.

The discussed framework, based on buoys for real-time monitoring of seawater, is intended to be an extension of the classical CTD probes, used for measuring the water conductivity, temperature and depth, and usually equipped with additional instrumentation for measuring the chlorophyll-*a* concentration and water turbidity. This additional instrumentation is usually very expensive and thus de facto has prevented the realization of a wide network of measuring unit. Starting from this assumption and in line with the Italian regulations in this area, the author proposes a new cheap module for in-vivo detection of chlorophyll-*a*.

The implementation the aforementioned sensor also requested the implementation of a novel circuit design technique, used to give a full symbolical representation of the circuit, which is then numerically simulated for millions of different combinations of the design parameters in a small time. The computation of a figure of merit thus leads to choose the most appropriate combination of adopted passive components.

The author also present two novel techniques: the first for power consumption characterization of WSN modules, which are usually subjected to high dynamic current variations and the second for the characterization of thermoelectric modules that are intended to be used to provide energy self-sufficiency in cogeneration with solar panel.

The author would link to thank Prof. F. Attivissimo for its support during the course and for supervising this thesis work.

TABLE OF CONTENTS

Chapter I
INTRODUCTION

The research activity described in this thesis has been focused on creating the basis of a long-term research topic in marine monitoring systems, which are of strategic interest for the development of southern regions of the Italian peninsula, where economic activities are often strictly connected to the sea coast.

Underestimating the importance of monitoring the seawater quality, may in fact lead to unexpected critical issues that may manifest as toxic algae blooms or other phenomena more generally connected to eutrophication. These may constitute a direct risk to human safety, both for bathers and for workers, as well as may interfere with commercial activities, especially those based on fishery, resulting in potential economic losses.

The implementation of such a monitoring system would help the local administration in prevent such critical issues, but requires to front many technological challenges connected to the acquisition of a wide technical knowledge that belongs to different

academic topics. These range from the applied physical measurement principles and signal processing algorithms, to the design of the required hardware and firmware both for sensor frontends and for system embedded electronics. Furthermore, it is necessary to grant an energy self-sufficiency to measuring units and to develop the network architectures as well as related communication standards.

Of course, all these building blocks cannot be implemented separately because they are often strictly interdependent, hence what is provided within this work is a first design of the entire system, which should then be test and eventually redesigned.

The Mediterranean Sea has always been an important resource for many European populations; today more than ever it is a richness in terms of marine and agricultural biodiversity and, especially in Italy, an attraction for a kind of tourists more and more demanding with specific requests. With this premises, it becomes necessary to implement a Europe-wide shared environmental policy able to cope with the ongoing climate change, with the overexploitation of natural resources and with the increase of pollution sources. With a view to safeguarding natural marine resources and to preserving biodiversity, the discharge of substances that promote eutrophication is considered a serious problem for the marine ecosystem so that its reduction is considered a strategic objective for the Community EU [1].

This thesis presents a network of smart buoy for seawater quality monitoring. In particular, the system design has been focused around the measurement of the only biological indicator recognized both in Italian and in European legislation at the present day, i.e. the density of chlorophyll-*a* inside micro algae

[1] The European Union Water Framework Directive: Integrated River Basin Management for Europe, WFD 2000/60/IEC

(phytoplankton), which can provide information regarding the trophic status of sea water.

Although measuring the chlorophyll-*a* concentration through fluorescence-based techniques do not result an innovative subject, such practice has generally required a significant effort in terms of economic and human capital, because of the use of considerably expensive instrumentation and for the necessity of highly specialized technicians that generally collect data manually through monitoring campaigns. Among other things, this task usually burdens on the economic resources of each region which are in charge of financing local Regional Agencies for the Environment (ARPA). The latter, have the daunting and often unattainable task of creating complex and expensive systems for the collection of data disposing only of few funds. This leads to a less attention paid to the marine monitoring and thus to a consequent increase in the number of not sufficiently monitored pollution sources with potential economic impact on commercial activities and on the healthcare system.

While the technological evolution of the instrumentation and measurement methodologies now offers several alternatives to the traditionally used techniques, such as the measurement of certain parameters using satellites via remote sensing techniques, on the other hand these are still rather limited by the attainable spatial resolution. In this context, the European project known as the Copernicus Programme, is a cutting-edge solution in remote measurement techniques and the use of the acquired satellite data is an obvious choice since users are provided with free, full and open access to environmental data, some of which are available after only three hours from the acquisition in the so-called near real-time. However, in the case of chlorophyll-*a* detection, the maximum resolution attainable from the Sentinel-3A satellite

(launched in February of this year) is of 300 m. Though remarkable it is, it still clashes with the non-uniformity of distribution of chlorophyll in the seawater, which is known to be affected by the phenomenon of spatial patchiness, i.e. its manifestation in spots of high concentrations on scales of a few tens of meters.

It is therefore necessary to combine these large-scale data surveying systems with sensor networks that employ cheaper instruments, able to carry out a more capillary monitoring of the territory and to provide more immediate response times.

Given the depicted background and to better define the project goals, the research concerned primarily with the study of the existing legislation and of environmental issues; subsequently, the requested network topology and related standards for the proposed sensors network were investigated.

Hence, a prototype concept is presented with a special focus on the design, the implementation and the electronics improvements, derived from different researches, of the sensor front-end for the measurement of chlorophyll-*a* density and seawater turbidity. Afterwards, a study of power consumptions for the proposed device is presented as wells as a preliminary study of energy harvesting systems for energy self-sufficiency.

Finally, an adequate metrological characterization of the measurement front-end is given through the presented experimental validation.

Chapter II
REGULATORY REQUIREMENTS AND ENVIRONMENTAL ISSUES

Today's regulations applying to monitoring the health state of aquatic ecosystems, separately address the different types of aquatic environments, according basically to whatever they are salty or fresh waters and imposing the use of different tools suitable for a given context. For instance, in the case of transitional waters, or fluvial environments or furthermore for the simple oxygen and dissolved nutrients evaluation, the generally adopted index is the $TRIX$

$$TRIX = \frac{\log_{10}(Chl_A \cdot DO_{\%} \cdot N_{min} \cdot TP) + a}{b} \quad (1)$$

where:

- Chl_A is the chlorophyll-a concentration in water (due to phytoplankton) in µg/l

- $DO_{\%}$ is the oxygen in terms of absolute percentage deviation from the saturation value
- $N_{\%}$ is mineral nitrogen, otherwise known with the acronym DIN (Dissolved Inorganic Nitrogen) in $\mu g/l$
- TP is the total phosphorus in $\mu g/l$
- a and b are determined on the basis of experimental data (e.g. for the Northern Adriatic Sea $a = 1.5, b = 1.2$)

It is important to underline that this index was adopted in 2003 by the UNEP-MEDPOL (United Nations Environment Programme) for the trophic classification of coastal waters and is used in several areas of the Mediterranean Sea prone to eutrophic risk [2].

However, due to the low eutrophication risk of Italian seawaters, the phytoplankton concentration limits in aquatic environments are defined in Italian regulations by the Ministerial Decree 260/2010 of 8 November, which explicitly states that: "The phytoplankton concentration is evaluated through the 'chlorophyll-*a*' parameter, which has been chosen as the biomass indicator and is measured on the water surface. It is therefore necessary to refer not only to the ecological quality ratios (RQE) but also to the absolute values of chlorophyll-*a* concentration, expressed in mg/m^3." The Annex table 4.3.1 of the aforementioned decree [3] is reported below and shows the value 2.4 mg/m^3 as the classification limit for 'High/Good' class and the value 3.5 mg/m^3 as the limit for the 'Good/Fair' one.

---

2 Review of the methods, criteria and limit values for the assessment of Eutrophication as developed in the framework of the Intercalibration Exercise of the MED GIG Water Framework Directive 2000/60 EC, UNEP(DEPI)/MED WG.365/Inf.7, 4 November 2011, p. 29

3 Decreto Ministeriale 260/2010, Tabella 4.3.1: www.reteambiente.it/repository/normativa/14566all1_2.pdf

Macrotype	Reference value (mg/m^3)	Class limits				Metric
		High/Good		Good/Sufficient		
		(mg/m^3)	RQE	(mg/m^3)	RQE	
1 (high stability)	1,8	2,4	0,75	3,5	0,51	Geometric mean
2 (medium stability)	1,9	2,4	0,80	3,6	0,53	90th Percentile
3 (low stability)	0,9	1,1	0,80	1,8	0,50	90th Percentile

Fig. 1 – Class Limit Table 4.3.1/a (D.M. 260/2010)

These values are significant for designing purposes, since they give an indication about the performance that the sensor should have, but it's also worthwhile to understand the reason why the chlorophyll-*a* concentration is so important and what are the reasons for its variability.

It is in fact contained inside the micro-algae, or phytoplankton, that are the base of the food chain in the vast majority of aquatic ecosystems, feeding zooplankton, which feeds more complex life forms such as fish, which are in turn the food base of billions of human individuals. But the phytoplankton is equally, if not more important for the fact that it produces about half the total oxygen produced by plant organisms on Earth.

Phytoplankton is in fact defined as the set of autotrophic photosynthetic organisms present in the plankton, i.e. all those organisms capable of using the solar radiation as a source of energy for synthesizing organic matter from low dissolved inorganic substances. Thanks to chlorophyll, these organisms use a pair of photons to split a water molecule and, thanks to carbon dioxide, they generate glucose for their own growth and oxygen as a waste substance.

$$CO_2 + H_2O \rightarrow C_6H_{12}O_6 + O_2 \quad (2)$$

In some occasions these organisms may manifest as phytoplankton blooms, micro-algal blooms, toxic algae, red tides, or harmful

algae, which are all terms for naturally occurring phenomena, but often connected to human activities. These are caused by a release of high concentrations of nitrogen and phosphorus salts in the seawaters, which further promote an abnormal development of the number of microalgae normally present, which can also reach millions of cells per liter. Although this condition is necessary, however, it is not sufficient for occurring a bloom. Beside the presence of nutrients, stable marine conditions are required, characterized by weak currents and the absence of waves. In fact, in presence of waves that disperse the nutrients, the chances of blooms would collapse.

When the effects of climate change add up to more and more marked anthropogenic ones on the surrounding environment, the consequences can be unpredictable and dangerous, requiring an ever-increasing ability to face the changes.

A very interesting case concerns the spread of a non-native toxic alga with tropical origin in the Apulian seas, known as Ostreopsis Ovata, which first appearance goes back to the early 2000. Its appearance is most likely due to the ballast water of cargo-ships coming from other areas of the globe, while its spread was definitely favored by global warming and is closely correlated with fertilizers used in agriculture that promote their growth reaching the sea via the sewage system or due to rains.

During flowering spikes, known as blooms, these micro-algae can cause considerable damages both to the marine ecosystem, causing anoxia and indiscriminate kills of marine life, and to humans and related commercial activities, with economic impact on the health-care system and local economies.

However, the efforts made by the regional agency for environment (ARPA Puglia) in monitoring twenty sampling spot (Fig. 2)

around the 800 km of the coast of the Apulia region, are not sufficient to prevent highly critical situations, as happened in the early summer of 2014 (Fig. 3).

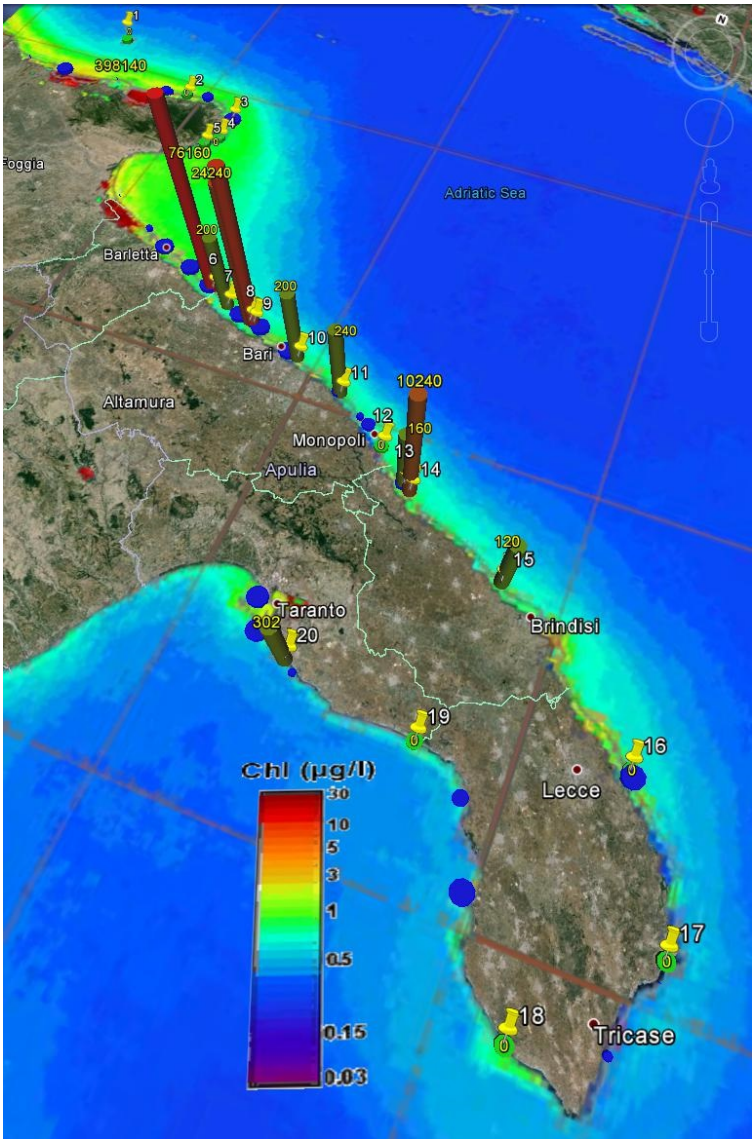

Fig. 2 - Different data superimposed on Apulia region Sat image: yellow place marks are the sampling spots; columns relate to concentration in Fig. 3; blue disks are wastewater treatment plants (size is proportional to the number of served inhabitants); remote image of chlorophyll-*a* concentration in color map (MERIS/MODIS A 2006/2011).

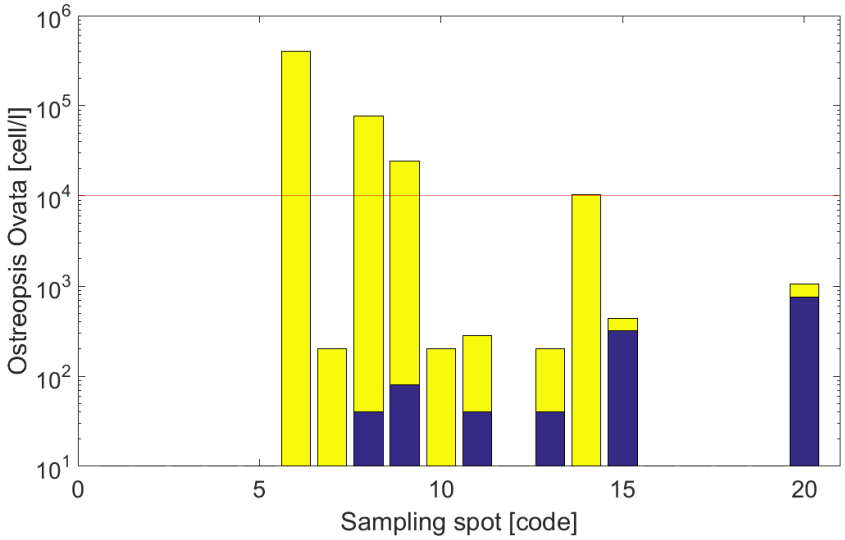

Fig. 3 - Ostreopsis Ovata concentration in the water column: first (blue) and second (yellow) fortnight of June 2014 and risk limit (red)

These micro-algae can in fact achieve the maturation in just ten days under favorable conditions, and the adopted twice-weekly sampling plan was unable to anticipate and/or predict the micro-algal bloom. This resulted in many people reporting effects such as fever, pharyngitis, cough, difficulty in breathing, headache, cold, lacrimation, dermatitis, nausea and vomiting [4], adding up to damages to the fisheries sector. Since these micro-algae are the basis of the food chain, they contaminate the seafood with toxins that accumulate and makes non-edible and even dangerous to eat all those organisms that live on the seabed and feed on algae.

The aforementioned event is by no means an isolated case. Analyzing the data provided by ARPA [5], it appears that during the four months of June to September of the years 2011 to 2016,

4 http://www.lagazzettadelmezzogiorno.it/news/home/568591/-litorale-barese--l-alga-tossica-fa-gia-prime-vittime.html

5 A.R.P.A. Puglia, Monitoraggio Ostreopsis: http://www.arpa.puglia.it/web/guest/monitoraggiostreopsis

there have been as many as 47 events of risk limit concentration exceeding 10,000 cells per liter.

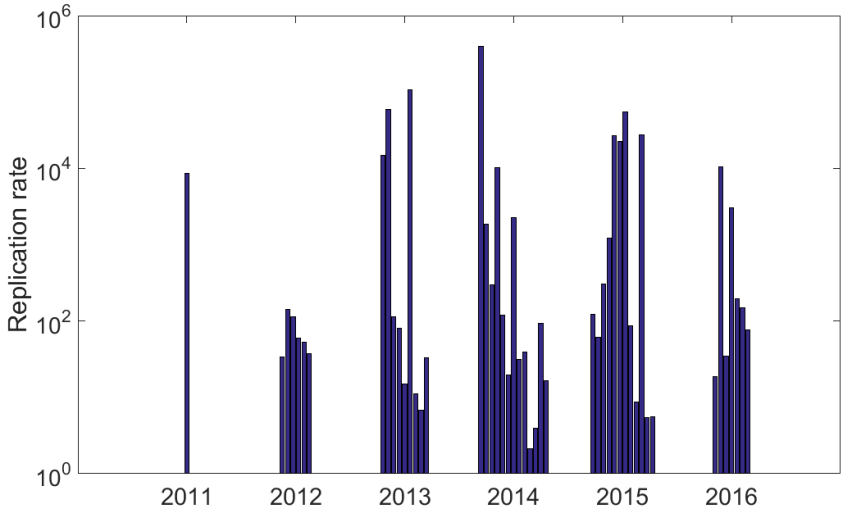

Fig. 4 – Risk limit threshold exceeding events

The reported micro-algae replication rate (Fig. 4) after a fortnight (as ratio post/pre-bloom), goes from a minimum value of 2 that makes the bloom not unexpected to approximately $4 \cdot 10^5$, making it largely unpredictable. Certainly, the agency operates to the edge of its capabilities both in economic terms and in technological ones. In fact, it should be pointed out that the typically required equipment for this type of measure (CTD probe and fluorimeter), may costs several thousand euro and it must be manually brought to the sampling point by an experienced operator, requiring the use of a dedicated boat, thus resulting in the inability to organize simultaneous measurement campaigns.

Considering that the Apulian coastline extends approximately for 800 km as stated above, it appears clear how onerous and time consuming is its monitoring with the described procedure.

Besides these biological forms of pollution, Apulia region is also affected by chemical pollution caused by leaks of toxic substances from different localized sources: wide coastal urban areas with a mean distance of 11 km between villages, great industrial plants along the coast such as ILVA in Taranto (the largest steelworks in Europe) and maritime transport.

The study of the substances released by the different industrial sectors together with their hazardous nature allowed identifying the following ones as the most polluting types of industry:

- Energy production
- Metal industry
- Manufacture of cement
- Oil refining
- Treatment of urban wastewater
- Chemical industry
- Manufacture of fertilizers.

Taranto city (Fig. 5) is a case in point of industry located along the Apulia region coasts in areas with high population density, almost within the urban center and in close proximity to other economic activities like agriculture and tourism. It is affected by many different water pollutants derived from industries, like Hg, Zn, Pb and PCBs and BAPs, which settle in neighbor areas used for mussel farming, and also waste waters containing high level of Escherichia Coli due to inefficient purification systems, resulting in a direct health risk for the population.

This means that pressures brought by industry to coastal and marine environments add to and interact with other types of pressures. The environmental pressures on the Mediterranean coastal marine ecosystem generated by this broad range of industrial activities are multiple and varied, including the use of

territory and natural resources (both marine and non-marine), the generation of waste waters and the release of pollutants into the atmosphere and water bodies.

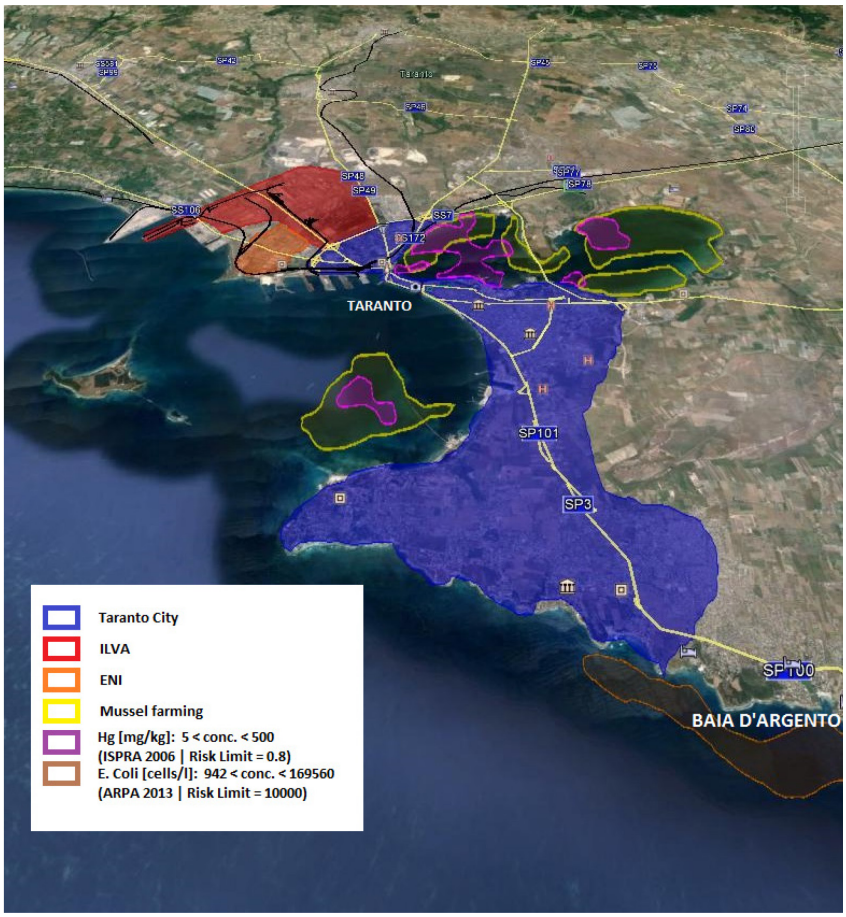

Fig. 5 Taranto map of main pollutants and sources of pollution

Furthermore, it should not be overlooked the impact of the tourism. In fact, as reported as Priority 5 in the national strategic Plan (2007) and in regional documents under Priority Axis 4 in the ERDF Operational Programme (Enhancement of natural and cultural resources for attraction and development), it is expected that the current region growth can achieve an even greater extent in the near future, under the pressure of development plans shared

with the Organization for Economic Co-operation and Development (OECD) [6], also known as OCSE, and thanks to the efforts of European Union funds (ERDF).

Today in fact, the OECD states that the traditional position of Apulia based on medium-quality beach tourism, may constitute a limit to further tourism growth, because of increased international competition with other Mediterranean countries. It believes that it is essential for Apulia to improve its beach holiday tourism offer as well as other forms of tourism but also considering environmental problems arising due to people visit from other regions and from other countries that can thus put more stress on the local services, especially when tourism is concentrated on a narrow peak season. But this situation still presents a positive side, consisting in a clear booster effect which would accelerate a range of projects that are likely to directly serve the local people, including projects that had previously been regarded as difficult to justify or carry out.

To overcome the above described limitations and taking advantage of the depicted scenario, this research aim to investigate the possibility of implementing an automatic and distributed monitoring system, based on a network of low cost sensor buoys for the collection and remote transmission of those parameters useful to monitor the seawater quality for real-time risk identification.

6 OECD LEED Policy Review on: Sustainable Tourism and Local Development in Apulia Region, 2010

Related papers

- "Monitoring Apulia region coastline: A case study", F. Adamo, F. Attivissimo, C. Guarnieri Calò Carducci, A. M. L. Lanzolla, 2014 *IEEE Workshop on Environmental Energy and Structural Monitoring Systems (EESMS)*, pp. 1 - 5, DOI:10.1109/EESMS.2014.6923270

- "A Smart Sensor Network for Sea Water Quality Monitoring", F. Adamo, F. Attivissimo, C. Guarnieri Calò Carducci, A. M. L. Lanzolla, *IEEE Sensors Journal*, 2015, Volume: 15, Issue: 5, Pages: 2514 - 2522, DOI:10.1109/JSEN.2014.2360816

Chapter III
NETWORK AND STANDARDS

The proposed monitoring system network was specially designed to be robust and low-cost. It consists of multiple layers arranged according to international standard ISO/IEC/IEEE 21451.

In the following it will be given first a brief description of this standard, then the network architecture will be presented together with some design considerations about the signal coverage and power consumptions.

III.1 STANDARD FOR SMART SENSORS NETWORKS

The standard ISO/IEC/IEEE 21451 establishes the role of the main blocks a network of sensors and transducers, or more in general of smart transducers, defining also the common functions, the communications protocols and the structure of the electronic datasheet (TEDS). This family of standards has been introduced almost fifteen years ago to overcome the growing e-babel due to company development of proprietary standards concerning sensor

network [7]. The IEEE1451 project was not meant to be a mandatory directive for companies, but rather a collection of guidelines to implement versatile networks of smart interchangeable sensors with different brands. The key feature of this standard is that the data of all transducer are sent on the Internet with the same format, independent on the sensor physical layer (wired or wireless) [8]. Moreover, thanks to the open nature of this standard, different manufacturers can produce products with the assurance that they will self-configure and seamlessly integrate and operate with products from other manufacturers.

The IEEE 1451.x is also an evolving standard, recently updated, revised and accepted as the new International Standard 21451-x, thanks to the joint efforts of ISO, IEC and IEEE, and is constantly adapted to emerging communication technologies.

III.1.1 TRANSDUCER ELECTRONIC DATA SHEET

The Transducer Electronic Data Sheet (TEDS) is the heart of a system based on this standard and its implementation is defined in ISO/IEC/IEEE 21450, previously known as IEEE 1451.0. It is structured to contain all the typical information about a sensor (Fig. 6), such as the physics variable to be measured, the span, the detectivity, the frequency response, the calibration coefficients, and eventually other user defined additional entries. These data can be stored into the sensor to be read when requested by the system or can be hosted on line in the form of Virtual TEDS. The latter case is intended to consider those sensors for which the adaptation to the standard would be too expensive for companies

---

7 IEEE, The Institute of Electrical and Electronics Engineers, "IEEE Standard for a Smart Transducer Interface for Sensors and Actuators - Transducer to Microprocessor Communication Protocols and Transducer Electronic Data Sheet (TEDS) Formats, IEEE Standard 1451.2"–1997, Inc., NY, 1997.

8 D. Wobschall "Networked sensor monitoring using the universal IEEE 1451 Standard" Instrumentation & Measurement Magazine, IEEE, vol. 11, no. 2, pp 18-22, 2008.

[9], for instance sensor working at high temperature or simply to let older technologies to still be used in modern smart networks.

Channel TEDS:

```
TEDSID: 0 3 1 1
CalKey: 4           //  Calibration correction is applied in the TIM
ChanType: 0         // Sensor
Units:
  Type: 0
  rad^(0)sterad^(0)m^(-3)kg^(1)s^(0)A^(0)K^(0)mol^(0)Cd^(0)
  Extension: 0
LowLimit: 0            //  Operational lower range limit
HiLimit: 1E-2          //  Operational upper range limit
OError: 2E-7           //  Uncertainty under worst-case
SelfTest: 1            //  Self-test function provided
MRange: 0              //  No multi-range capability
Sample:
  SampleMod: 1         //  Single-precision real
  SampleModLength: 4   //  Number of octets (float32)
  SampleSigBits: 16    //  Number of bits from the converter
UpdateT: 0.000
RSetupT: 1.010          //  Read setup time
SPeriod: 0.001          //  Minimum sampling period
WarmUpT: 0.500          //  Warm-up time
RDelayT: 0.001          //  Read delay time
```

Fig. 6 Extract of the Channel TEDS memory content for Chl-*a* sensor

III.1.2 TIM AND NCAP MODULES

The standard also identifies two abstract blocks, the Transducer Interface Module (TIM) and the Network Capable Application Processor (NCAP), to be implemented together or on different devices, depending on the application context.

Different transducer channels may compose the first block, each one representing a sensor/actuator or an event sensor and it is supposed to encapsulate the relative TEDS (Fig. 7). The NCAP instead may be any device with a network interface, e.g. a personal

[9] J. Wiczer, “Smart Interfaces for Sensors”, Proceeding Sensor Expo – Smart Sensor Session, Chicago, IL, 2001

computer or an embedded device and should make sure that the TIM is visible from the rest of the network.

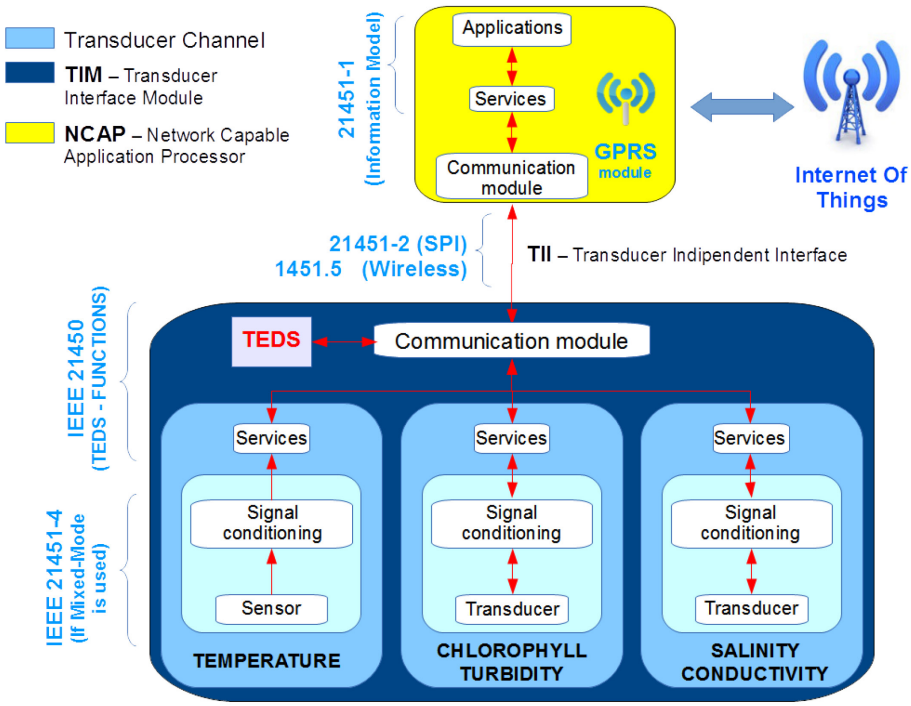

Fig. 7 IEEE 21451 Smart buoy abstract layers

The behavior of the TIM module (WTIM if wireless), its ability to generate message and replies to requests coming from the NCAP, as well as message structures and required/optional commands it should respond to, are also defined in 21450. With respect to the NCAP module, TIM side implementation follows guidelines defined in 21450, whereas for network side implementation it follows 21451-1 directives, which defines web services and applications it should provide. The communication layer between the TIM and the NCAP is the Transducer Independent Interface (TII). It includes different technologies, from point to point communication defined in 21451-2, to mixed-mode ones defined in 21451-4 or 21451-7 for RFID sensors. The

wireless interface is also available and defined in 1451.5, but it is waiting to be revised and accepted as an international standard.

III.1.3 COMMON COMMANDS

ISO/IEC/IEEE 21450 defines many command classes and different command functions for each class. These commands are intended to be universal commands for all ISO/IEC/IEEE 21451 compliant devices. Thus, all sensors and actuators should for instance respond to Trigger commands, with the underlying difference that the former should store the measured value into a buffer when triggered, waiting for a succeeding *Read Transducer Channel data-set segment* command, whereas the latter should behave actuating data previously written inside its buffer by means of *Write Transducer Channel data-set segment* command.

These commands must be structured in a message according to its format definition in 21450. Therefore, for instance, to query a sensor connected to TIM channel #1 or to drive an actuator on channel #2, two messages need to be sent to each channel, each one made up of 6 bytes at minimum, with a variable data payload which length is defined in *Length* field, as shown in TABLE I. However, it is also feasible to dispatch the same message to many different transducers, in fact in this case the standard foresees the creation of appropriate proxy groups.

TABLE I.
COMMAND EXAMPLES

Command	Channel Address		Command Class	Command Function	Length		Data
Sensor							
Trigger	0x**00**	0x**01**	0x**03**	0x**03**	0x**00**	0x**00**	-
	Channel 1		Operate	Trigger	MSB	LSB	
Read	0x**00**	0x**01**	0x**03**	0x**01**	0x**00**	0x**00**	-
	MSB	LSB	-	Read	MSB	LSB	
Actuator							
Write	0x**00**	0x**02**	0x**03**	0x**02**	0x**00**	0x**01**	0x**1F**
	Channel 2		Operate	Write	MSB	LSB	31_{DEC}
Trigger	0x**00**	0x**02**	0x**03**	0x**03**	0x**00**	0x**00**	-
	MSB	LSB	-	Trigger	MSB	LSB	

Using a Logic Analyzer, it's easier to understand how a 21451 transaction is made; for instance, Fig. 4 reports what happens when the NCAP forwards a *Read Transducer Channel data-set segment* command to the 21451-2 compliant probe through a SPI interface (Serial Peripheral Interface), to read the seawater temperature on *channel 1*.

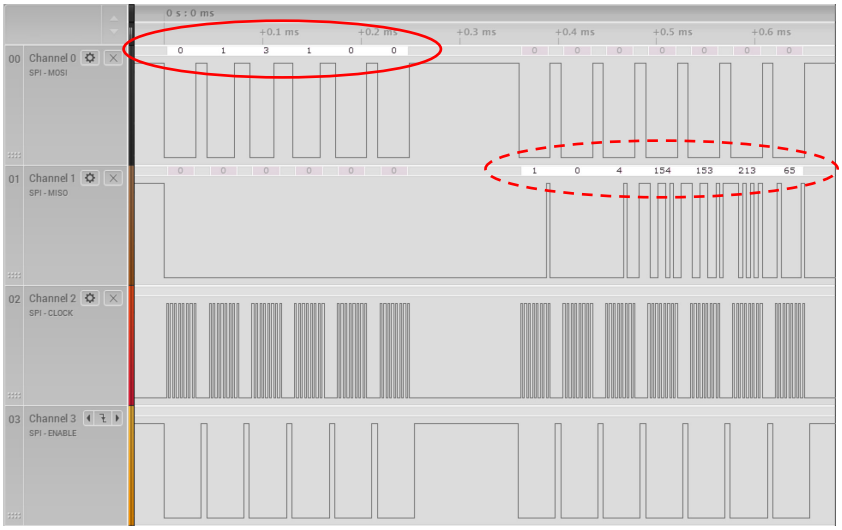

Fig. 8 SPI Query through sensor read command (solid) in TABLE I and response (dashed) of Temperature channel using Salae Logic Analyzer; Trigger command has been sent before time zero and therefore it's not visible

Per message/reply definition in 21450, the NCAP sends a Read command (solid) to the TIM as defined in TABLE I. After the command has been parsed and the temperature has been measured, the reply message (dashed) containing the acquired sample is stored inside the TIM output buffer, ready to be sent back on master request. Hence the NCAP reads the first reply octet, which contains the Success/Fail Flag and checks whether it is respectively bigger or equal to zero. Value 1 means that operation was successful and the NCAP can thus continue querying the next two octets that, once merged, contain the length of the payload, i.e. the number of remaining octets.

Since the temperature value has a floating-point precision, which needs 4 bytes to be stored, the payload contains four octets (154, 153, 213, 65) obtained using a simple union structure:

```
union  temp_val {
   byte   b[4];
   float   temp;
} T;
```

Once received, the NCAP merges the four bytes to obtain the original value of 26.7 °C acquired by the TIM first channel.

It is reasonable that the additional complexity required for 21450 command packet recognition would also introduce a greater delay in communication systems. In fact, it involves an approximately average increase in TIM reaction time of 50% [10], from the mean value of 2 ms without 21451 to almost 3 ms with it, a value that may appear considerable in some specific cases, but that it is generally negligible using modern microcontrollers.

III.2 NETWORK ARCHITECTURE

Coastal monitoring is a tough challenge in comparison to local smart sensor networks, mainly due to the hostile environment and long distances involved. In addition, the most important biological indicator of water quality, the chlorophyll-*a* molecule, does not exhibit a homogenous distribution in seawater but rather a spatial patchiness [11], meaning that events of potential interest can even happen on a scale of a few tens of meters.

---

10 J. Popelka, P. Paces, "Performance of smart sensors standards for aerospace applications", Electrical Review, vol. 88, pp. 229-232, 2012.

11 L.de Montera, M. Jouini, S. Verrier, S. Thiria, M. Crepon, "Multifractal analysis of oceanic chlorophyll maps remotely sensed from space", Ocean Science Discussions, Vol. 7 no.2, pp.219-229, 2011.

Thus, considering that the Water Framework Directive (WFD-2000/60/EC [12]) indicates 1 mile as the monitoring limit distance from the coast and that Apulia region has almost 800 km of coastline, any kind of widespread homogenous monitoring would be unfeasible and different approaches must be taken in consideration.

The exact positions of the sampling points must be accurately determined by the team of biologists in charge of monitoring, considering the history of the observed place, the influence of anthropogenic factors, as well as geo-hydro morphological features and the presence of usual marine currents. The relationship between nutrient disposability and algae replication is better appreciated when overlapping on a satellite image of Apulia region (Fig. 2), the second series of data in Fig. 3 and positions of wastewater treatment plants (responsible, together with the rivers, for the introduction of nutrients into the sea).

Merging the above data sets, two main scenarios arise which lead to different network layout, optimized for further analysis:

- Coastal water bodies known for their propensity to develop environmental critical situations, which need a constant monitoring.
- Transitional waters, in which the investigation of the influence area of possible pollution impacts would be of great interest.

The former is mainly related to those shores characterized by a rocky substrate, especially in areas with high nutrient density or

[12] European Parliament, "Directive 2000/60/EC of the european parliament and of the council establishing a framework for the community action in the field of water policy," CELEX-EUR Official J., vol. 327, pp. 1–72, Dec. 2000.

with natural geomorphological features that would promote algae replication.

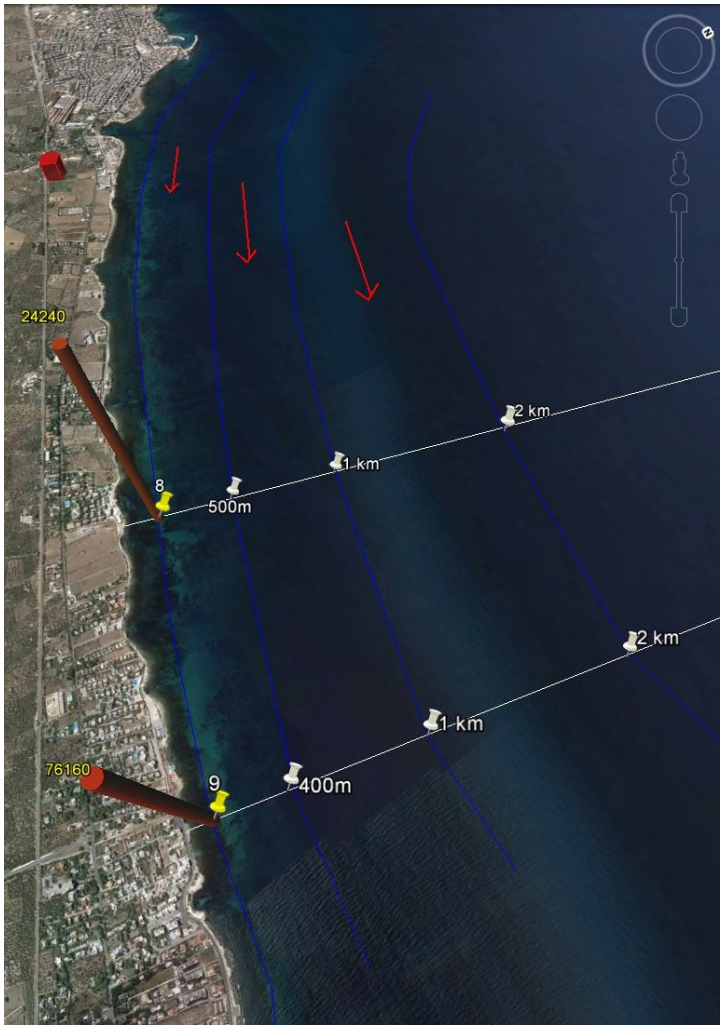

Fig. 9 Transects monitoring: Ostreopsis Ovata cell concentration in columns (ARPA 2014), typical water current flow (red), bathymetric lines (blue), transects (white), current fortnightly monitored spots (yellow), ideal additional spots (white).

For instance, spots 8 and 9 (Fig. 2), magnified in Fig. 9, fairly adapt to this description. They are placed respectively at 2.6 km and 4 km from the wastewater treatment plant (the red box), on the same bathymetric line (10 m of depth), which makes more

comparable the two readings. Hence, if a sensor network is adopted instead of fortnightly manual sampling, a deeper time resolution can be reached, while decreasing reaction time in case of indicators exceeding their limit values. Furthermore, a more accurate control of shore water quality may also be achieved if more probes are used, monitoring the same transects they rely on, i.e. the white lines perpendicular to the coastline (Fig. 9).

The latter scenario otherwise involves zones where nutrients are directly released, like in front of wastewater drains or towards river estuaries. In this case, biologists would prefer a different spatial distribution of sensor probes, more suitable to assess the edges of a possible pollution impact zone. Taking as an example the Ofanto River (Fig. 10), during the period 2010/2011 it has received a low LIMeco score in terms of intake of macronutrients such as NO3, PO4, but also considering Escherichia coli (E. coli) concentration, surfactants, herbicides, pesticides or silicates; on the other hand, it flows in a shore with sandy substrate, which does not favor the establishment of microalgae colonies. Unfortunately, the sandy bottom slopes more gently than the rocky one, eventually requiring greater distances to be covered.

An easily reconfigurable sensor network may be used in this situation to map the pollutant impact zone with high spatial resolution. Being for instance $f(x, y)$ a scalar field representing the water concentration of chlorophyll-*a* or of another indicator:

- ∇f is a vector field containing important information regard actual parameter diffusion
- $\nabla \cdot \nabla f$ is a scalar field containing additional information regard possible illegal sewages or pollutants accumulation spots.

Fig. 10 Transitional water monitoring: Radial probe distribution (white) for impact zone detection. Example of chlorophyll-*a* (red) and inverse salinity (yellow) gradient maps that can be obtained.

III.2.1 SMART BUOYS

Considering that internal distances between sensor probes in the two scenarios are likely less than 1 km and that maximum distances from farthest probe to the shore is generally below 1.852km (1 mile), two slightly different probe solutions have been

proposed for field covering, which can be integrated to work together:

Type **A**:

This is a self-sufficient buoy, conceived for isolated spot data surveying, but it can also operate in a local sensor network coordinating Type B probes.

By leveraging existing infrastructure (providers APN), a Type A probe (Fig. 11) have been proposed, equipped with a second generation (2G) General Packet Radio Service (GPRS) module. This device contains the TIM module but also act as an NCAP, being able to provide TCP features based on IPv4 protocol for internet access through Gateway GPRS Support Node (GGSN) (Fig. 13), with services and applications described in ISO/IEC/IEEE 21451-1. The communication between the NCAP and the TIM module is 21451-2 compliant, while 1451.5 compliance is currently under development adding an NRF24L01+ based (Nordic Semiconductor) wireless module.

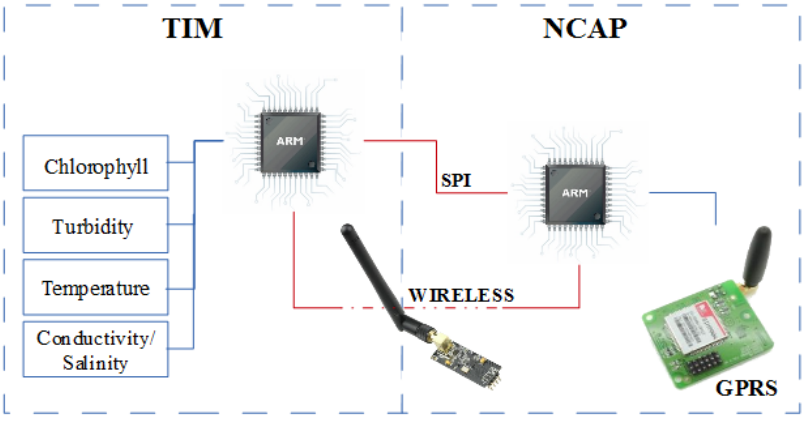

Fig. 11 Abstract probe architecture

Furthermore, the choice of a GPRS module equipped with an integrated GPS receiver, like the adopted SIM908 GSM/GPRS +

GPS module from SIMCom Wireless Solutions, would be highly recommended, to allow real time probe tracking and data interpolation over spatial coordinates without the need for an additional module.

In the proposed system two 32-bit ARM Cortex-M4 microcontroller with floating point signal processing unit are used (Fig. 11); the first one to control on board sensors, implementing the TIM block and communicating to the NCAP through Serial Peripheral Interface (SPI) connection, the second to implement di NCAP itself.

The NCAP side, encapsulate an embedded light server able to provide advanced machine-to-machine (M2M) interactions based on the underlying HTTP/1.1 protocol and XML request/response messages as payload to GET or POST HTTP methods. Human interaction is also allowed through a simple HTML user web interface (Fig. 12) which adopts Asynchronous JavaScript and XML (AJAX) technique for efficient background data exchange between server and web browser, allowing dynamic web page content update.

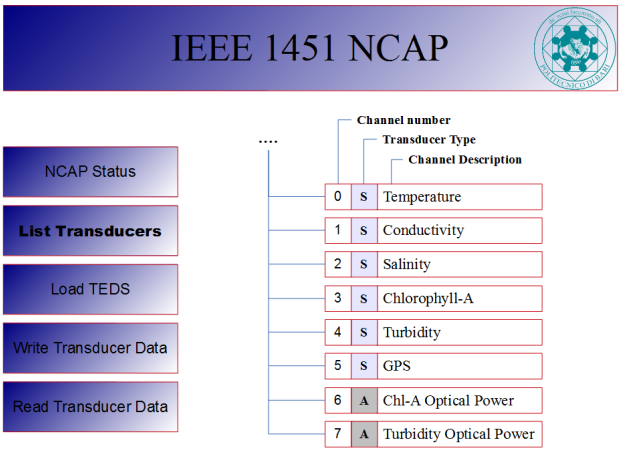

Fig. 12 Simple web server NCAP interface

This behavior may be basically implemented in two different ways, using a Web Server with Common Gateway Interface (CGI) to handle POST requests or with an Application Server designed specifically for use on deeply embedded systems. The former is an older method to handle data returned by a web browser, thus requesting low-level C code, easily error-prone, redefinition of routines needed. Conversely the latter adopted solution is a Lua-based application server (e.g. Barracuda Web Server) that integrates web server functionality to handle requests and provide a built-in C/C++ application framework for invoking C/C++ programs. In addition, Lua-based servers allow system update through the on-fly program compilation, without the need to take the system down.

In order to control many probes geographically spread out in a single network and grant at the same time a secure data transmission, an Internet Protocol-Virtual Private Network (IP-VPN) must be adopted (Fig. 13). Using a fixed IP address and a VPN router inside the control room, a secure tunnel is created over the internet, able to ensure that only eligible users have access to data during the overall transmission.

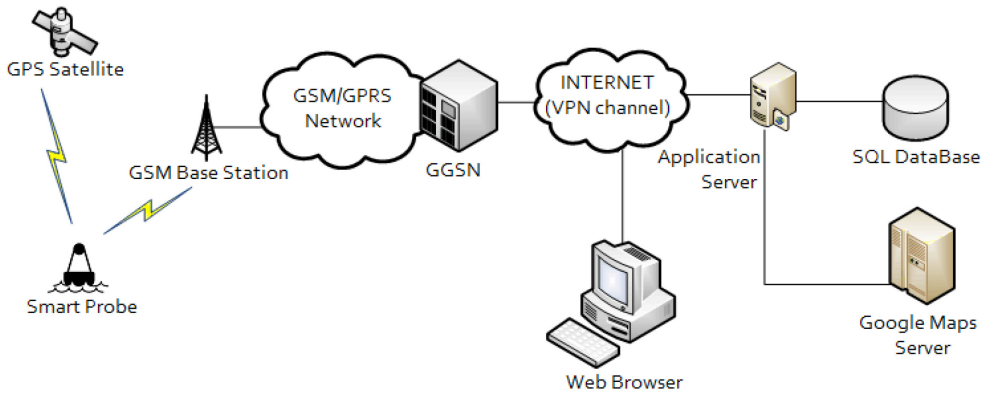

Fig. 13 – General network architecture and services

Type **B**:

This device is composed by the same Transducer Channels as Type A, being able to monitor the same parameters, plus a dedicated GPS module. Nevertheless, its interface implementation is slightly different from type A; in fact, it is not independent and it should actually work in a network, acting as a Wireless-TIM (IEEE 1451.5 compliant) connected to the NCAP inside Type A buoys by mean of NRF24L01+ module.

The PHY TEDS data-block of this device contains specific information about the communication channel as defined in 1451.5, like Radio type, Max Data throughput, Authentication and others. Even though the radio interfaces currently covered by the standard are only four

- IEEE 802.11
- Bluetooth
- ZigBee
- LoWPAN

the adopted one does not implement any listed network stack, therefore the Manufacture specific code (255) is used in TEDS. The communication between NCAP and WTIM in fact relies on Nordic Semiconductor MultiCeiver™ technology, which let the use of up to 6 data pipe for 1:6 star networks and Enhanced ShockBurst™ which features automatic packet handling, automatic acknowledgment and retransmission. Considering operation in a harsh environment, this is an extremely useful built-in function. In this configuration Type A probes gather the Primary RX status, while Type B the Primary TX, allowing bi-directional communication, simply configuring internal register map through SPI interface. In order to overcome the 6:1 network size limitation,

a mesh network implementation using the same module is currently under investigation.

III.2.2 INTERACTIONS DESCRIPTION

To speed up the creation of the network stack, both the NCAP and the TIM have been implemented using Arduino open-source integrated development environment (IDE), which provides a useful hardware abstraction layer (HAL) for cross-compiling among different platform. As result, once the entire stack code has been written and tested, it can be simply compiled for the selected final hardware solution.

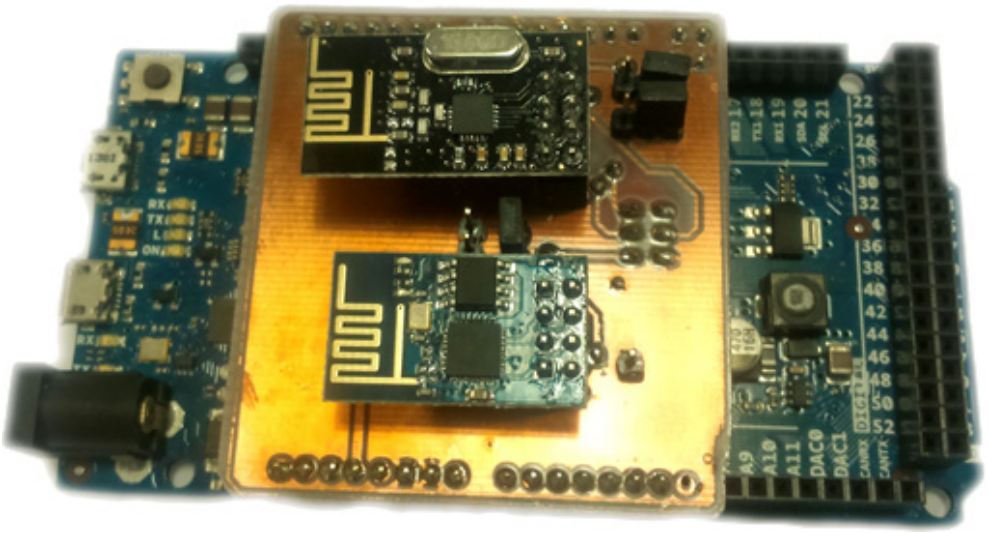

Fig. 14 – Arduino DUE board with adapter board for simultaneous testing of the nRF24L01+ module (black) and ESP8266 (blue)

Furthermore, at this early stage of the network development and for easier indoor device testing, the adopted GPRS SimCOM 908 module has been substituted with a Wi-Fi one, the EspressIF ESP8266, with which it shares the same set of AT commands, except for a handful of functional related commands. In this way, after developing the framework using appropriate preprocessor

directive for code differentiation, the two modules can just be swapped with no further required changes.

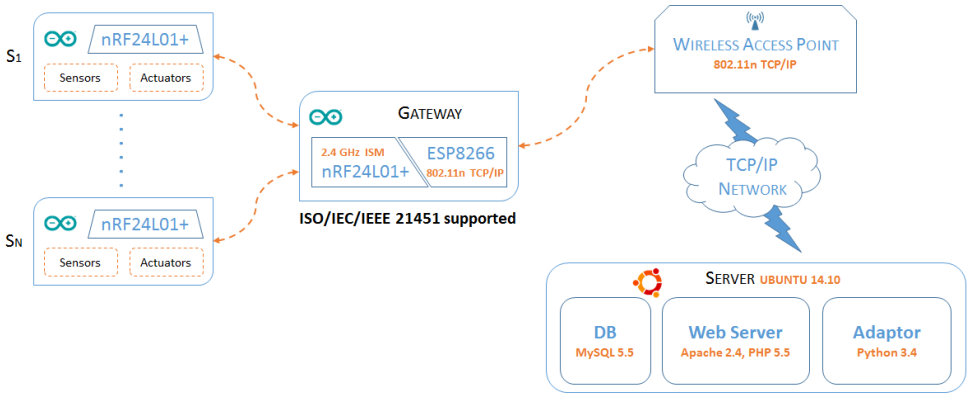

Fig. 15 – Adopted architecture for network designing and prototyping

Hence, the NCAP and the TIM firmware have been developed respectively using an Arduino DUE board (Fig. 14), based on a 32-bit Atmel SAM3X8E ARM Cortex-M3 CPU microcontroller and an Arduino UNO board, based on an 8-bit ATmega368PU. The choice of a powerful development board was due in the former case to the need of running the protocol translational engine requested by the ISO/IEC/IEEE 21451 standard, between external HTTP-XML based commands and internal messages structure. Whereas in the latter case, after developing the stack code, the firmware has been ported to a similar 32-bit board to execute the complex algorithm described in IV.1.1.

The NCAP gateway connects the sensor network based on the nRF24L01+ modules, in which it has the logic address #0, with the rest of the network based on IP protocol. The latter link is provided by the ESP8266 Wi-Fi chipset, which integrates a complete TCP/IP protocol stack. At the beginning of the payload of each packet received by the nRF24L01+ module, it adds the address of the sender and forwards it to the server via the ESP8266 Wi-Fi link. Conversely, in receive mode, the gateway extracts the

first byte of the packet received by the ESP8266 (Fig. 16) to obtain the address of the destination smart sensor, then forwards the packets by means of the nRF24L01+. The addressing method, as previously mentioned, is based on the Nordic Semiconductor proprietary standard, whereas the packet payload contains messages formatted using ISO/IEC/IEEE 21451 standard.

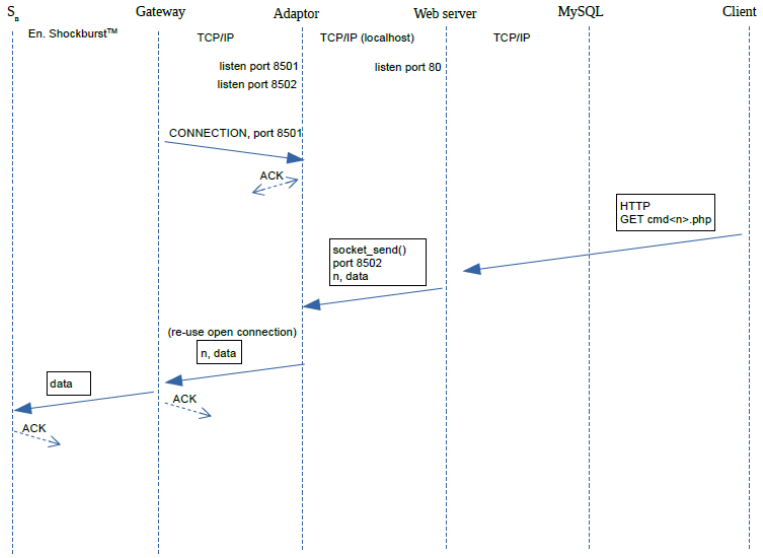

Fig. 16 – Remote smart sensor control sequence diagram

The server is implemented in Ubuntu 14.10 and provides SSH and SFTP services for remote administration and content uploading. Three main blocks run on the server:

- **Adaptor** server: it is a multi-threaded server implemented in Python with a listening port (8501) for packets coming from the gateway. Each received packet (Fig. 17) generates two HTTP POST requests to the Web server:

    1. to *http://localhost/store0.php*
    2. to *http://localhost/store<n>.php*, where *<n>* is the smart sensor address of the incoming packet

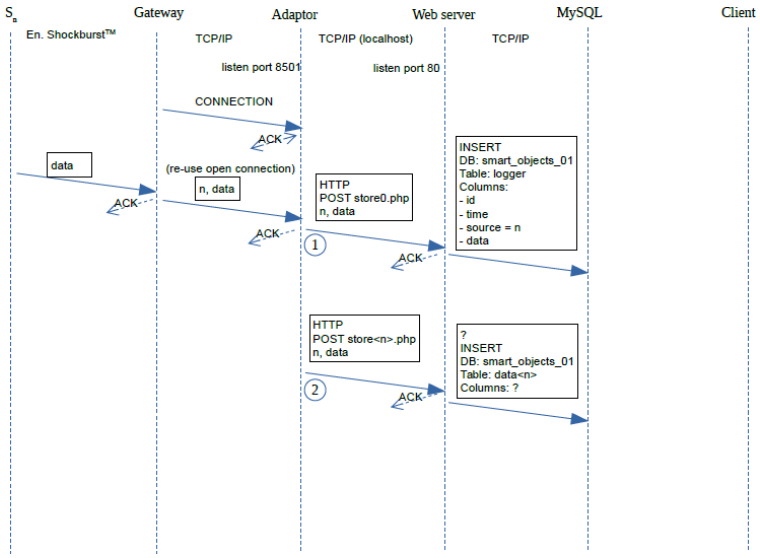

Fig. 17 – Data storing sequence diagram for smart sensors

The Adaptor has an additional listening port, 8502, for payloads arriving from the Web server, which are subsequently forwarded to the gateway. These payloads must have, as the first byte, the address of the smart sensor.

- **MySQL** server: the *smart_objects_01* database is available in the local network and can also be administered through phpMyAdmin. All the smart sensors interactions are stored in a *logger* table (Fig. 18), which is populated by *store0.php*. The database also contains the *data<Sensor><n>* table that is populated by the script *store<n>.php*.

#	Name	Type	Collation	Attributes	Null	Default	Extra	Act
1	id	int(10)		UNSIGNED	No	None	AUTO_INCREMENT	
2	time	timestamp		on update CURRENT_TIMESTAMP	No	CURRENT_TIMESTAMP	ON UPDATE CURRENT_TIMESTAMP	
3	source	int(3)		UNSIGNED	No	None		
4	data	varbinary(512)			No	None		

Fig. 18 – *Logger* table

- **Web** server: it is an Apache 2.4 server with PHP 5.5. It executes the previously mentioned scripts: *store0.php* that

stores the incoming data from each smart sensor in the *logger* table and *store<n>.php*, which accepts HTTP POST requests generated by the Python Adaptor upon reception of data from the node <*n*>. Fig. 19 shows the sequence diagram relevant to page *read0.html*, which is able to read and plot data from the table with automatic updating via AJAX technique, aided by the script *read_update0.php*.
The webpages wait<n>.html have been created to report in real time alarm messages and updates from any smart sensor. This has been made possible by using the Sync extension for PHP and inserting a special Event object in scripts store<n>.php and wait_update<n>.php (Fig. 20).

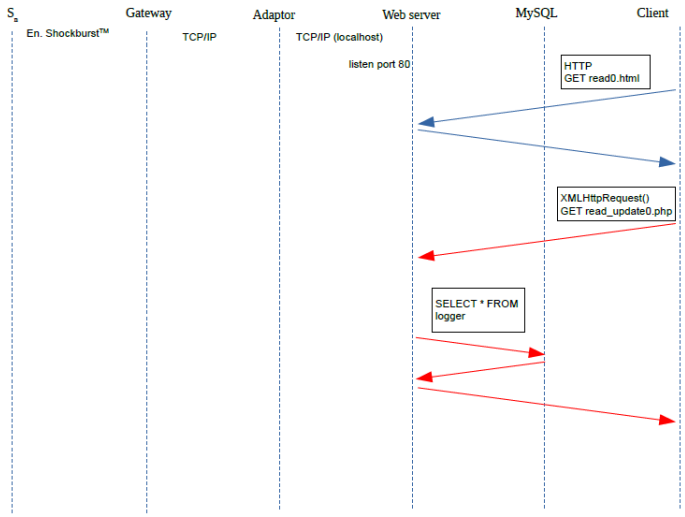

Fig. 19 – Read/Plot sequence diagram

The script wait_update<n>.php remains in fact locked (with timeout) until it receives a signaling event from store<n>.php and subsequently, thanks to an AJAX request, the wait<n>.html page can detect the event and updated its content dynamically.

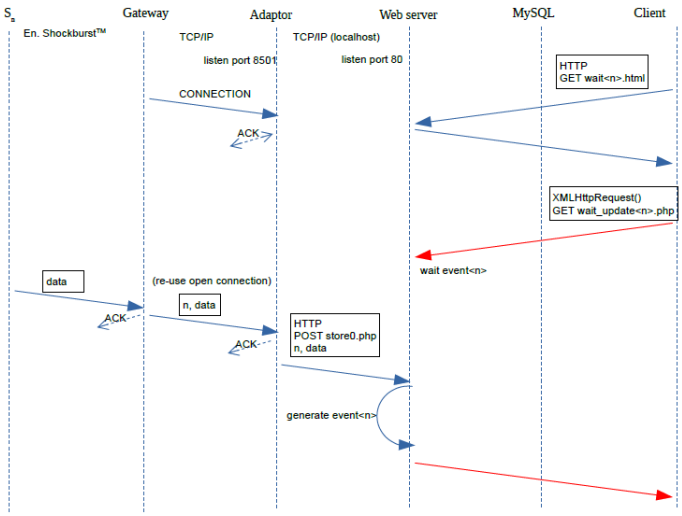

Fig. 20 – Events handling and data visualization sequence diagram

III.2.3 NETWORK SIGNAL COVERAGE

The adopted NRF24L01+PA+LNA module has a transmitting Power Amplifier and a receiving Low Noise Amplifier, which respectively grant a maximum output power of $+20$ dBm and a receiving sensitivity of -104 dBm at 250 kbps, a more than sufficient speed if a heavy real-time stream communication is not required.

To assess the network feasibility, the signal strength between sensor probes needs to be evaluated. For this purpose, an important parameter is the FSL (Free Space Loss), defined as

$$\mathrm{FSL} = -20\log_{10}\left(\frac{\lambda}{4\pi d}\right) \tag{3}$$

where λ is the signal wavelength and d is the distance between transmitter and receiver antennas. Plotting the value of FSL with respect to the distance (Fig. 21) and fixing a link length of 1 km

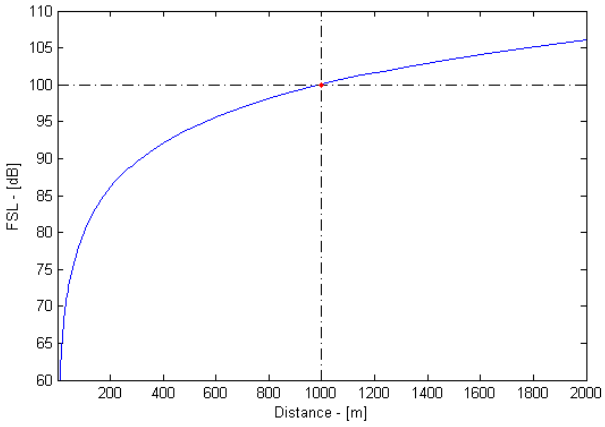

Fig. 21 Free Space Loss vs. Transmitting distance (carrier frequency is 2.4 GHz)

between transmitter and receiver, leads to $FSL_{MAX} = 100$ dB; doubling the distance the FSL increases of 6 dB.

Considering 0.5 dB as cable loss for a length of 1 m, it is possible to use the module parameters to perform a link budget.

TABLE II.
LINK BUDGET CALCULATION

	20 dBm	(TX Power)
+	2 dBi	(TX antenna gain)
-	0.5 dB	(TX cable loss)
+	2 dBi	(RX antenna gain)
-	0.5 dB	(RX cable loss)
	23 dB	**Total Gain**
-	100 dB	(Free Space Loss @ 1km)
	-77 dB	**Expected signal level**
-	-104 dBm	Sensitivity @ 250 kbps
	27 dB	**Link Margin**

Though the Link Margin is largely above the confidence threshold of 10 dB, further considerations need to be carried out. In fact, despite marine environment is characterized by the absence of almost any obstacle, the height of the antenna over the water level plays also an important role.

If considering the signal reflection upon seawater (approximated as a perfect conductor) and using 2-ray model [13], a new value can be derived for Propagation Losses

$$\begin{aligned} \mathrm{PL(dB)} = {} & 40\log(d) \\ & - (10\log(G_t) \\ & + 10\log(G_r) + 20\log(h_t) + 20\log(h_t)) \\ & = 40\log(1000) - (20\log(2) + 40\log(1)) \\ & = 113.98 \end{aligned} \tag{4}$$

where G_t and G_r, h_t and h_r, are respectively the transmitting and receiving antenna gain and height (assumed 1 m over seawater level). Using Propagation Losses (PL) instead of Free Space Losses in TABLE II, leads to a reduced Link Margin equal to 13 dB.

In addition, for microwave communication (this is the case for nRF24 module that transmit at 2.4 GHz in the ISM band) it is not sufficient that antennas are on the same Line of Sight (LoS), they also must have at least a clear first Fresnel Zone, because obstacles may cause reflection and diffraction introducing additional signal paths. To take into account these effects, the *n*-th Fresnel zone define a portion of space enclosed by an ellipsoid, for which a potential obstacle on the path may in fact interfere constructively or destructively, respectively in even and odd zones. However, if the first Fresnel zone is kept clear at least at 55% [13], then further Fresnel zone clearance does not significantly affect diffraction

[13] Theodore S. Rappaport, "Wireless Communication: Principles and Practice", Prentice Hall, 2 edition, January 10, 2002.

losses. Considering a link distance of 1 km, the 1st Fresnel Zone radius in the middle distance, i.e. for $d_1 = d_2 = 500$ m, is

$$F_n = \sqrt{\frac{n\lambda d_1 d_2}{d_1 + d_2}} = \sqrt{\frac{\lambda 500^2}{1000}} = 5.59 \text{ m} \tag{5}$$

$$F_{55} = 5.59 \cdot 0.55 = 3.07 \text{ m} \tag{6}$$

This means that the antenna's height of each probe should be at least 3 m for total losses to be equal to FSL, confirming that PL due to a shorter antenna are higher than FSL.

Careful mathematical simulations should be carried out to evaluate the effects of rough seas, which cause multiple diffraction due to the waves ridges; however, an estimate of the minimum loss values can be made considering the diffraction due to a single ridge placed in middle, using Knife-edge Diffraction model [13].

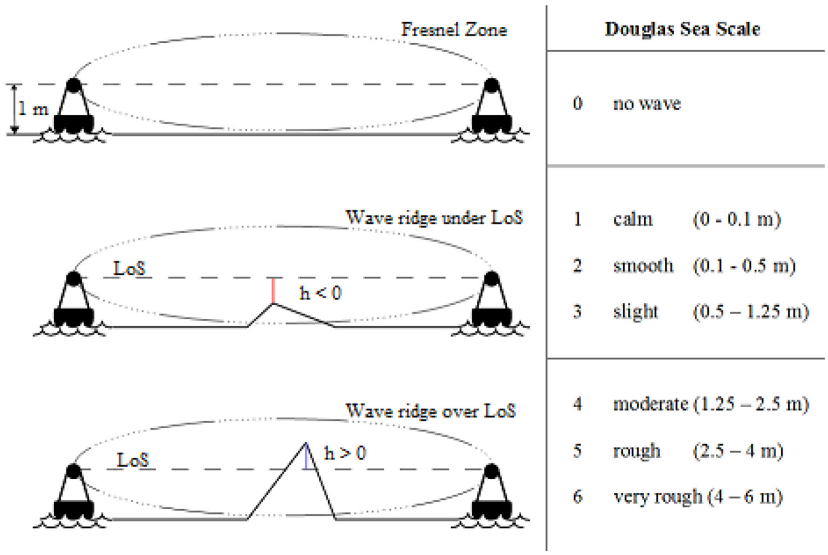

Fig. 22 Edge values used in the model, related to Douglas Sea scale

For each wave height in Fig. 22, dimensionless Fresnel-Kirchhoff diffraction parameters are computed as follow

$$\nu = h\sqrt{\frac{2(d_1 + d_2)}{\lambda d_1 d_2}} \tag{7}$$

where h is equal to wave ridge height minus LoS height and d_1, d_2 are assumed to be equal to 500 m. Using Lee [14] approximation, the numerical relation between Douglas Sea scale and Diffraction loss is calculated and reported in Fig. 23.

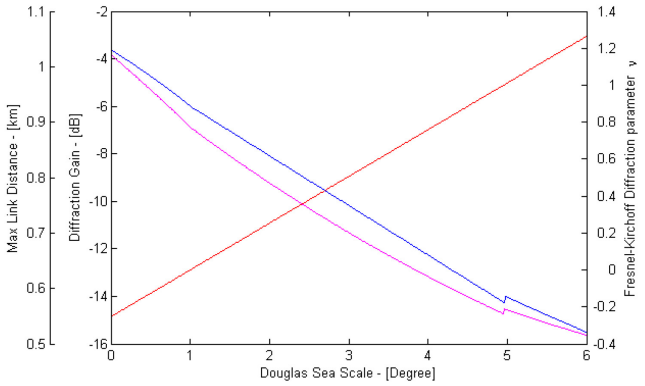

Fig. 23 Diffraction Gain (blue) and Fresnel-Kirchhoff Diffraction parameter (red) for $d = 1$ km; Maximum link distance (magenta) with Link Margin $= 10$ dB

Diffraction Loss graph suggests that using an antenna height of 1 m and a limit distance of 1 km, the link strength is just enough for calm water to leave 10 dB of Link margin and it rapidly degrades with sea rough increasing.

At last, a coverage simulation for analytical results verification has been performed (Fig. 24), showing that green zone has 1 km radius as expected; further investigation will also be carried out to compare theoretical values with experimental data.

[14] Lee, W. C. Y., "Mobile Communications Engineering", McGraw Hill Publications, New York, 1985.

Fig. 24 Coverage simulation around central buoy ("415m" in Fig. 10): green zone has strong signal (Link Margin > 10 dB), yellow zone has weak signal (Link Margin < 10 dB)

III.2.4 Power Consumption

The assessment of the power consumption of the proposed device in its different operating modes is needed to carry out a reliable energy budget with respect to adoptable energy harvesting systems and for the dimensioning of the required battery pack. However, a fully characterization of a network module in microcontroller based application, requires the measurement of currents which alternates in a high dynamic range from extremely low power modes to fast transmitting bursts. This task is usually accomplished using extremely performant and expensive instruments, able to provide at the same time a very high resolution and a sufficiently large bandwidth, whereas usually adopted shunt based techniques are not able to provide acceptable results.

To overcome this limitation, a new measurement technique able to provide high accuracy on a wide dynamic range of current values has been introduced and validated, against other well-known methods, to provide a precise characterization of the adopted hardware configuration.

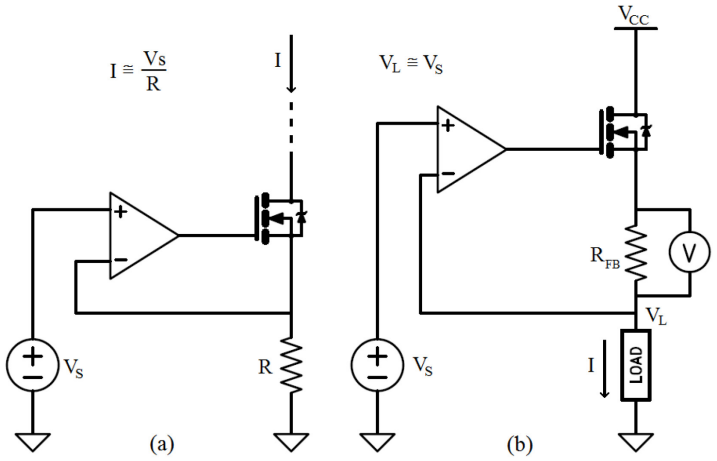

Fig. 25 - Voltage-controlled current sink (a), proposed "shunt + feedback" method to measure the current in the load for a fixed operating voltage (b)

The op-amp-based voltage-controlled current generator (Fig. 25a) is largely used to easily create a current sink/source, since its voltage follower configuration forces the input voltage over a known resistor R, so to generate the desired current.

Exploiting the ability of the virtual short-circuit between terminals to maintain a fixed potential approximately equal to V_S at the op-amp inverting input, a load was put in place of R so to fix its operating voltage to a given value $V_L \cong V_S$. Furtherly a shunt resistor R_{FB} was placed in series with this node (Fig. 25b), which voltage will add up to the load operating voltage. The clear advantage is thus to untie the tradeoff between the need to use larger resistors to detect small currents, and the necessity of not altering the voltage on the load, which would result in a perturbation of its operating condition and of its power consumption. In addition, in this configuration the op-amp input offset no longer affects the detectability of small currents, since it affects only the accuracy of the voltage imposed to the load.

The proposed method in Fig. 25b is, however, subject to the onset of oscillations due to the continuous change of the transistor

bias point while the current drained by the load varies. The equivalent impedance of the load, especially in presence of large capacitive loads, interacts with the feedback loop, promoting the spreading of unwanted resonances that must be suppressed. To find the best values of compensation capacitors that provide stability over the range of interest, the design process has been conducted making use of PSpice tools for parametric simulations.

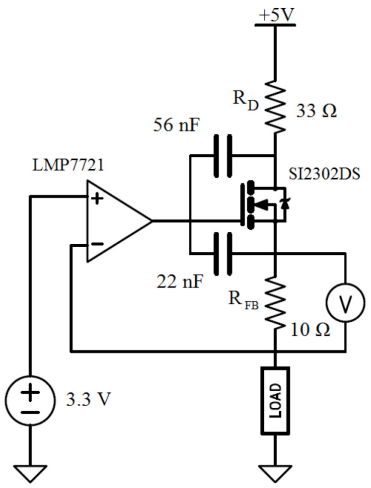

Fig. 26 Adopted circuit for the measurement scheme

The final circuit is reported in Fig. 26, where a resistor and two capacitors have been added to suppress the undesired oscillations in the working current range, which is 1 µA to $I_{MAX} = 30$ mA for the sensor node described in III.2.2, with capacitive loads up to 10 nF. The usable current range is shown in the simulation of Fig. 27,

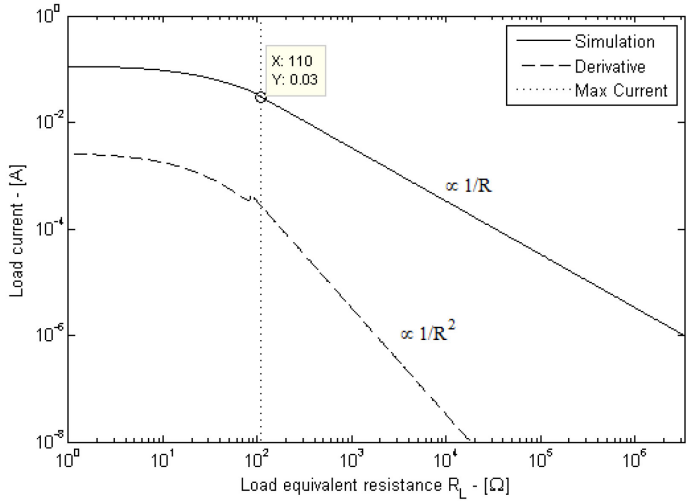

Fig. 27 - Load current as a function of load resistance, obtained by means of a PSpice DC simulation. The derivative of the load current and the higher current limit are also indicated.

where the vertical line denotes the maximum current such that V_L remains nearly constant, $I_L \propto 1/R$ and the MOSFET remains in the saturation region. The derivative of I_L with respect to R, which is proportional to $1/R^2$, is also shown to emphasize the useful operating range.

In general, when no measurement or transmission activity is required, the microcontroller and the wireless module should be in the lower admissible power consumption mode. The microcontroller runs at 1 MHz and, to save energy, it is put into *power-down* mode with the possibility of being awakened in two different ways: periodically by the internal watchdog, in a sensor configuration called *Tx mode*; or upon reception of an external interrupt from the wireless module, in the *Rx mode* configuration. In the former case, the wireless module is in *power-down* and is awakened by the microcontroller; in the latter case, it is *standby-I mode*, and is awakened upon reception of a radio packet. Furtherly, a third operational mode of the sensor node, *TxRx mode*, is also

taken into consideration for a mixed behavior. A summary of all designed energy saving combinations for the microcontroller and the wireless module and respective current consumption measurements are reported in TABLE III. Since these measurements are relative to stationary energy saving operation, which can be artificially prolonged for an indefinite time, they have been performed with a high precision multimeter. To extend the characterization to the other operating phases of the sensor node, characterized by fast variations of current consumption, the proposed method was used as illustrated in the following subsection.

TABLE III.
SENSOR NODE MODES AND CURRENT CONSUMPTIONS[A] [B]

Sensor mode	ATmega328P		nRF24L01+	
	Mode	Current [μA]	Mode	Current [μA]
Tx	Pwd/Wdt	4.38	Pwd	1.13
Rx	Pwd/Int	0.106	Standby-I	25.4
TxRx	Pwd/Wdt+Int	4.38	Standby-I	25.4

a. Measured using an Agilent 3458A multimeter

b. *Pwd* stands for *power-down*; *Wdt* and *Int* mean, respectively, that the internal wake-up on *watch-dog* and on *pin interrupt* are active

Observing energy consumption in real operating conditions required a high current measurement rate. Indeed, when the sensor node is configured to work in Tx mode, the microcontroller wakes up when the configured watchdog interval is elapsed, then checks if the desired interval between transmissions is also elapsed. If so, it completes the procedure transmitting a 32-byte packet at 2 Mbps on-air data-rate before returning to sleep mode. Hence, in Tx mode the sensor node has three operating phases: power-down of both microcontroller and wireless module, wake-up on watchdog and transmission, to which is added a fourth survey phase (data acquisition and processing) that has been measured separately for a typical procedure, consisting in one ADC sampling and three floating point operation for data conversion.

The measurements performed with the proposed method on a sensor node working in Tx mode are shown in Fig. 28, where the fast transition of current in the watchdog and transmission windows can be appreciated.

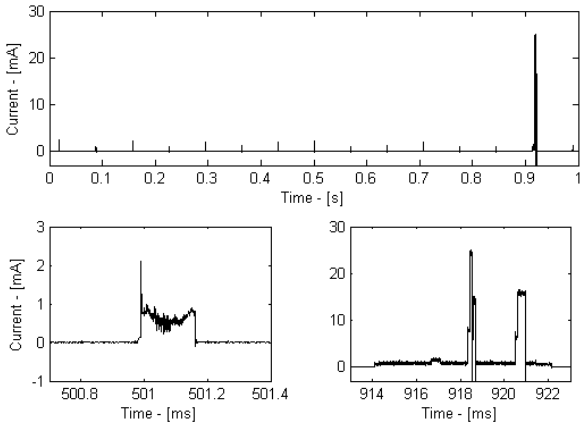

Fig. 28 Sensor node current measured with the proposed method (top), zoom of one of the many watch-dog events (left), which repeat every 64 ms, and zoom of a data transmission event (right). The entire cycle repeats every one second.

The power consumption characterization was carried out performing an accelerated test, with transmissions events set to a relatively high frequency, 1 Hz. The current was hence sampled at $f_s = 1$ MS/s for 100 s, obtaining a vector $\mathbf{I}_{Sh}$ of N measurements of the shunt current, with $N = 10^8$ (see Fig. 29a for a one second subset).

Since this large data set contained hundreds of events, an automatic segmentation algorithm was developed to identify the operating phases of the sensor node in Tx mode, allowing to calculate energy consumption for each phase: power-down, wake-up on watchdog and transmission.

The segmentation algorithm consists in the following steps, which are repeated for each measurement method.

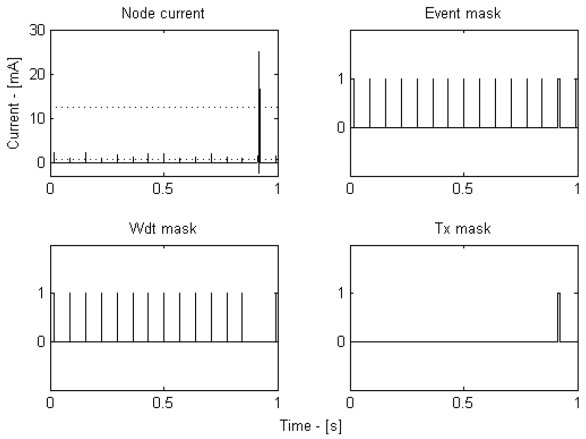

Fig. 29 a) Sensor node current consumption (solid line) measured with the proposed method and thresholds (dotted lines); b) event mask; c) Wdt mask; d) Tx mask

Firstly, a low threshold $th_1 = std(\mathbf{I}_{Sh})$ and a high threshold $th_2 = \max(\mathbf{I}_{Sh})/2$ are calculated from the $\mathbf{I}_{Sh}$ vector and used to calculate two raw logical masks:

$$\begin{aligned} \mathbf{M}_1 &= \mathbf{I}_{Sh} > th_1 \\ \mathbf{M}_2 &= \mathbf{I}_{Sh} > th_2 \end{aligned} \tag{8}$$

where the greater-than operator is applied to each element of $\mathbf{I}_{Sh}$, so obtaining Boolean vectors $\mathbf{M}_1$ and $\mathbf{M}_2$ of size N. Ideally, a given element of $\mathbf{M}_2$ is true when the corresponding element of $\mathbf{I}_{sh}$ is relevant to a measurement performed when the sensor node is transmitting. Analogously, a given element of $\mathbf{M}_1$ is true when the sensor node is not in power-down.

These masks may still contain holes inside the event windows because of current fluctuations around the thresholds. Thus, the final event mask $\mathbf{M}_{\text{EVENT}}$ (Fig. 29b), which individuates the instants in which the sensor node is not in power-down, is derived from $\mathbf{M}_1$ using a morphological closing operation [15], which consists

15 R. C. Gonzalez, R. E. Woods , "Digital Image Processing," 3rd ed, Prentice Hall, 2008.

in a dilation operation $\oplus$ with a structuring element SE_1 large 300 μs followed by an erosion $\ominus$ with the same structuring element

$$\mathbf{M}_{\mathrm{EVENT}} = \mathbf{M}_1 \bullet \mathbf{SE}_1 = (\mathbf{M}_1 \oplus \mathbf{SE}_1) \ominus \mathbf{SE}_1 \tag{9}$$

A dilation operation process is also applied to $\mathbf{M}_2$ with a larger 50 ms structuring element $\mathbf{SE}_2$, so obtaining a mask $\mathbf{M}_3$ around higher consumptions instants due to transmission. A logical *and* operation, $\wedge$, with $\mathbf{M}_{\mathrm{EVENT}}$ is performed to individuate the entire transmission phases, which are characterized by an alternation of higher and lower currents, so obtaining the final transmission mask $\mathbf{M}_{\mathrm{TX}}$ (Fig. 29d)

$$\begin{aligned} \mathbf{M}_3 &= \mathbf{M}_2 \oplus \mathbf{SE}_2 \\ \mathbf{M}_{\mathrm{TX}} &= \mathbf{M}_{\mathrm{EVENT}} \wedge \mathbf{M}_3 \end{aligned} \tag{10}$$

Two more masks, power-down $\mathbf{M}_{\mathrm{PWD}}$ and watchdog event $\mathbf{M}_{\mathrm{WDT}}$ (Fig. 29c) are obtained as follows

$$\begin{aligned} \mathbf{M}_{\mathrm{PWD}} &= \neg \mathbf{M}_{\mathrm{EVENT}} \\ \mathbf{M}_{\mathrm{WDT}} &= \mathbf{M}_{\mathrm{EVENT}} \ \mathrm{XOR}\ \mathbf{M}_{\mathrm{TX}} \end{aligned} \tag{11}$$

The above-defined masks were used to perform a numerical integration of the current I_{Sh} for transmission and watchdog events, in order to compute the average and the standard deviation of the requested charge per event, whose values will be expressed in [Ah] instead of coulombs [C], to simplify their comparison with batteries' capacity. Considering, for example, the computation of the transmission charge, firstly the transmission events are searched by individuating all the connected components [15] in which $\mathbf{M}_{TX}$ is true, so obtaining M set of indices $C_1, \dots, C_M$, where M is the number of events. The charge of the m-th event is then $Q_{Tx,m} = \frac{1}{f_s} \sum_{i \in C_m} I_{Sh,i}$, from which average and standard

deviation of the M events is easily calculated. The charge of watchdog events is calculated similarly by using $\mathbf{M}_{WDT}$.

The integration results are used to compute the necessary statistics over 90 identified transmission events and 1441 identified watchdog events. Mean values are reported in TABLE IV together with the other parameters that fix the sensor node operation other than time interval between transmissions T_{Tx} and number of bytes transmitted N_{Tx}. In particular, a sensor node task model is used in which, before each transmission, N_{Op} operations are performed, each one having duration T_{Op}, microcontroller current I_{Op} and involving sensor circuitry current I_S.

TABLE IV.
SYMBOLS, VALUES AND DESCRIPTION OF DESIGN PARAMETERS

Symbol	Value		Description
$I_{Pwd,Tx}$	4.93	[μA]	Power-down current, sensor in Tx mode[a]
$I_{Pwd,Rx}$	25.4	[μA]	Power-down current, sensor in Rx mode[a]
$I_{Pwd,TxRx}$	30.3	[μA]	Power-down curr., sensor in TxRx mode[a]
Q_{Wdt}	31.12	[pAh]	Watchdog Event
T_{Wdt}	0.016 – 8	[s]	Watchdog Interval
Q_{Tx}	5.4	[nAh]	Transmission Event
T_{Tx}	-	[s]	Transmission Interval
N_{Tx}	-	-	Number of 32-byte packets
I_{Op}	798	[μA]	Operating Event [b] [c]
T_{Op}	1.795	[ms]	Operating Time [c]
N_{Op}	-	-	Number of Operations
I_S	-	-	Sensor circuitry current

a. Combined microcontroller and wireless module power-down current

b. Measured with an Agilent 3458A 8½ digital multimeter

c. The operation consists of 1 ADC conversion and 3 floating-point calculations. The time was calculated as the average of a loop containing 100 such operations.

TABLE IV can be used together with the following simple design formula to evaluate the hourly battery consumption of a WSN node based on the proposed framework

$$Q_h = (1\text{h}) \cdot I_{Pwd} + \frac{1\text{h}}{T_{Wdt}} \cdot Q_{Wdt} + \frac{1\text{h}}{T_{Tx}} \cdot [N_{Tx} \cdot Q_{Tx} + N_{Op} \cdot T_{Op} \cdot (I_{Op} + I_S)] \qquad (12)$$

where I_{Pwd} is one of the values $I_{Pwd,Tx}$, $I_{Pwd,Rx}$ or $I_{Pwd,TxRx}$ from TABLE IV.

The expected sensor node lifetime L_{Exp} in hours is very simple to calculate using the given formula, since it only implies a division by the adopted battery capacity Q_{Batt}

$$L_{Exp} = \frac{Q_{Batt}}{Q_h} \text{ [h].} \qquad (13)$$

Of course, the designer may use this information choosing the transmission intervals to obtain longer lifetimes, or different techniques can be exploited, such as those based on energy harvesting from photovoltaic and thermoelectric generators [16] to charge the battery while the sensor is in power-down.

The given design formula is a simplified expression that tends to under estimate the expected lifetime in conditions of highly intensive operations, since the power-down current should be multiplied by 1 hour less the sum of all other events duration. Furthermore, asynchronous occasional Rx events of the wireless module are considered negligible with respect to the overall current consumption; if this is not the case, an Rx event probability density function may be used to take also into account this contribution.

---

16 F. Attivissimo, A. Di Nisio, A.M.L Lanzolla, M. Paul, "Feasibility of a photovoltaic–thermoelectric generator: performance analysis and simulation results," IEEE Trans. on Instr. & Meas., vol.64, no.5, pp.1158,1169, May 2015.

Related papers

- "A Smart Sensor Network for Sea Water Quality Monitoring", F. Adamo, F. Attivissimo, C. Guarnieri Calò Carducci, A. M. L. Lanzolla, *IEEE Sensors Journal*, 2015, Volume: 15, Issue: 5, Pages: 2514 - 2522, DOI:10.1109/JSEN.2014.2360816

- "New Technologies and Perspectives for Laboratory Practices in Measurement Science", F. Adamo, F. Attivissimo, G. Cavone, C. Guarnieri Calò Carducci, A. M. L. Lanzolla, 2015 *IEEE International Instrumentation and Measurement Technology Conference (I2MTC)* Proceedings, pp. 1 - 6, DOI:10.1109/I2MTC.2015.7151230

- "Design of a low cost multipurpose wireless sensor network", A. Di Nisio, T. Di Noia, C. Guarnieri Calò Carducci, M. Spadavecchia, *2015 IEEE International Workshop on Measurements & Networking (M&N)*, pp. 1 - 6, DOI: 10.1109/IWMN.2015.7322986

- "High Dynamic Range Power Consumption Measurement in Microcontroller-Based Applications", A. Di Nisio, T. Di Noia, C. Guarnieri Calò Carducci, M. Spadavecchia, *IEEE Transactions on Instrumentation and Measurement*, 2016, Volume: 65, Issue: 9, Pages: 1968 - 1876, DOI:10.1109/TIM.2016.2549818

Chapter IV
BUOY CONCEPT AND ELECTRONICS

Once defined the architecture of the real-time monitoring network, in this chapter is described the electronic front-end for the chlorophyll-*a* measurement and the system for energy harvesting, but first a brief description of the proposed concept is given.

The buoy concept is based on the typical spar buoy model (Fig. 30), which consists in a tall, thin buoy that floats upright in the water. This is commonly used in oceanographic measurements for its stability against waves and its tubular shape makes also it very easy and cheap to be implemented, since it can be made of a simple rigid plastic pipe or a metal one.

The air contained in the pipe and the low weight of inner electronics make it easily floating and it must be anchored partially submerged. The inner volume is intentionally split in two in correspondence of the waterline to create two sections. The submerged section should contain the battery packs and all the

measurement devices with the related front-end electronics (TIM) installed in the tip to perform measurements at a fixed depth, whereas the control electronics (NCAP) should be placed in the emerged section.

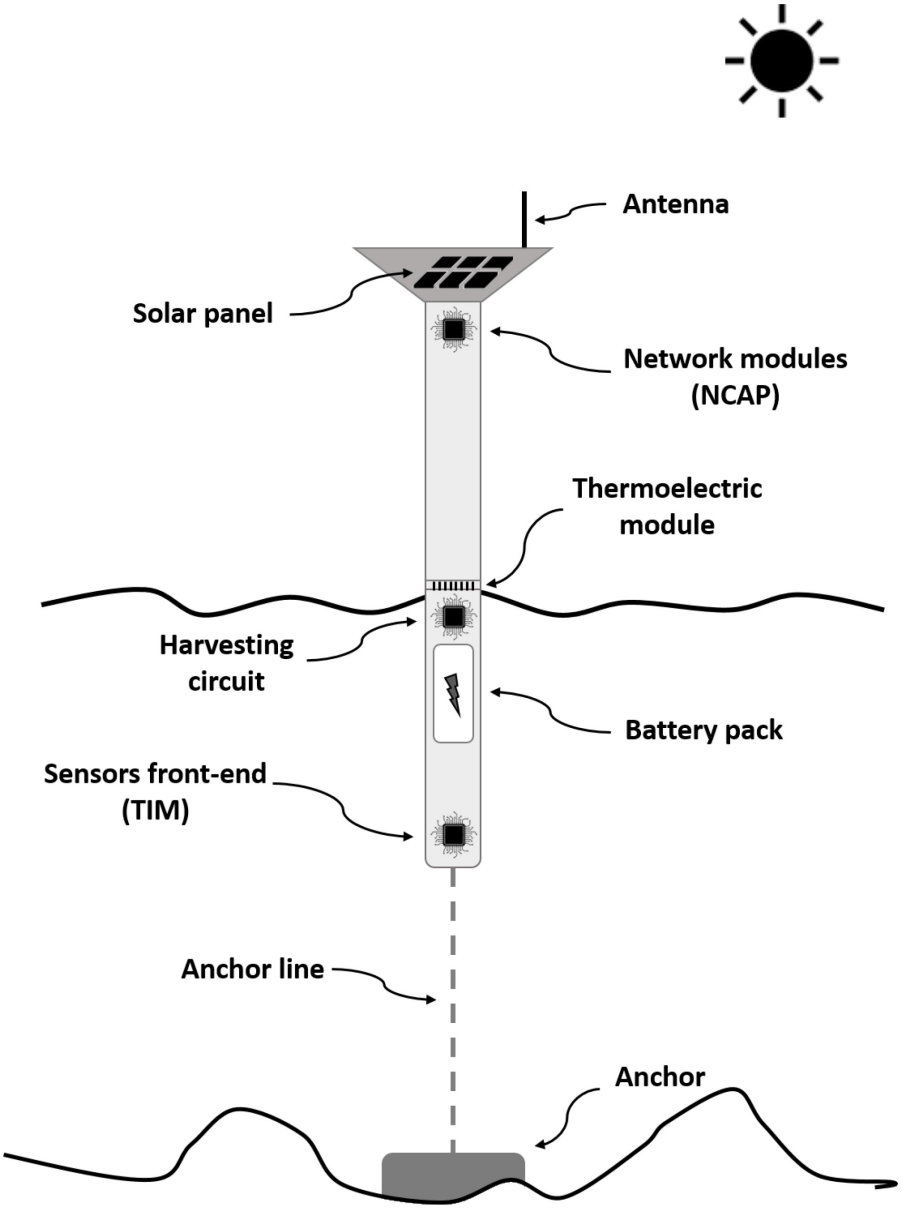

Fig. 30 – Smart buoy concept

The volume split may be created using a bulkhead made of a thermoelectric module (TEM) placed between two aluminum disks, which create two isolated chambers between which a temperature difference arises. Since the submerged chamber is always kept at the same temperature of the seawater, whereas the emerged one is subject to heating by sun irradiation, this energy harvesting element takes advantage of the resulting temperature difference to generate an electric energy that adds up to the one generated by solar panels to be furtherly used for battery charging. An alternative solution consists in placing the thermo-electric harvesting module directly beneath the solar panel, using the temperature difference directly induced by thermal conduction. At the moment, none of the two solutions was privileged and the focus was put in the characterization of the module in order to be able to better investigate the efficiency in the proposed scenarios.

IV.1 SENSOR FRONT-END

In the following, will be first described the chlorophyll-*a* and turbidity measurement method. A physics background is given together with underlying formulas. Subsequently will be described the first electronic prototype and its improvements.

IV.1.1 MEASUREMENT METHOD

In situ chlorophyll-*a* measurement relies on its intrinsic fluorescent property. Once the measurement sample is irradiated with blue light, it re-emits a part of the absorbed energy with higher wavelengths [17], typically in orange-red band (Fig. 31).

[17] Joseph R. Lakowicz "Principles of Fluorescence Spectroscopy" Springer, 2006.

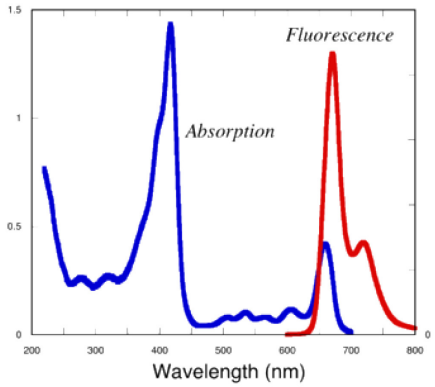

Fig. 31 – Chl-*a* in methanol: absorption (blue line) and emission (red line) spectra in arbitrary units

Thus, using a suitable light stimulus, chlorophyll-*a* molecules contained in phytoplankton cells can be induced to emit light as result of the fluorescence process, which can be subsequently collected by mean of a photodiode and used to evaluate the inner chlorophyll concentration, which can finally be used to evaluate phytoplankton concentration.

Fluorescence is a quantum effect due to photon absorption by a molecule which induces an electron transition to an excited state. If not expended in photosynthetic processes, this excited electron could undergo a thermal dissipation, drop to a lower energy level and finally decay to ground level emitting a photon with a generally lower energy, thus with higher wavelength. The difference between absorption and emission maxima wavelengths is known as Stokes shift [17], while the ratio between absorbed and emitted photons is the fluorescence quantum yield (Φ_F):

$$\Phi_F = \frac{I_a}{I_f} \tag{14}$$

The relation between the exciting light intensity I_0 and fluorescence radiation I_f is derived by considering first the amount of light absorbed in the sample, using Lambert-Beer's equation:

$$I_a = k \cdot I_0(1 - e^{\varepsilon dc}). \tag{15}$$

Introducing the chlorophyll fluorescence quantum yield in the above equation, leads to the final relation between absorbed light in the volume sample and the emitted fluorescence:

$$I_f = k \cdot \Phi_F \cdot I_0(1 - e^{\varepsilon dc}) \tag{16}$$

where k is the instrumentation setup factor, ε is the molar absorption coefficient, d is the optical path and c is the fluorescent substance concentration. Under the hypothesis of low absorbed intensity (i.e. *absorbed energy* $< 2\%$ *of excitation energy*) and very low concentration ($\varepsilon dc < 0.01$), a new relation could also be derived linearizing equation (16), by assuming to keep constant all variables except the unknown concentration c.

$$I_f = k \cdot \Phi_F \cdot I_0 \cdot \varepsilon \cdot d \cdot c = K \cdot c \tag{17}$$

Equation (17) shows a direct proportionality relation of the fluorescence intensity with Chl-*a* concentration.

Likewise in Chl-*a* fluorescence case, the nephelometric turbidity measurement also undergoes a similar linear relation. In fact, the electromagnetic behavior of a wave propagating in a colloidal solution with particles dimensions comparable with excitation light wavelength is described by the Tyndall effect [17]:

$$I_s = k \cdot \frac{N \cdot V^2}{d^2 \cdot \lambda^4} \cdot I_0 \tag{18}$$

where I_s is the intensity of the scattered light, N is the number of particles for units of volume, V is the particles volume and λ is the excitation wavelength.

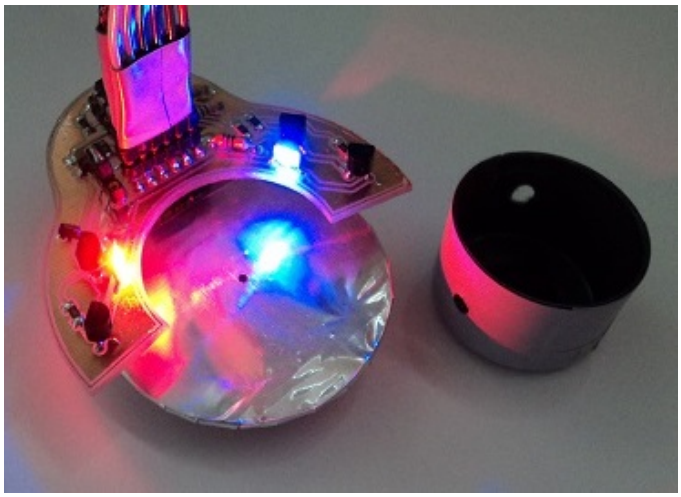

Fig. 32 – Optical sensor prototype

Sensor design guidelines follow the typical fluorescence measurement setup. A light source is placed to form an angle of 90 degrees with the light detector to avoid the stimulus light to be captured. The fluorescence signal is then collected back thanks to the isotropic emission of the sample. This setup has been also considered useful for turbidity measurement based on scattered light by suspended particles, thus using the same detector circuit with a different light stimulus. The prototype is illustrated in Fig. 32 representing the optical c-shaped transmitter, docked to the detection module. The optical transmitter is composed by a digitally controlled current generator, driving alternatively two LED sources (blue for Chl-*a* fluorescence excitation and red for turbidity) with a clean and stable square wave at the lock-in reference frequency. These LEDs couple the light in the sea water sample under test. The signal coming from the light source excites the sample and the emitted or scattered amplitude modulated (AM)

light is collected back on a photo-detector working in the fluorescence band range. Because of the resonant trans impedance amplifier (TIA) input stage, only the signal generated by synchronous emission will be amplified whereas DC components, e.g. the sunlight, will be attenuated, hence A digital circuit processes the output signal by means of an ARM *Cortex-M3* microprocessor.

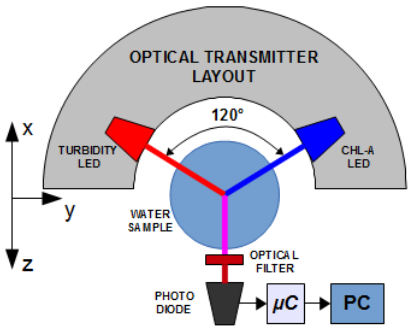

Fig. 33 Scheme of measurement setup

In Fig. 33 the scheme of the adopted experimental setup is illustrated. The circular layout was adopted to facilitate the measurements; in fact, the sample is inserted in the center of the circular layout for an efficient light source coupling.

The analog front end is integrated in the detection module printed circuit board (PCB), containing an anti-alias filter (see Fig. 34) also useful for op-amp voltage noise integration bandwidth reduction and an analog-to-digital-converter (ADC) with SAR architecture, which communicates with the µC by means of a serial SPI connection.

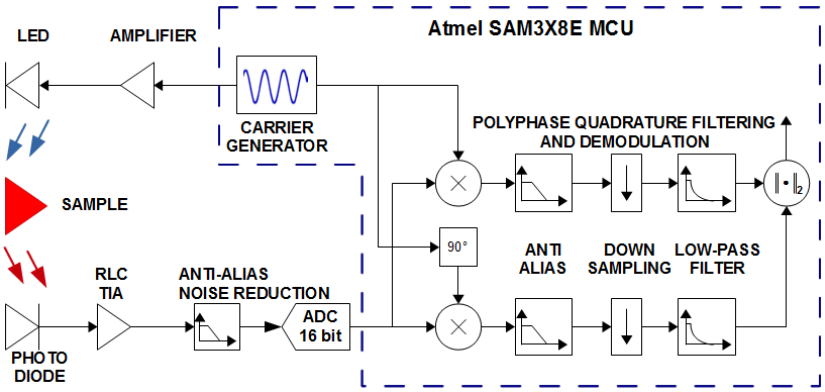

Fig. 34 – Simplified lock in implementation scheme

The digital signal processing chain has been implemented to work in batch mode for debug purposes. Once the samples of the AC signal are acquired, they have to be demodulated. Hence a high-performance algorithm has been implemented which makes possible anti-alias filtering, demodulation, down sampling and DC extraction of the signal, all in a single stage.

Finally, a variable and user-defined number of output samples are stored in the output buffer which has a default size of 1,000 samples. As last step, samples in the buffer are averaged to provide a single measurement value and to increase the SNR by a factor of $10 \cdot \log_{10} N_s$, where N_s is the number of samples to average.

IV.1.2 ELECTRONIC DESIGN

Resonant implementation of the first stage (see Fig. 35) has made practicable, with respect to discrete components needed in the classical RC TIA implementation, the use of a big gain resistor while at same time keeping the synchronous AC signal bandwidth unaffected. Despite the values of resistor and capacitor involved, the inductor value for a given resonant frequency of 1 kHz and a quality factor Q = 2π becomes now unfeasible with available discrete components, forcing its virtualization through a Miller

integrator circuit (Fig. 36) which well and easily emulates the behavior of an inductor between two variable voltage nodes.

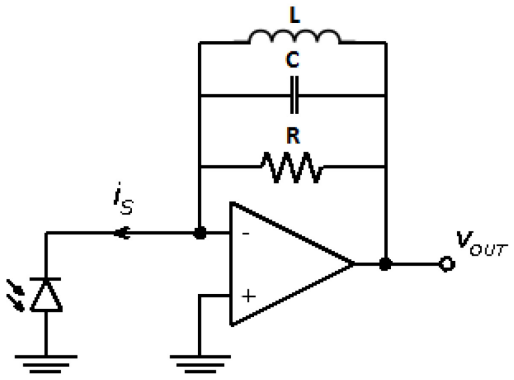

Fig. 35 – RLC Trans Impedance Amplifier

The inductor emulation is though incomplete and the dipole behaves as an inductor in series with the resistor used for Miller emulation, thus giving a maximum of 40 dB of attenuation of the DC component with respect to signal of interest (see Fig. 37).

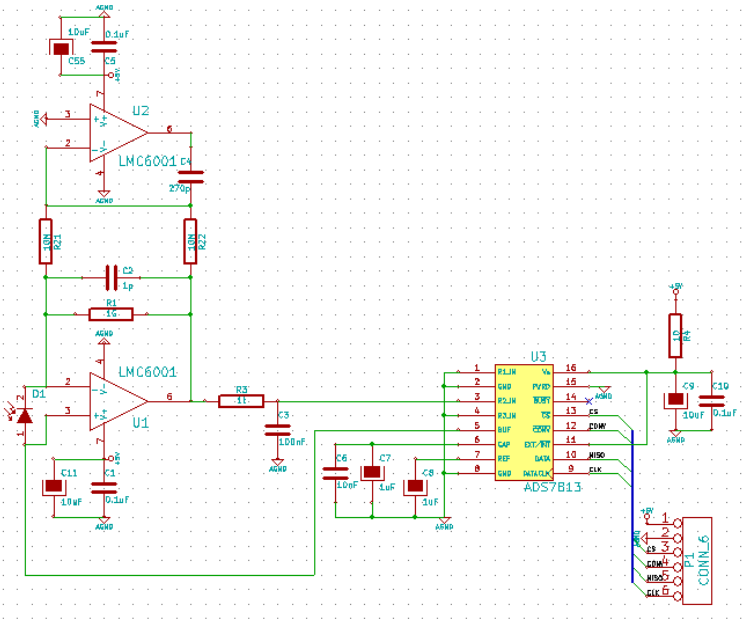

Fig. 36 –First prototype circuital scheme of the detection module

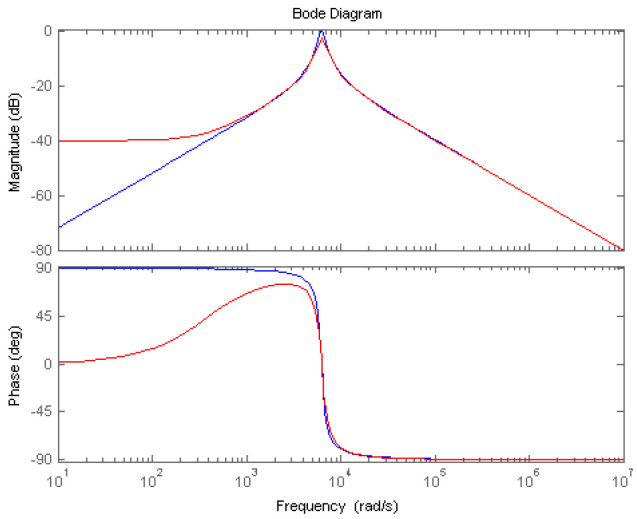

Fig. 37 . Bode diagram of normalized RLC impedance, theoretical (blue) and emulated through Miller integrator (red).

Using a lock-in modulation carrier of 1 kHz the signal is amplified at the output by the feedback system reported in Fig. 35 able to improve the best gain of 10^9. The signal passes then through a single pole anti-alias/noise-reduction filter with a time constant $\tau = RC = 10^4\ s$.

The full circuital scheme of the first prototype of optical receiver is illustrated in Fig. 36, whereas Fig. 38 shows the transmitter circuit. Through the DAC voltage, the op-amp based current generator is able to set the driving current value, in first approximation equal to the ratio of the input voltage applied to the emitter degeneration resistor. Hence a pulse width modulation (PWM) signal is used to drive alternatively the differential pair transistor bases to digitally switch the LEDs at the desired frequency, with a maximum percentage voltage overshoot included in range of 1-15%, inversely depending on the entity of the biasing current.

The TIA transfer function will then remove all the harmonics of the resulting square wave stimulus signal, allowing the only fundamental component to pass.

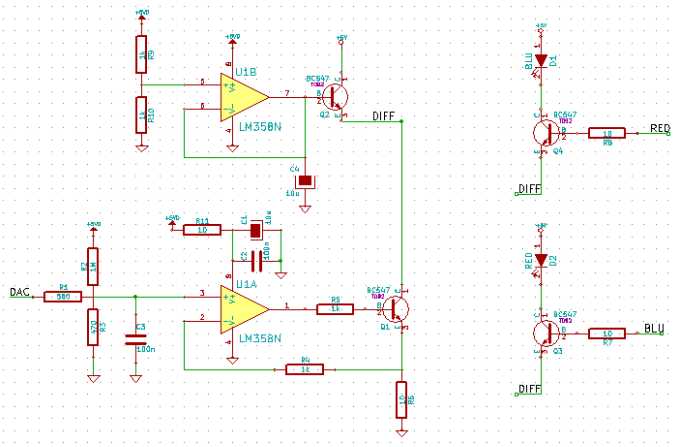

Fig. 38 First prototype circuital scheme of the transmitter module

In order to properly design the electronic front end and to evaluate different design solutions, a careful error budget analysis of the circuit need to be performed. Hence, starting from the TIA noise model described in [18] and introducing the appropriate corrections aimed to describe and take into account the effects of the RLC stage on to the noise shape, numerical simulations have been carried out using Matlab.

[18] W. Kester, “Practical Design Techniques for Sensor Signal Conditioning”, Analog Devices Technical Reference Books, vol. 5, pp. 1-40, 1999.

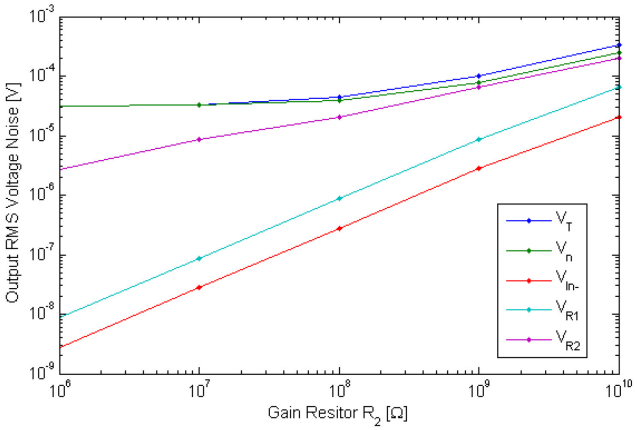

Fig. 39 – Total rms TIA output noise and its components

The resulting total root means square (rms) noise, referred to TIA stage output and described in Fig. 39 as function of the gain resistor, is calculated from the Euclidean norm of its uncorrelated individual rms noise components to properly choose a suitable ADC

$$V_T = \sqrt{\int V_n^2(f)df + V_{In-}^2(f)df + V_{R_1}^2(f)df + V_{R_2}^2(f)df} \qquad (19)$$

where V_n is the op-amp voltage noise, V_{In-} is the output voltage noise due to op-amp current noise across the gain resistor R_2, V_{R_1} and V_{R_2} are thermal noises on R_1 photo-diode shunt resistor and R_2 gain resistor respectively.

These determined values are then used to estimate the achievable stage resolution as function of its gain. In this regard, two different resolutions are shown in Fig. 40: effective resolution (ER) is calculated from the noise rms values, while the noise free code resolution (NFCR) is derived from the equivalent peak-to-peak noise, by means of the following relationships:

$$V_{PP} = 6.6 \cdot V_{rms} \qquad (20)$$

$$ER = \log_2\left(\frac{FS}{V_{rms}}\right) \tag{21}$$

$$\begin{aligned} NFCR &= \log_2\left(\frac{FS}{V_{PP}}\right) \\ &= \log_2\left(\frac{FS}{6.6 \cdot V_{rms}}\right) \\ &= \log_2\left(\frac{FS}{V_{rms}}\right) - \log_2 6.6 = ER - 2.7 \end{aligned} \tag{22}$$

where FS is the sensor Full Scale and V_{rms} is the total output referred rms.

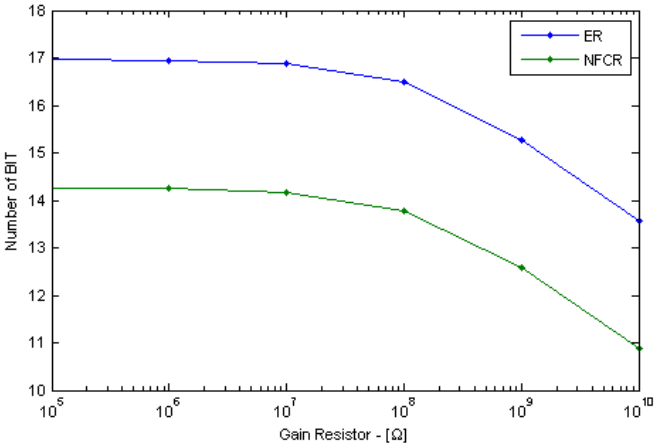

Fig. 40 . Calculated number of bits

Final calculated performances of the designed input stage are reported in TABLE V.

TABLE V.
CALCULATED RMS (NFCR) FRONT-END PERFORMANCES

Parameter	Value
Total Output Noise (V_{out})[µV]	101
Max number of BITs	15,3 (12,6)
Min detectable Current [pA]	0,18 (1)

IV.1.3 ELECTRONIC IMPROVEMENTS

After examining the results obtained with the first version of the chlorophyll-*a* sensor and reported in Chapter V, it was required the implementation of an advanced methodology for the design of analog front-end based on resonant transimpedance amplifiers that would allow to increase both the sensitivity and detectivity.

Op-Amp based transimpedance amplifiers typically use a resistor in the feedback network to set the current-to-voltage gain of the stage. In fact, since the current which flows into the input terminal of the Op-Amp is negligible, all the current i_s generated by the sensor is forced to flow in first approximation in the feedback resistor, inducing an output voltage v_o proportional to its value R. Fig. 41shows the typical TIA configuration used as a low-noise front-end for a photodiode, where the voltage at V_- equal to V_+ because of virtual short-circuit. Very often, a compensation capacitor C should be placed in parallel to R, as in Fig. 41, to guarantee adequate stability margins for the circuit, especially when large gains are required and/or the sensor exhibits high equivalent capacitance C_s [19]. In fact, in this case, without the compensation capacitor C, the Noise Gain would contain only a low frequency zero placed in $\omega_z = 1/RC_s$, intersecting with a slope of 20 dB/decade the open-loop gain of the Op-Amp, characterized by a -20 dB/decade slope due to its dominant pole. This results in a poor phase margin PM of the feedback circuit.

[19] W. Kester, "Practical Design Techniques for Sensor Signal Conditioning", Analog Devices Technical Reference Books, vol. 5, pp. 1-40, 1999

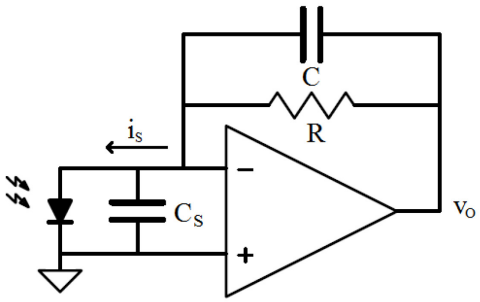

Fig. 41 – Classic Op-Amp TIA configuration

As rule of thumb, the value of the feedback resistor should be always maximized, to decrease its noise contribution and to avoid further amplification stages, which would inevitably introduce additional noise and would result in an increase of cost. For instance, halving the value of the feedback resistor R entails a 3 dB loss in the Signal-to-Noise Ratio that cannot be recovered using a second stage:

$$SNR_{R/2} = \frac{\frac{V_S^2}{4}}{4kT\frac{R}{2}\frac{\Delta\omega}{2\pi}} = \frac{1}{2}\cdot\frac{V_S^2}{4kTR\frac{\Delta\omega}{2\pi}} = \frac{1}{2}\cdot SNR_R \qquad (23)$$

where $V_S = RI_S$, SNR_R and $SNR_{R/2}$ are the Signal-to-Noise ratios corresponding to the feedback resistor value R and $R/2$ respectively, T is the temperature in kelvin, k is the Boltzmann's constant and $\Delta\omega$ is the closed-loop bandwidth of the circuit.

However, these guidelines lead to a natural trade-off between the TIA gain and the signal bandwidth, making very difficult, for instance, to design an amplification stage able to detect very weak signals using lock-in techniques. Moreover, together with the increase of the feedback resistor, an increasing deleterious antenna effect occurs, due to the presence of a high impedance node at the Op-Amp inverting input.

Taking into account all the previous considerations, a different feedback topology, based upon a T-network, can be exploited to address the issues associated to the configuration in Fig. 41.

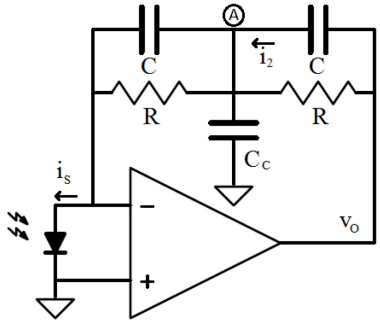

Fig. 42 – TIA configuration based on a T-network feedback

What is interesting about this configuration (Fig. 42), is its intrinsic ability, under proper conditions, to exhibit a bandpass behavior that can be easily derived using Y-Δ transform or, as in the following, using Laplace transform:

$$
\begin{aligned}
Z_{RC_1} &= Z_{RC_2} = \frac{R}{1 + sRC} \qquad Z_{C_C} = \frac{1}{sC_C} \\
v_A &= Z_{RC_1} i_s \qquad\qquad i_2 = i_s + \frac{v_A}{Z_{C_C}} \\
v_o &= v_A + i_2 Z_{RC_2} = Z_{RC_1} i_s + \left(i_s + \frac{Z_{RC_1}}{Z_{C_C}} \right) Z_{RC_2} \qquad (24) \\
v_o &= \left(Z_{RC_1} + Z_{RC_2} + \frac{Z_{RC_1} \cdot Z_{RC_2}}{Z_{C_C}} \right) i_s = \left(2Z_{RC} + \frac{Z_{RC}^2}{Z_{C_C}} \right) i_s \\
Z(s) &= \frac{v_o}{i_s} = \frac{sR^2(2C + C_C) + 2R}{(sRC + 1)^2}
\end{aligned}
$$

In fact, from (24) it is clear that the resulting transfer function $Z(s)$ has a DC gain equal to $2R$, a transmission zero in $-2/[R(2C + C_C)]$ and a double pole in $-1/(RC)$ (Fig. 43).

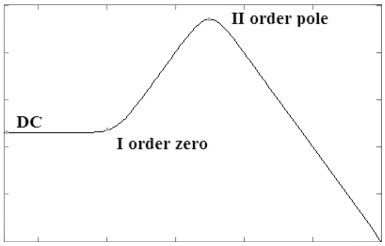

Fig. 43 – Bode plot of the transimpedance $Z(s)$

Unfortunately, different SPICE simulations show that this result is far from describing what really happens and it is not sufficient to take into account the interactions of the T-network with some relevant parasitic parameters of the circuit when it is used to close the feedback, as well as the finite gain $A_{V\,OL}$ and the finite bandwidth of the Op-Amp. It is therefore necessary to carefully derive the correct result using a more rigorous approach, starting from considering a dominant pole approximation for the open-loop transfer function of the Op-Amp:

$$v_O = A_D(v_+ - v_-) = A_D v_D \tag{25}$$

where

$$A_D(s) = \frac{A_{V_{OL}}}{1 + s/\omega_0} \tag{26}$$

In the following, to avoid confusion, the previously found expression (24) of the closed-loop transimpedance $Z(s)$ is called Z_2, whereas Z_1 is the total input impedance given by the parallel of the photodiode shunt resistor R_s, its junction capacitance C_s and the Op-Amp input capacitance C_{IN}. Consequently, Z_2 represents the closed-loop transimpedance gain of the system only under ideal conditions, i.e. when the gain of the controlled voltage source of the Op-Amp tends to infinity; in other words, it represents the asymptotic gain A_∞ of the system [20]

$$A_\infty = \left.\frac{v_o}{i_s}\right|_{A_{V_{OL}} \to \infty} = Z_2 \tag{27}$$

whereas ϑ_i is the return ratio

$$\vartheta_i = \frac{A_D\, Z_1}{Z_1 + Z_2} \tag{28}$$

Finally, a more realistic model for the closed-loop gain $G(s)$ of the TIA represented in Fig. 42 can be derived using the classic feedback theory [20]:

$$G = \frac{A_\infty\, \vartheta_i}{1 + \vartheta_i} \tag{29}$$

$$G = \frac{\omega_0\, A_{V_{OL}}\, Z_1\, Z_2}{Z_1(\omega_0\, A_{V_{OL}} + s + \omega_0) + Z_2(s + \omega_0)} \tag{30}$$

This equation is far more complex and difficult to handle than (24), in fact a more detailed analysis will show that it is a third order transfer function. Nevertheless, the expression (24) of the closed-loop gain of the circuit accurately represents its behavior, as confirmed by means of PSpice simulations.

The main problem, when dealing with (30), is that the gain is expressed as a function of 3 parameters defined over a subset *A* of $\mathbb{C}$, which gives values in $\mathbb{C}$

$$f_{R,C,C_C}\colon A_{R,C,C_C} \subset \mathbb{C} \to \mathbb{C}$$

This makes very tough the circuit design process, since the same desired feature can be obtained in first approximation with many different parameter combinations. To better understand which parameter triplet best suits designer needs, it is also necessary to derive a similar symbolic formulation for all the involved noise

[20] S. Rosenstark, "Feedback amplifier principles", Macmillan Press USA, 1986

sources, resulting in a long, error-prone procedure that can be sped up by using automated software only after completion of the hand analysis of the circuit.

In order to overcome these difficulties, a new design procedure has been derived, which will be briefly descripted in the following. The symbolic problem formulation is a powerful tool for all designers, since it can provide a detailed description of the system, from which all inferable properties depend on the mathematical skills of the designer himself. In addition, a symbolic model and thus the entire design process can be easily and completely handled using Matlab, taking also advantage of all the additional available toolboxes.

The new approach starts from a Pure Nodal Analysis (PNA) of the network, to derive a complete minimal matrix representation of the circuit, used to infer the expression of the main circuit properties (zeros, poles and peak positions) and to derive the parametric symbolic expression for all involved noise densities, in the form of deeply vectorized minimal computational blocks. Subsequently, an N-dimensional grid (where N is the number of parameters) is used to efficiently compute the previously mentioned blocks in a short time, providing $\prod_{i=1}^{N} \mathrm{M}_i$ raw circuit analysis in a single step, where M_i is the size of the *i-th* parameter vector. Afterwards, a 4–step post-processing stage refine the raw data in order to compute poles, peaks, output RMS noise and to perform design constraints evaluation. Finally, scalar design goal functions can be directly plot as 4^{th} dimensions over a tri-dimensional support for $\mathrm{N} = 3$, to provide an immediate visual inspection of the solutions space, otherwise, for $\mathrm{N} > 3$, solutions have to be reshaped and sorted, for the further extraction of the parameter N-tuple corresponding to the desired specifications.

Starting from the first prototype of TIA and trying to use the same number of components with the new T-shaped feedback network, a new photodiode amplification stage for Chl-A detection was designed, able to reach much greater values of sensitivity [21].

In the previous prototype, the second amplifier was used to emulate the behavior of an inductor, creating a RLC resonant feedback loop. However, considering a T-network feedback, its use is not necessary anymore, so the second Op-Amp is now used to double the circuit creating a fully differential TIA (Fig. 44).

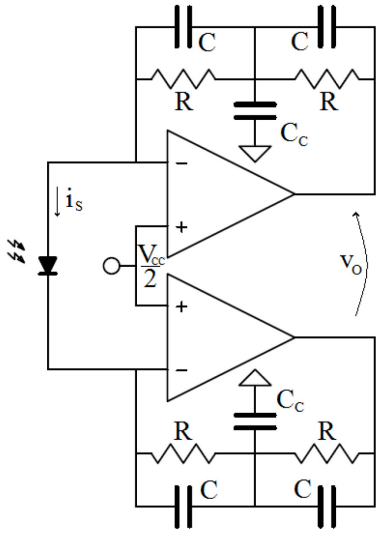

Fig. 44 – Fully differential TIA based on T-networks

This topology provides a higher immunity against interfering signals, since they appear as common mode signals which couple to the inverting input, hence they are rejected by subtraction. It also gives an implicit 2x gain factor and reduces the total input capacitance given by the photodiode junction capacitance in

[21] Keithley, "Low Level Measurements Handbook", Keithley Instruments Inc, 2004

parallel to the series of the two Op-Amp input capacitance, further increasing the gain and the quality factor.

The analysis of the previous circuit has been carried out by exploiting the special properties of two ideal elements known as Nullator and Norator [22], used to model the Op-Amps of the network. The former is a one-port element that does not permit the current to flow through it and, at the same time, maintains zero voltage across its terminals ($v = i = 0$), whereas the latter admits an arbitrary voltage and current ($v = i = arbitrary$). Combining these two elements in different configurations, two-port networks with interesting properties can be modeled, such as Nullors, but also MOS and OTAs [23] in Fig. 45.

The main advantage of this approach is that, by exploiting the properties of nullator-norator pairs, the order of the resulting system of equation can be reduced by one for each nullor.

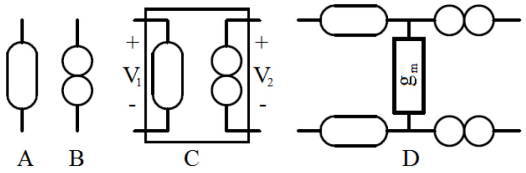

Fig. 45 – Nullator (A), Norator (B), Nullor (C) and OTA (D)

Unlike SPICE programs that use Modified Nodal Analysis to compute the stamp associated to each non-NA-compatible element, nullor-based method leads to a network of only NA-compatible elements, reducing CPU-time [23].

The circuit in Fig. 44, was realized using two LMC6001 Op-Amps from Texas Instruments, which can be modeled using a

---

22 C. Sanchez-Lopez, E. Tielo-Cuautle, "Behavioral model generation for symbolic analysis of analog integrated circuits", ISSCS 2005, doi: 10.1109/ISSCS.2005.1509920

23 E. Tlelo-Cuautle, L.A. Sarmiento-Reyes, "A Pure Nodal-Analysis Method Suitable For Analog Circuits Using Nullors", Journal of Applied Research and Technology, vol. 1, num. 3, october, 2003, pp. 235-247

nullor based voltage-controlled voltage source (Fig. 46) with gain equal to $k = g_1/g_2$ [24].

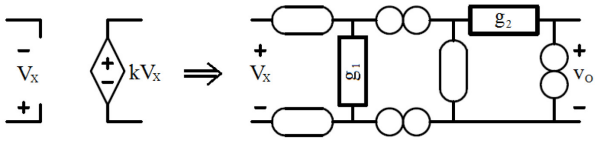

Fig. 46 – VCVS and its nullor based model

This model has been modified using data from the datasheet of the Op-Amp or from the SPICE model, in order to take into account the actual value of the dc open-loop gain $A_{V\,OL} = 8 \cdot 10^5$, the dominant pole time constant $t_1 = 2\pi \cdot 1.634\,\mathrm{s}$ and the input capacitance $C_i = 2$ pF, as depicted in Fig. 47.

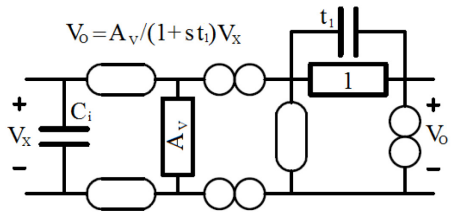

Fig. 47 – LMC6001 model

The circuit in Fig. 48 shows the complete nullor-based small signal model of the circuit in Fig. 44, where the photodiode has been replaced with its equivalent circuit given by the junction capacitance in parallel to its shunt resistance and each element has been written in the form of Y admittance ($G = 1/R$).

$$\begin{cases} Y_D = sC_D + G_D & Y_{C_i} = sC_i & Y_P = st_1 + 1 \\ Y_{RC} = sC + G & Y_{C_C} = sC_C & \end{cases} \tag{31}$$

[24] E. Tlelo-Cuautle, J. Cid-Monjaráz, "Computing symbolic transfer functions from SPICE files using nullors", Proceedings of WSEAS International Conferences, 2002, Mexico, pp. 1641-1646

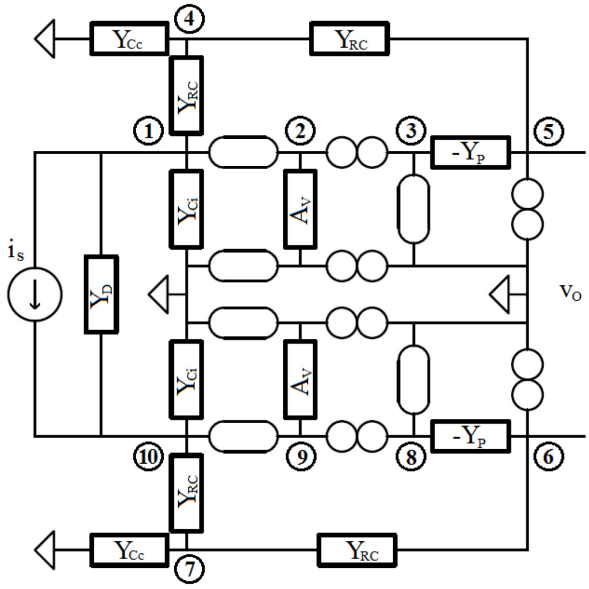

Fig. 48 – Nullor-based differential T-network TIA small signal equivalent model

Applying the two following rules

$$y_{ii} = \sum_{i=1}^{n} y_i$$
$$y_{ij} = -(y_{ii} \cap y_{jj}) \tag{32}$$

the 10x10 Y_{NA} nodal admittance matrix is written down, where subscript index i relates to node's numbers in Fig. 48:

$$\begin{bmatrix}
Y_D+Y_{RC}+Y_{C_i} & 0 & 0 & -Y_{RC} & 0 & 0 & 0 & 0 & 0 & -Y_D \\
0 & A_V & 0 & 0 & 0 & 0 & 0 & 0 & 0 & 0 \\
0 & 0 & -Y_P & 0 & Y_P & 0 & 0 & 0 & 0 & 0 \\
-Y_{RC} & 0 & 0 & 2Y_{RC}+Y_{C_c} & -Y_{RC} & 0 & 0 & 0 & 0 & 0 \\
0 & 0 & Y_P & -Y_{RC} & Y_{RC}-Y_P & 0 & 0 & 0 & 0 & 0 \\
0 & 0 & 0 & 0 & 0 & Y_{RC}-Y_P & -Y_{RC} & Y_P & 0 & 0 \\
0 & 0 & 0 & 0 & 0 & -Y_{RC} & 2Y_{RC}+Y_{C_c} & 0 & 0 & -Y_{RC} \\
0 & 0 & 0 & 0 & 0 & Y_P & 0 & -Y_P & 0 & 0 \\
0 & 0 & 0 & 0 & 0 & 0 & 0 & 0 & A_V & 0 \\
-Y_D & 0 & 0 & 0 & 0 & 0 & -Y_{RC} & 0 & 0 & Y_D+Y_{RC}+Y_{C_i}
\end{bmatrix}
\cdot
\begin{bmatrix} v_1 \\ v_2 \\ v_3 \\ v_4 \\ v_5 \\ v_6 \\ v_7 \\ v_8 \\ v_9 \\ v_{10} \end{bmatrix}
=
\begin{bmatrix} i_1 \\ i_2 \\ i_3 \\ i_4 \\ i_5 \\ i_6 \\ i_7 \\ i_8 \\ i_9 \\ i_{10} \end{bmatrix}$$

The next step consists in the reduction of the Y_{NA} matrix to its minimal representation using nullator-norator properties [24]:

- Series nullator (Fig. 49A) are virtually shorted, thus a single admittance can be written as sum of the relative columns. The resulting column is maintained, while the remaining is deleted.
- Series norator (Fig. 49B) are virtually shorted, thus a single admittance can be written as sum of the relative rows. The resulting row is maintained, while the remaining is deleted.
- Nullators and norators connected to ground (Fig. 49C) are virtually shorted to ground, thus respective columns or rows are deleted.

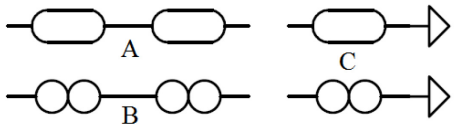

Fig. 49 – Reduction cases

The reduced 6x6 matrix Y_{PNA} is:

$$\begin{bmatrix} Y_{C_i}+Y_D+Y_{RC} & -Y_{RC} & 0 & 0 & 0 & -Y_D \\ A_V & 0 & Y_P & 0 & 0 & 0 \\ -Y_{RC} & Y_{CC}+2Y_{RC} & -Y_{RC} & 0 & 0 & 0 \\ 0 & 0 & 0 & -Y_{RC} & Y_{CC}+2Y_{RC} & -Y_{RC} \\ 0 & 0 & 0 & Y_P & 0 & A_V \\ -Y_D & 0 & 0 & 0 & -Y_{RC} & Y_{C_i}+Y_D+Y_{RC} \end{bmatrix} \cdot \begin{bmatrix} v_{1,2} \\ v_4 \\ v_5 \\ v_6 \\ v_7 \\ v_{9,10} \end{bmatrix} = \begin{bmatrix} i_1 \\ i_{2,3} \\ i_4 \\ i_7 \\ i_{8,9} \\ i_{10} \end{bmatrix} \quad (33)$$

It contains a complete representation of the circuit in the form of a system of linear equations $Y \cdot v = i$, from which all transfer functions (TF), from one input current at a given node to one output voltage at another given node, can be derived simply using Matlab syntax $v = Y \setminus i$. For instance, the differential input-output transfer function is computed as follow:

$$\begin{bmatrix} 0 \\ 0 \\ v_5 \\ v_6 \\ 0 \\ 0 \end{bmatrix} = Y \setminus \begin{bmatrix} -i_1 \\ 0 \\ 0 \\ 0 \\ 0 \\ i_{10} \end{bmatrix}, \quad \text{where} \quad \begin{cases} i_s = i_1 = i_{10} \\ v_o = v_5 - v_6 \end{cases} \tag{34}$$

giving the following relationship as v_o to i_s ratio

$$Z = \frac{v_o}{i_s} = \frac{2A_V\left(Y_{C_C} + 2Y_{RC}\right)}{(A_V + Y_P)Y_{RC}^2 + Y_{C_C}\left(Y_{C_i}Y_P + 2Y_DY_P + Y_{RC}Y_P\right) + \left(2Y_{C_i} + 4Y_D\right)Y_{RC}Y_P}$$

or made explicit with respect to variable s

$$Z(s) = \frac{A_V(4C + 2C_C) \cdot s + 4A_VG}{s^3K_3 + s^2K_2 + sK_1 + K_0} \tag{35}$$

$$\begin{aligned} K_3 = \;& t_1(C^2 + CC_C + 4CC_D + 2CC_i + 2C_CC_D + C_CC_i) \\ K_2 = \;& C(4C_D + C + A_VC + 2C_i) + (C + C_i + 2C_D + t_1G)C_C + \cdots \\ & + 2t_1\left((2C + C_C)G_D + G(C + 2C_D + C_i)\right) \\ K_1 = \;& t_1G^2 + G(2C + C_C + 4C_D + 2C_i + 2A_VC + 4t_1G_D) + (4C + 2C_C)G_D \\ K_0 = \;& A_VG^2 + G^2 + 4GG_D \end{aligned}$$

from which it's clear that $Z(s)$ is a 3rd order transfer function.

What is interesting with this approach is that all TFs can be directly computed from the schematic file without the need to perform difficult manual analysis. Even more interesting is that also the TF of each noise source is directly available, such as resistor thermal noise, current and voltage Op-Amp noises.

In fact, the complete noise model of the circuit, including resistor thermal noise, Op-Amp voltage and current noise, is easily derived using the Y matrix previously derived, because it contains all signal TFs between couples of nodes, valid also for noise sources. It means that the noise spectral density of each noise source will be shaped by the respective input-output TF.

To compute the rms noise referred to the output (RTO) due to a given source, for instance a resistor Johnson noise with spectral

density $V_R = \sqrt{4kTR}$ and $H(s)$ transfer function, the following integral should be computed, at least over an appropriate bandwidth

$$V_{R_{RMS}} = \sqrt{\frac{1}{2\pi}\int_0^{\infty}(V_R \cdot |H(j\omega)|)^2 d\omega} \tag{36}$$

but since the solutions to the $V = I/Y$ problem are impedances $Z(s)$ that relate the current I injected into a given node to the voltage V at another one, the voltage noise spectral density must be first transformed in a current noise, dividing it by the respective R value:

$$\begin{aligned} I_R &= V_R G = \frac{V_R}{R} = \frac{\sqrt{4kTR}}{R} = \sqrt{\frac{4kT}{R}} = \sqrt{4kTG} \\ V_{R_{RMS}} &= \sqrt{\frac{1}{2\pi}\int_0^{\infty}(I_R \cdot |Z(j\omega)|)^2 d\omega} \end{aligned} \tag{37}$$

All the noise sources that share a common node:

- Johnson's current noise due to the photodiode shunt resistance between nodes (1,10) in Fig. 48
- Johnson's current noise due to $R/2$ resistance (because of differential doubled output rms noise) between nodes (1,4) and (10,7)
- Op-Amp current noise

are all multiplied by the same transfer function $Z_1(j\omega)$ obtained by solving the $YV = I$ problem for $I = [-i_1, 0,0,0,0, i_{10}]$.

Similarly, the Op-Amp voltage noise spectral density is shaped by $Z_2(j\omega)$, obtained by solving the $YV = I$ problem for $I = [0, -i_{2,3}, 0,0, i_{8,9}, 0]$ and hence dividing by its equivalent

resistance, or, in an equivalent way, multiplying by g_1 in Fig. 46, i.e. A_V in Fig. 47:

$$V_{n_{RMS}} = \sqrt{\frac{1}{2\pi}\int_0^{\infty} \left(V_n \cdot |Z_2(j\omega)| \cdot A_{V_{OL}}\right)^2 d\omega} \qquad (38)$$

Last noise source is due to Johnson noise of R resistors between node (4,5) and (7,5) that is shaped by $Z_3(j\omega)$, obtained for $I = [0,0,-i_4,i_7,0,0]$. Consequently, the total RTO rms voltage noise is the sum of all the N noise contributions V_i

$$V_{RTO_{RMS}} = \sqrt{V_{0_{RMS}}^2 + \ldots + V_{N_{RMS}}^2} = \sqrt{\sum_{i=1}^{N} V_{i_{RMS}}^2} \qquad (39)$$

The above described formulas are too costly to be computed for multiple values of design parameters, as they require inefficient *for* computation loops that cannot be vectored. However, this obstacle was overcome using functional analysis tools [25], recognizing that for a given source of noise, with spectral density V_x and transfer function H_x, the RTO rms noise can be written as

[25] Norms for Signal and Systems, online: http://www.cds.caltech.edu/~macmardg/courses/cds110b/dft/dft92-ch2.pdf

$$
\begin{aligned}
V_{x_{RMS}} &= \sqrt{\frac{1}{2\pi}\int_0^{\infty}(V_x \cdot |H_x(j\omega)|)^2 d\omega} \\
&= V_x \cdot \sqrt{\frac{1}{4\pi}\int_{-\infty}^{\infty}|H_x(j\omega)|^2 d\omega} \\
&= V_x \cdot \sqrt{\frac{1}{4\pi j}\int_{-j\infty}^{j\infty}H_x(s)\cdot H_x(-s)ds} \\
&= V_x \cdot \sqrt{\frac{1}{4\pi j}\oint_{\Gamma}H_x(s)\cdot H_x(-s)ds} \\
&= V_x \cdot \sqrt{\frac{\|H_x\|_2^2}{2}} \\
&= V_x \cdot \sqrt{\frac{1}{2}\sum_{k=1}^{3}Res_{p_k}(H_x)}
\end{aligned}
\tag{40}
$$

where $\Gamma = \Gamma_R \cup \Gamma_L$ is a path that encloses the poles in the left half-plane of Fig. 50.

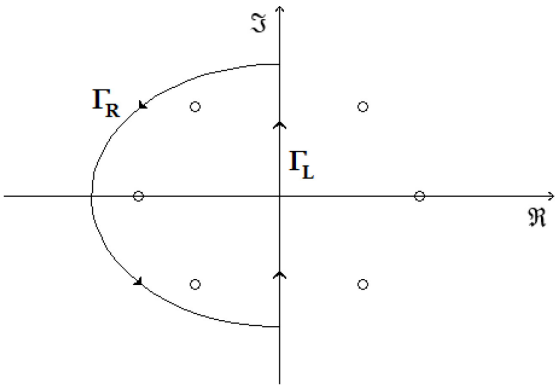

Fig. 50 – Integration contour Γ in the *s* plane.

In fact, it can be written

$$
\begin{aligned}
2\pi j \cdot \|H_x\|_2^2 &= \oint_{\Gamma} H_x(s)H_x(-s)ds \\
&= \cancel{\int_{\Gamma_R} H_x(s)H_x(-s)ds} + \int_{\Gamma_L} H_x(s)H_x(-s)ds \\
&= \lim_{R\to\infty}\left[\int_{-\pi/2}^{\pi/2} H_x\left(Re^{j\vartheta}\right)H_x\left(-Re^{j\vartheta}\right)d\vartheta + \cdots \right. \\
&\qquad \left. + \int_{-jR}^{jR} H_x(jy)H_x(-jy)dy\right] \\
&= \int_{-j\omega}^{j\omega} H_x(j\omega)H_x(-j\omega)d\omega \\
&= 2\pi j \cdot \sum_{k=1}^{3} Res_{p_k}(H_x) \\
&= 2\pi j \cdot \sum_{k=1}^{3} \lim_{s\to -p_k}[(s+p_k)H_x(s)H_x(-s)]
\end{aligned}
\tag{41}
$$

where the contour integral over Γ_R vanishes by Jordan's lemma.

Finally, the desired expression of the output noise in vector form equation is derived, which is dependent only on the value of the system poles:

$$
V_{x_{RMS}} = V_x\sqrt{\frac{1}{2}\sum_{k=1}^{3} Res_{p_k}(H_x)} = V_x\sqrt{\frac{1}{2}\sum_{k=1}^{3} \lim_{s\to -p_k}[(s+p_k)|H_x(s)|^2]} \tag{42}
$$

where $H_x(s)$ is written using an abstract symbolic pole representation of each solution to the *V = I/Y* problem. For instance, for input-output transfer function $Z_1(s)$, it is

$$
Z_1(s) = \frac{(s/z_1+1)}{(s/p_1+1)(s/p_2+1)(s/p_3+1)} \tag{43}
$$

Solutions space is now computed over a logarithmic 3D mesh-grid of parameters (Fig. 51) G, C, C_C, but it can also be computed over an *n*-dimensional grid for *n* parameters. Choosing $\mathrm{M} = 100$ elements per parameter vector, it leads to a grid of MxMxM $= GxCxC_C = 10^6$ parameters combinations.

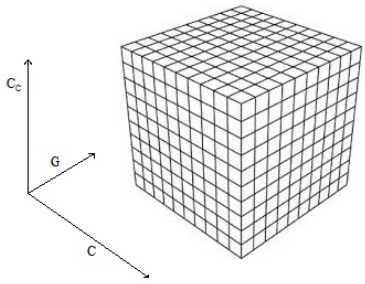

Fig. 51 – Mesh-grid for computation

For each combination of the three parameters, the associated poles and zero from symbolic solutions to the input-output transfer function (35) can now be derived. These solutions are then used to compute the resonant peak frequency using

$$Z(j\omega) = \|Z\|_\infty \Longrightarrow \frac{d|Z(j\omega)|}{d\omega} = 0 \tag{44}$$

and the relative total output RMS noise

$$V_{RTO_{RMS}} = 20 \cdot log_{10} \sqrt{\sum_{i=1}^{N} V_i^2{}_{RMS}(G, poles, zeros)} \tag{45}$$

At this step, design constraints b_i are applied to the grid using binary logic, to reduce the solution space. For first it is required to all valid solutions to be stable and the presence of the natural frequency within a 30% of the frequency of interest, with a given quality factor. Subsequently those solutions that have a $\|Z\|_\infty$ norm with the following properties are searched: a peak within 1%

of the frequency of interest f_i and a given range for both the impedance peak value Z_{pk} and the DC impedance value Z_{DC} in dB

$$b_1 = \mathrm{Re}(poles) < 0 \qquad b_5 = f_{p,min} \leq 0.01 \cdot f_i$$
$$b_2 = f_{n,min} \leq 0.3 \cdot f_i \qquad b_6 = Z_{DC} \leq 155$$
$$b_3 = 1.5 \leq Q \leq 10 \qquad b_7 = 200 \leq Z_{pk} \leq 230$$
$$b_4 = b_1 \wedge b_2 \wedge b_3 \qquad b_8 = b_5 \wedge b_6 \wedge b_7$$

where f_p and f_n are respectively the peak and the natural frequency associated to the circuital solution with a given combination of the three parameters G, C, C_c. The final binary solution matrix is given by

$$b = b_4 \wedge b_8 \tag{46}$$

Using three parameters it is easy to visualize a desired 4D function as a color map over a 3D grid. In order to best choose parameter ranges, the numerical computation is iterated two times, the first using an extended range and the second using maxima and minima for each parameter in the solution set:

$$\begin{matrix} 10^{-9} \leq G \leq 10^{-2} \\ 10^{-12} \leq C \leq 10^{-9} \\ 10^{-12} \leq C_C \leq 10^{-6} \end{matrix} \quad \Rightarrow \quad \begin{matrix} 8.1 \cdot 10^{-8} \leq G \leq 7.9 \cdot 10^{-7} \\ 8.1 \cdot 10^{-12} \leq C \leq 4.3 \cdot 10^{-11} \\ 1.3 \cdot 10^{-8} \leq C_C \leq 1.6 \cdot 10^{-7} \end{matrix}$$

Values in the given range can be selected to have a homogenous distribution over a linear or logarithmic scale, or using discrete values of commercial components to minimize costs.

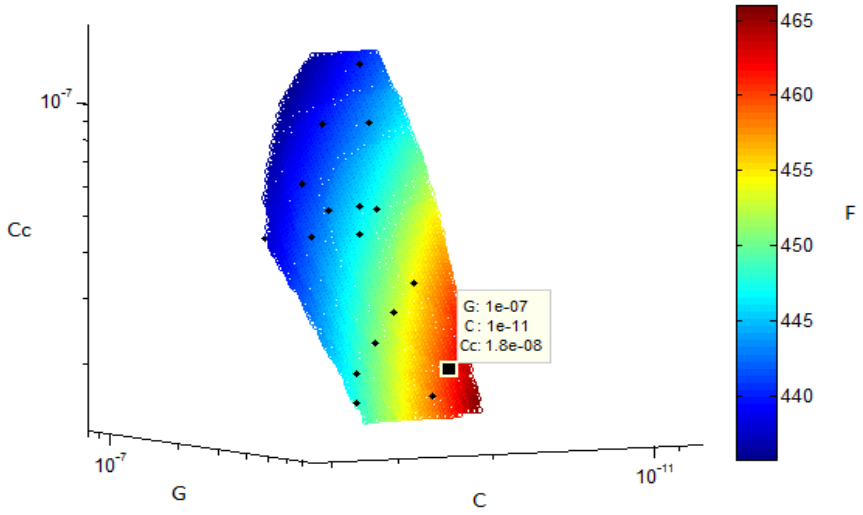

Fig. 52 – Figure of merit F_{dB} in color map and adopted solution among combinations of commercial elements (black dots)

Using commercial component values, except for $C_C = 15 + 3.3 = 18.3$ nF that is a combination, a final design parameters' triplet is selected in this project and highlighted in Fig. 52 over the solution set, where colors are used to map the dB value of our design figure of merit:

$$F = \frac{Sensitivity}{Detectivity} = \frac{Z_{pk}}{V_{RMS}/Z_{pk}} = \frac{Z_{pk}^2}{V_{RMS}} \qquad (47)$$

Hence, design parameters and associated DC and Peak gain, as long as the total output noise are:

$$R = 1/G = 10\ \text{M}\Omega \qquad Z_{DC} = 152\ \text{dB}\Omega = 40\ \text{M}\Omega$$
$$C = 10\ \text{pF} \quad \Rightarrow \quad Z_{pk} = 216\ \text{dB}\Omega = 63\ \text{G}\Omega$$
$$C_C = 18.3\ \text{nF} \qquad V_{RMS} = -29.3\ \text{dBV} = 34\ \text{mV}$$

For a signal at the frequency peak, this combination leads to a sensitivity S equal to Z_{pk} and a detectivity D equal to the ratio of the total rms output noise to the signal gain:

$$S = Z_{pk} = 63 \cdot 10^9 \text{ V/A}$$
$$D = \frac{V_{RMS}}{Z_{pk}} = 543 \text{ fA} \tag{48}$$

with an input dynamic range over 5 V of almost 80 pA.

To validate the procedure, a compared analysis of the symbolical circuit representation in Matlab and in PSpice was performed. A simulation in PSpice was first run using device library models provided by the manufacturer (for TI LMC6001 and Osram SFH2701), subsequently the magnitude and the frequency vectors were exported, using the latter as computational base in Matlab.

A clear match between the results of the symbolic method and the SPICE simulation is visible in Fig. 53, except for an error of less than 1% in the peak region and a deviation at high frequencies due to unmodeled higher order Op-Amp poles.

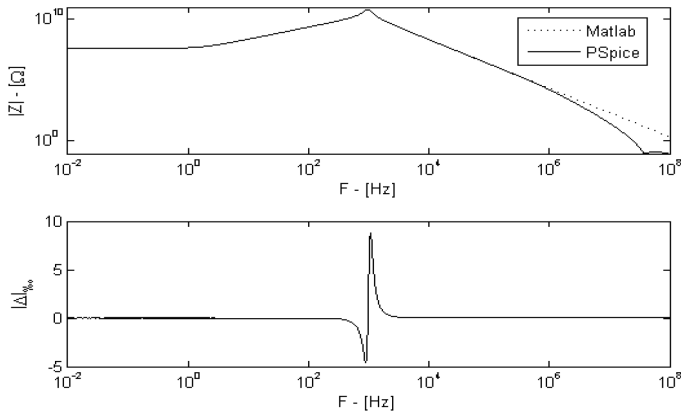

Fig. 53 – Comparison between Matlab and PSpice simulations and relative percentage error $|\Delta|_{‰}$.

For sake of clarity, a comparison between the results provided by PSpice simulations and the symbolic analysis was also performed in terms of noise performance of the circuit (Fig. 54). Resistor Johnson noise is directly computed in PSpice, whereas for

the Op-Amp current and voltage noise contributions a hybrid approach was used, since the manufacturer does not provide the SPICE noise model.

Thus, the values from LMC6001 datasheet were used ($V_n = 22 \cdot 10^{-9}$ V/$\sqrt{\text{Hz}}$, $I_n = 1.3 \cdot 10^{-16}$ A/$\sqrt{\text{Hz}}$), together with PSpice computed TFs to obtain the actual noise spectral densities of the Op-Amp noise contributions.

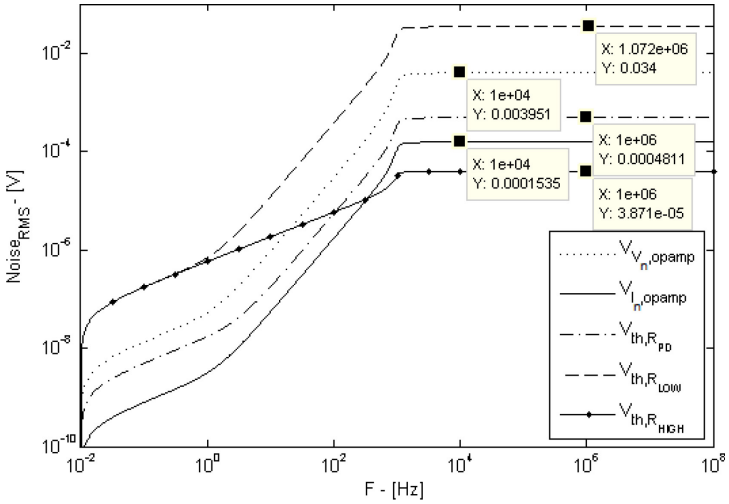

Fig. 54 – PSpice cumulative rms noise for each noise source

At high frequency (i.e. for f that tends to infinity), the cumulative rms noise for each source considered in Fig. 54 matches the result of the corresponding symbolic analysis (TABLE VI) where the main contribution to the total output rms noise composition results to be given by feedback resistors R_{LOW} directly connected to the photodiode.

In Fig. 55 a comparison of time domain simulations of the circuit response to an input square wave and a current step respectively was reported, from which a small difference between the two responses obtained with PSpice and Matlab may be

observed only during the transient phase, as it rapidly vanishes in about two milliseconds.

TABLE VI.
COMPARISON OF RMS OUTPUT NOISE FOR THE TWO METHODS

Symbol	Description	PSpice [mV]	Matlab [mV]
V_N	OpAmp Voltage Noise	4.2	3.95
I_N	OpAmp Current Noise	0.153	0.153
R_{PD}	Photodiode Johnson Noise	0.480	0.481
R_{LOW}	Low-side Resistor Johnson Noise	33.9	34
R_{HIGH}	High-side Resistor Johnson Noise	0.038	0.038

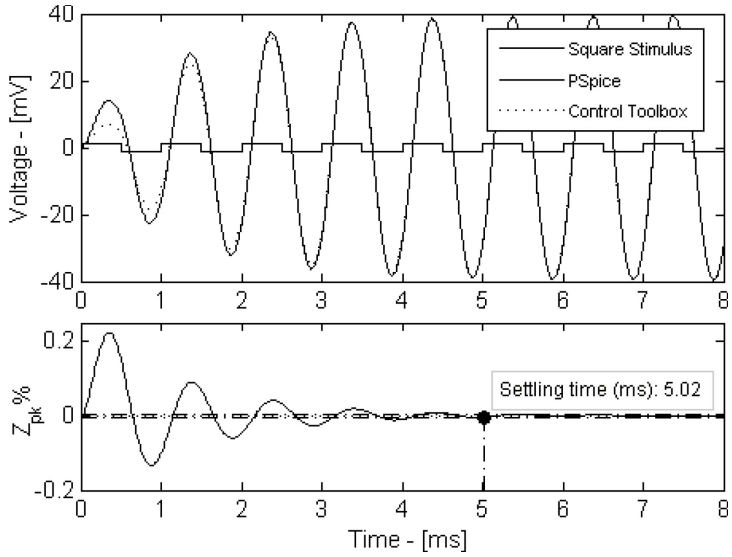

Fig. 55 - Comparison between system response to 1 pA @ 1 kHz square wave (top) and step response (bottom), computed using Matlab Control System Toolbox and PSpice.

The resulting 40 mV amplitude of the output signal in Fig. 55 due to a 1 pA square wave, corresponds to a gain G' equal to 40 GΩ, that is less than the one computed and expected of

$G = Z_{pk} = 63$ GΩ. However, this result is simply due to the use of a square wave stimulus in place of sine one, which is a common approach when dealing with LEDs. In fact, the reduced gain is consistent with the magnitude of the first coefficient c_1 in the Fourier series expansion of the square wave:

$$\begin{aligned} c_n &= \frac{4\,A_{pp}/2}{n\pi} \Longrightarrow \Big|_{n=1} \frac{4 \cdot 0.5}{\pi} = 0.6366 \\ G' &= 63 \cdot c_1 \cong 40 \text{ GΩ}. \end{aligned} \tag{49}$$

IV.2 THERMOELECTRIC HARVESTING

As said previously, this topic was not fully explored and is currently still under investigation. The main idea is to take advantage of the temperature difference between the seawater and the heated solar panel using a thermoelectric module.

Thermoelectric modules (TEM) are gaining a constant interest in the energy harvesting context, since they are very cheap and able to power autonomous nodes in sensor networks. Nevertheless, this advantage has a despicable counterpart in the lack of datasheet information useful for a correct design.

TEMs are typically characterized by the manufacturer in a handful of operating conditions (commonly two or three), from which is very difficult to derive their efficiency in different conditions. Furthermore, in energy harvesting applications the available temperature drops are small if compared to those for which they are designed and operating conditions may also vary in time, making desirable an improved knowledge of the dependence of their electrical and thermal parameters with working conditions. This information would be very useful for design purposes, running energy harvesting simulations in

different operating scenarios to perform a more accurate and reliable energy budget.

For this purpose, a characterization method has been implemented and reported in the following, which can provide a detailed description of the dependence of internal parameters with both the temperature of the cold and the hot surface of the module.

IV.2.1 THEORETICAL BACKGROUND

TEMs behavior is based upon three thermodynamically reversible effects, namely Seebeck, Peltier and Thomson effects, which differ among them only because of the way they manifest themselves; but actually they all have a common ground and are related to the Seebeck coefficient.

- Seebeck effect

  This effect appears as an electromotive force $\boldsymbol{E}_{emf}$ in a material in response to a temperature gradient $\boldsymbol{\nabla} T$,

$$\boldsymbol{E}_{emf} = -s\boldsymbol{\nabla} T \tag{50}$$

  where s is the absolute Seebeck coefficient, or thermoelectric power. Equation (50) is the basic principle for power generation in TEG modules. This voltage source extends the Ohm's law taking also into account the observable current in absence of measurable voltages. Its differential form is:

$$\rho \boldsymbol{J} = \left(-\boldsymbol{\nabla} V + \boldsymbol{E}_{emf}\right) \tag{51}$$

  Integrating out equation (50), an expression of the voltage resulting on the terminals of a thermoelectric module in open circuit conditions is derived. For instance, when exposed to a temperature difference ΔT between its junctions, a TEG will exhibit a proportional voltage:

$$V_\alpha = \alpha \Delta T \tag{52}$$

where α is the relative Seebeck coefficient. More generally, when a TEM is supplied by a current, the measurable voltage is derived integrating out equation (51):

$$V = V_R + V_\alpha = R_{in} I + \alpha \Delta T \tag{53}$$

Equation (53) is composed by two different contributions: the voltage drop V_R on the internal resistance R_{in} and the thermoelectric one V_α.

- Peltier effect

It is the dual of the Seebeck effect; it appears when a current I flows in a junction of different conductors. This effect, characteristic of the TEC modules, induce a local heat flux q emitted or absorbed depending on the current direction

$$q = \Pi I = \alpha I T \tag{54}$$

where Π is the relative Peltier coefficient of the junction and T is its absolute temperature. The last term in (54) follows from the relation between the Seebeck and Peltier coefficients, i.e. $\Pi = \alpha T$.

- Thomson effect

This plays a minor role because it is due to the Seebeck coefficient dependence with the temperature, and appears as a distributed Peltier effect in a conductor exposed to a temperature gradient. Although it is an interesting physical topic, in many practical cases it is not taken into account since its effect is generally negligible if compared to the other ones.

In some cases, however, the relationship between α and the temperature T should be considered because it affects the

performance of TEG modules operating in scenarios with dynamic working conditions.

- Figure of Merit Z

The thermoelectric figure of merit Z is a parameter which summarizes the bulk material proprieties allowing the comparison among TEM modules realized with different materials, dimensions and internal architectures. It is defined as

$$Z = \frac{\alpha^2 \Theta}{R_{in}} \tag{55}$$

Its expression (55) requires the knowledge of the relative Seebeck coefficient α, of the internal electrical resistance R_{in} and of thermal resistance Θ. Alternatively, the same meaning is given to a dimensionless parameter $Z\bar{T}$, where $\bar{T}$ is the average absolute temperature between the two faces of the module.

As a matter of fact, a TEM behaves like a heat engine (Fig. 56) that converts the electrical energy in the thermal one and vice versa according to the following relation:

$$|q_{em}| = |q_{abs}| + |VI|, \tag{56}$$

where q_{em} and q_{abs} are respectively the emitted and absorbed heat flux from the module's faces.

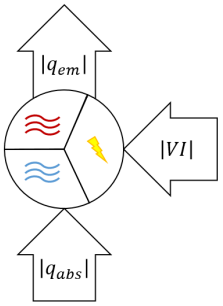

Fig. 56 - Concept diagram of a heat engine

The figure of merit can thus be though as an indicator of the conversion efficiency of energy processes involved, since its value grows as the electrical resistance decreases. In fact, all the three previously described physical processes are entirely reversible, conversely the energy dissipated by Joule effect on the internal resistance cannot be recovered. For this reason, the TEM conversion efficiency is the Carnot efficiency reduced by a factor which is function of the material's figure of merit [26]. Hence Z quantifies the ratio of thermoelectric effects to thermal effects, or equivalently of reversible to non-reversible processes.

Scientific literature includes different methods for the figure of merit assessment, which usually implies the use of different measurement principles for the determination of each parameter it is composed by. Many of them are inspired by the Harmann method. For example, one approach, known as *"modified Harmann method"* [27], or Buist transient method, allows a direct estimation of Z with a single principle exploiting the different time constants of the electrical and thermal response. The main drawback of the cited method is that it is suitable only under specific conditions that cannot be obtained during normal operating conditions thus not allowing a full characterization of TEM modules. Generally, the Harmann method is valid under the hypothesis of thermal equilibrium

$$T_h \approx T_c \approx T_a. \tag{57}$$

---

26 K. Hee Seok, L. Weishu, C. Gang, C. Ching-Wu, R. Zhifeng, "Physics Relationship between thermoelectric figure of merit and energy conversion efficiency", Proc Natl Acad Sci U S A. 2015 Jul 7; 112(27): 8205–8210. doi: 10.1073/pnas.1510231112

27 R. J. Buist, "Methodology for testing thermoelectric materials and devices", in CRC Handbook of Thermoelectrics, D. M. Rowe, Ed. Boca Raton, FL: CRC, 1995, pp. 189–209.

- Thermal Resistance Measurement

As already mentioned, among the three parameters of equation (55) the thermal resistance Θ results to be the less immediate to be measured, requiring a greater effort both in terms of number of temperature probes, as well as in the necessary readout electronics and mechanical parts for the realization of the measurement setup.

Before describing the method developed by the authors, it is convenient to find a suitable expression for the thermal resistance. Let start from the one-dimensional Fourier heat equation in steady state

$$q = -\kappa A \frac{dT}{dx} \tag{58}$$

where q is the heat flux, κ is the thermal conductivity, A is the cross-sectional area of heat flux path, dx and dT are respectively the infinitesimal increments in position and temperature in the flux direction. Integrating out (58), leads to a thermal equivalent of the Ohm's law [28],

$$\Delta T = \Theta \cdot q \quad \leftrightarrow \quad V = R \cdot I \tag{59}$$

where Θ is the thermal resistance analogous to electrical resistance R, heat flux q and temperature difference ΔT are respectively analogous to the electric current I and voltage V at terminals.

[28] S. Lineykin and S. Ben-Yaakov, "Modeling and Analysis of Thermoelectric Modules," in IEEE Transactions on Industry Applications, vol. 43, no. 2, pp. 505-512, March-april 2007. doi: 10.1109/TIA.2006.889813

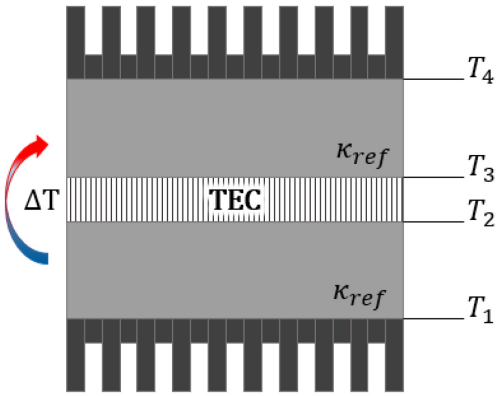

Fig. 57 – General scheme for the measurement of the thermal resistance Θ

It is therefore clear from (59) that the determination of Θ for any material requires the measurement of, at least, two different contributions (ΔT and q). In presence of an active element like a TEM, made by different coupled materials, it is not sufficient to estimate the heat flux on one face only since the energy balance involves also the electrical power. Therefore, the emitted flux is equal to the absorbed one only if $|VI| = 0$, in all other cases it is necessary to determine the electrical power and both emitted and absorbed heat flux, thus acquiring four temperature measurements.

Following the approach proposed in [29], both heat fluxes in (60), respectively q_{em} for the hot side and q_{abs} for the cold one, may be expressed as an energy balance between the Peltier effect, the heat conduction and Joule effect due to the injected current,

$$\begin{aligned} q_{em} &= \alpha I T_h - \frac{\Delta T}{\Theta} + \frac{I^2 R}{2} \\ q_{abs} &= \alpha I T_c - \frac{\Delta T}{\Theta} - \frac{I^2 R}{2} \end{aligned} \tag{60}$$

[29] T. A. Ajiwiguna, A. Ismardi, S. Y. Kim, "Measurement System for Thermoelectric Module", IEEE I2MTC 2015 Proceedings, 2015

Considering the heat flux both emitted and absorbed by a TEC module, it is possible to derive the average heat flux $\bar{q}$ to eliminate the contribution due to the Joule effect

$$\bar{q} = \frac{(q_{em} + q_{abs})}{2} = \alpha I \frac{(T_h + T_c)}{2} - \frac{\Delta T}{\Theta} \tag{61}$$

where the heat fluxes may be determined using the scheme in Fig. 57, measuring four temperatures and using a reference medium with known thermal conductivity κ_{ref}. It is

$$\begin{aligned} q_{em} &= \frac{\kappa_{ref} A (T_3 - T_4)}{L} = \frac{T_3 - T_4}{\Theta_{ref}} \\ q_{abs} &= \frac{\kappa_{ref} A (T_2 - T_1)}{L} = \frac{T_2 - T_1}{\Theta_{ref}} \end{aligned} \tag{62}$$

where A is the medium area, L is its thickness and $\theta_{ref} = L/(\kappa_{ref} A)$ is recognized as the known thermal resistance of the reference medium. Afterwards, T_h and T_c can be directly computed considering the temperature drop on ceramic faces of the TEC module

$$\begin{aligned} T_h &= T_3 + q_{em} \Theta_{cer} \\ T_c &= T_2 + q_{abs} \Theta_{cer} \end{aligned} \tag{63}$$

where Θ_{cer} is the typical thermal resistance of the TEM ceramic faces.

Finally, solving (61) with respect to Θ, it is possible to derive a measurement formula for the unknown thermal resistance

$$\Theta = \frac{2\Delta T}{\alpha I (T_h + T_c) - (q_{em} + q_{abs})} \tag{64}$$

To overcome the limits of the above described methods, an extensive unified one was proposed which relies on a modified version of the Buist method integrated with the thermal one. The

proposed unified method can provide a detailed description of the three parameters that compose the figure of merit Z with respect to variations of the operating conditions, i.e. the temperature of both side of the module.

The proposed method consists in placing the TEM module under test between to heat-flux sensors, each one made stacking two metal layers for temperature sensing with an interposed medium with known thermal conductivity κ_{ref}, while varying the temperature of the two sides sourcing it with an adequate current. When the desired operating conditions are met, a rapid current variation is applied and the following quantities are measured: the emitted and the absorbed fluxes (q_{em} and q_{abs}), the temperature at cold and hot side (T_c and T_h), the voltage V_L and the current I at its terminals.

Although all above parameters are measured at the same time, in the following they are discussed separately to avoid confusion between electrical and thermal ones.

IV.2.2 ELECTRICAL MEASUREMENT

Once the module reaches a steady-state condition, the voltage V_L at its terminals is measured along with the current I flowing in it using a series shunt resistor R_S. In this condition, the total voltage resulting at the power supply output terminals is

$$V(I, \Delta T) = V_S + V_L = R_S I + R_{IN} I + \alpha_S \Delta T \tag{65}$$

Then, if a rapid current variation, fast enough to not interfere with its thermal steady-state, is applied in a time window τ_{el} which is at least one order of magnitude smaller than the thermal time constant τ_{th}, than $V_{th} = \alpha_S \Delta T$ may be considered constant in such window and the total voltage (65) may be considered dependent only on the current supplied, hence on the electrical response of

the module. Therefore, the resulting voltage at the terminals of the module under test is

$$V_L(I) = R_{IN}I + V_{th} \quad \leftrightarrow \quad \tau_{th} \gg \tau_{el} \tag{66}$$

The proposed current variation consists in a current sweep from the value I_{st} it has in the steady-state condition up to its opposite $-I_{st}$. Using (66), this current sweep produces a line drawn in the I-V plane, as shown in Fig. 58, where the slope is given by the internal electrical resistance R_{IN} of the module and V_{th} is its intercept with the ordinate axis, both referred to a given temperature T_c and T_h.

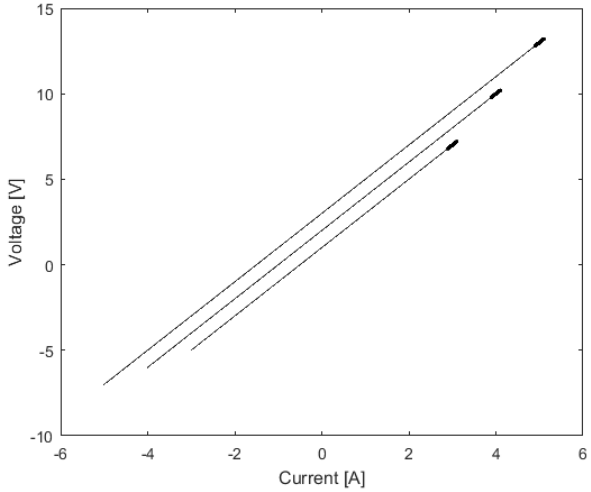

Fig. 58 Qualitative I-V plot for three different bias point of the current sweep method (solid) vs. small signal one (bold)

The consistence of the method has been validated using also a different current profile that produce the same results, but consists in a small sine signal i_{ss} added to the steady-state current I_{st}, that can be considered to all effects as a perturbation around the bias point. From the theoretical point of view, such a small current does not require to satisfy the condition on the thermal time constant, since it is generally negligible with respect to I_{st}. In first

approximation, this would seem a better approach, but the choice of a current sweep as current profile provides far more uniform results and a higher reliability in the estimation of both the involved parameters.

This statement can be easily demonstrated analytically, observing that equation (66) consists in a linear regression problem where a given set of n points (X_i, Y_i), in this case (I, V_L), is used to find the best-fit line $\widehat{Y}_\iota = a + b\widehat{X}_\iota$, trying to minimize the sum of squared errors $SSE = \sum\left(Y_i - \widehat{Y}_\iota\right)^2$. The regression slope b, the intercept a and respective standard errors are computed using the following expressions [30], where $\bar{X}$ denotes the mean value of X, $SSx = \sum_{i=1}^{n}(X_i - \bar{X}_\iota)^2$ is the sum of X squared errors, s_X^2 is the sample, not population, variance of X and $s_{y,x}^2$ is the error variance.

$$b = \frac{\mathrm{Cov}(X,Y)}{\mathrm{Var}(X)} = \frac{\sum_{i=1}^{n}(X_i - \bar{X}_\iota)(Y_i - \bar{Y}_\iota)}{\sum_{i=1}^{n}(X_i - \bar{X}_\iota)^2} \tag{67}$$

$$a = \bar{Y} - b\bar{X} \tag{68}$$

$$\sigma_b^2 = \frac{s_{y,x}^2}{SSx} = \frac{SSE}{(n-2)(n-1)\cdot s_X^2} \tag{69}$$

$$\sigma_a^2 = s_{y,x}^2\left(\frac{1}{n} + \frac{\bar{X}^2}{SSx}\right) = \sigma_b^2\left(\frac{(n-1)\cdot s_X^2}{n} + \bar{X}^2\right) \tag{70}$$

From equation (70), it is immediate to see that the uncertainty σ_a in the estimation of the intercept a for a given σ_b, increases linearly together with the samples standard deviation s_X and with the mean value $\bar{X}$, which is always zero if a symmetric current sweep is used. Conversely, $\bar{X}$ equals I_{st} when using a small signal

[30] Douglas C. Montgomery, George C. Runger, "Applied Statistics and Probability for Engineers", John Wiley & Sons, Inc., pp. 379-384

current profile and this produces higher errors for increasing values of steady-state currents. Similarly, the uncertainty σ_b in the estimation of the slope b is inversely dependent on the variance of X and increases as long as the samples tend to form a spot instead of spreading on the plane. This indeed means that using a symmetric current sweep, hence acquiring wider spread samples, leads to reduced errors in the estimation of fit parameters with respect to the small signal method, but also that the sweep method has a decreasing uncertainty in the slope estimation for increasing currents, whereas the small-signal method has a constant uncertainty.

After computing the standard deviations σ_a and σ_b, if the estimation errors ϵ_i are normally and independently distributed with mean zero and variance σ^2, the $100(1-\alpha)\%$ confidence intervals on the slope and intercept can be expressed considering that the errors in the estimations of the same are both distributed as t random variables with $n-2$ degrees of freedom.

$$\begin{aligned} |\hat{a}-a| &\leq u_{V_{th}} = t_{\alpha/2,n-2}\sigma_a \\ |\hat{b}-b| &\leq u_{R_{IN}} = t_{\alpha/2,n-2}\sigma_b \end{aligned} \tag{71}$$

If the applied current sweep is not sufficiently fast to satisfy equation (66), both because of an erroneous over-estimation of the module thermal time constant or because of intrinsic limits in the acquisition speed of the implemented test, corrections may be applied to the acquired signals. In fact, it can be shown that a quadratic term compares in the LKV equation, that induce a bending of the I-V line while the current varies. In this case, all the acquired values can still be used for parameters estimation, but the actual slope is the one at the beginning of the sweep, before the bending appears.

Hence, if (66) is weakly satisfied, a linear regression with pure quadratic formula $\widehat{Y_i} = a + b\widehat{X_i} + c\widehat{X_i}^2$ may be applied and the slope b' and intercept a' may be computed as follow

$$\begin{aligned} b' &= \left.\frac{dY_i}{dX_i}\right|_{X_0} \\ a' &= Y_0 - b'X_0 \end{aligned} \tag{72}$$

where

$$\begin{aligned} X_0 &= I_{st} \\ Y_0 &= V_{L_{st}} \end{aligned} \tag{73}$$

IV.2.3 THERMAL MEASUREMENT

To satisfy (66), the thermal transfer function of the module has been preliminarily estimated making use of an Autoregressive Exogenous (ARX) method included in the MATLAB® System Identification Toolbox.

After applying a current step $I(t)$, the four temperatures indicated in the setup in Fig. 57 are measured and composed to create two differential temperature signals, where ΔT_{32} should be most representative of the response of the module itself and ΔT_{41} should also consider the response of system of which it is part.

$$\begin{aligned} \Delta T_{41}(t) &= T_4 - T_1 \\ \Delta T_{32}(t) &= T_3 - T_2 \end{aligned} \tag{74}$$

These are later used to estimate two transfer function $H_{\Delta T}$, expressed as the Laplace transform of a first order system, where $A\tau_{th}$ is the DC gain.

$$\mathrm{H}_{\Delta \mathrm{T}}(s) = \frac{\mathcal{L}[\Delta \mathrm{T}(t)]}{\mathcal{L}[\mathrm{I}(t)]} = \frac{A}{s + \frac{1}{\tau_{th}}} \quad \left[\frac{^{\circ}\mathrm{C}}{\mathrm{A}}\right] \tag{75}$$

Since the output differential temperature time constant at external sides of the heat-flux sensors is always greater than the one at direct contact with the TEM because of the heat propagating time in a given medium (i.e. $\tau_{th_{41}} \gg \tau_{th_{32}}$), $\tau_{th_{32}}$ is taken into consideration to establish the maximum temporal width τ_{el} of the electrical perturbation.

During the current sweep, all the four temperatures are acquired and elaborated to compute the internal thermal resistance of the module Θ_{IN}.

$$\Theta_{IN} = \frac{2 \cdot (T_h - T_c)}{\alpha_S I_{st} \cdot (T_h + T_c) - (q_{em} + q_{abs})} \tag{76}$$

Since even in the worst examined case, i.e. in correspondence of the highest heat fluxes, the temperature drops (77) on the ceramic plates of the module are negligible, it results that $T_c \approx T_2$ and $T_h \approx T_3$.

$$\begin{aligned} \left|\frac{T_3 - T_h}{T_h}\right| &< 0.3\% \\ \left|\frac{T_2 - T_c}{T_c}\right| &< 0.007\% \end{aligned} \tag{77}$$

Making also explicit in (76) the dependence of the remaining parameters on the acquired temperatures, the thermal resistance equation (78) can be rewritten as a function of the measured variables, where $k_{ref} = 1/\Theta_{ref}$ is the thermal conductance of the reference medium. The value of the latter can be fine-tuned sourcing the module with a known electrical power and solving the energy balancing equation $q_{em} - q_{abs} = VI$.

$$\Theta_{IN} = \frac{2 \cdot (T_2 - T_3)^2}{V_{th} I_{st} \cdot (T_2 + T_3) + k_{ref}(T_1 - T_2 - T_3 + T_4)(T_3 - T_2)} \tag{78}$$

At this point, if the following simplifying assumptions are made

- k_{ref} has no associated uncertainty since it is a calibration factor
- the four temperatures have the same uncertainty u_T
- variables are uncorrelated, which results true for all except for I_{st} and V_{th} that are obviously correlated

the uncertainty u_Θ on the estimation of the thermal resistance can be derived applying standard uncertainty propagation formula (79) to (78), i.e. computing the 2-norm of the sensitivity coefficients with respect to each variable x_i times their uncertainty u_{x_i}.

$$u_f = \left\| \sum_{i=1}^{n} \frac{\partial f}{\partial x_i} u_{x_i} \right\|_2 \tag{79}$$

Hence, the thermal resistance uncertainty may be expressed as

$$u_\Theta = \frac{\Theta_{IN}^2}{2\Delta T^2} \left| \bar{T}\left(V_{th} u_{I_{st}} + I_{st} u_{V_{th}}\right) + 2 V_{th} I_{st} u_T \right| \tag{80}$$

from which is mainly observable a clear quadratic inverted trend with respect to $\Delta T = T_3 - T_2$.

IV.2.4 AUTOMATIC TEST

The implemented automatic test procedure performs the above described measurement over a matrix of testing points obtained from the combination of two vectors containing respectively the desired temperatures for the cold side T_c and the desired working ΔT. The whole test is conducted inside a climate chamber (Fig. 59) Discovery Es 250 (DY-250) by Angelantoni Group S.p.A., that forces the cold side of the module to follow the inner ambient temperature.

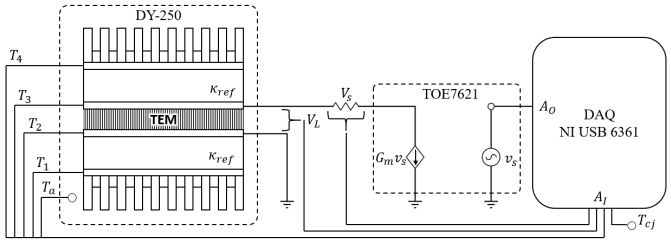

Fig. 59 Automatic measurement setup

All the measured variables, outlined below, are voltage signals acquired at $f_s = 160\,\mathrm{S/s}$ by means of a 16-bit DAQ board X Series USB 6361 by National Instruments

- V_L is the voltage at the TEM terminals
- V_S is the voltage across the shunt resistor R_S
- V_a is the climate chamber ambient temperature measured by means of a TI LM35 sensor
- V_{cj} is the cold junction compensation temperature acquired by means of a TI LM35 sensor
- V_1, V_2, V_3, V_4 are the temperatures of the four layers acquired by means of type J thermocouples

The same DAQ board is also responsible for generating the driving voltage for a 4-quadrant transconductance amplifier Toellner TOE7621 that further supply the module under test.

The entire process of acquisition and generation is handled by a LabVIEW VI that runs a PI controller (Fig. 60) in a closed-loop feedback to drive the module at the desired working conditions. Using the current-to-thermal transfer function estimated in (75), the tuning parameters for the controller have been computed using both the closed-loop Ziegler-Nichols method and the MATLAB® Simulink Auto-tune tool. Although both produce good results, the latter has been chosen since it's able to produce the desired response in a smaller time with less overshoot.

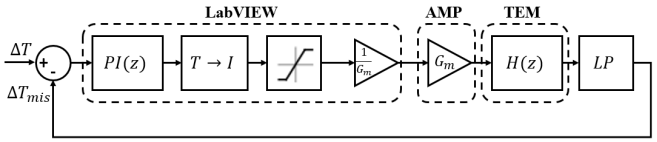

Fig. 60 TEM module control loop

Once steady-state conditions for a given combination of T_c and ΔT are met, i.e. when the following two conditions

$$\begin{aligned} |\mu_{\Delta T} - \Delta T| &< \mu_{th} = 0.15\,°\mathrm{C} \\ \sigma_{\Delta T} &< \sigma_{th} = 0.05\,°\mathrm{C} \end{aligned} \tag{81}$$

are satisfied over 100 s or 16 KS, the LabVIEW VI locks the driving current to the last current value, waits a time equivalent to five thermal time constant ($t_w = 5\tau_{th_{41}}$) for all transient to be finished and switches from Control Mode to Measure Mode.

The measurement procedure (Fig. 61) consists of three sections run in sequence, in which three different current profile are generated:

1. *steady-state*: the last driving current value is applied and the acquired values are used to compute statistics over I_{st}
2. *small-signal*: a small current sine stimulus at 10 Hz is added to I_{st}, with an amplitude equal to the ratio of standard deviation threshold to the static gain of (75)
$$i_{ss} = \frac{\sqrt{2}\sigma_{\mathrm{th}}}{\mathrm{H}(0)}$$
3. *symmetric sweep*: the driving current I_{st} is swept to its symmetric value $-I_{st}$ with a ramp-like signal I_{sw} that is finally switched back to the initial value

The duration t_m of each of the just described current stimulus is set to a value sufficiently minor than the module thermal time

constant $(t_m \leq \tau_{el} \ll \tau_{th})$, producing $n_S = t_m f_S$ acquired samples per section.

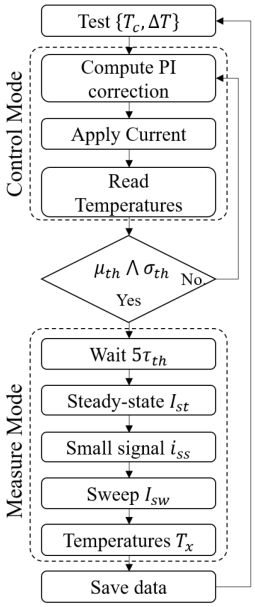

Fig. 61 - Test procedure flowchart

At the end of each test, all raw data (acquired voltage signals) are stored for further elaboration using MATLAB:

- V_L is left as is
- V_S is divided by R_S to obtain I
- T_a and T_{cj} are obtained from respective voltages using the sensitivity $S = 10\ mV/°C$
- T_1, T_2, T_3, T_4 are computed using NIST coefficients and applying software cold-junction compensation
- q_{em} and q_{abs} are computed using (62)
- T_c and T_h are derived by T_2 and T_3 computing the temperature drop on the ceramic layers induced by the computed heat fluxes

Once all the raw signals have been transformed, the three parameters composing the thermoelectric figure of merit Z can be calculated for each working condition $\{T_c, \Delta T\}$:

- V_{th} and R_{IN} are derived using equation (66), applying a linear regression to acquired values $\{I, V_L\}$; α_S is then obtained as ratio of V_{th} to ΔT
- Θ_{IN} is computed using equation (76)

Related papers

- "A Portable Optical Sensor for Sea Quality Monitoring", F. Attivissimo, C. Guarnieri Calò Carducci, A. M. L. Lanzolla, A. Massaro, M. R. Vadrucci, *IEEE Sensors Journal*, 2015, Volume: 15, Issue: 1, Pages: 146 - 153, DOI: 10.1109/JSEN.2014.2340437

- "A MATLAB-Based Method for Designing High-Gain Resonant Transimpedance Amplifiers", F. Adamo, F. Attivissimo, C. Guarnieri Calò Carducci, C. Marzocca, *IEEE Sensors Journal*, 2016, Volume: 16, Issue: 12, Pages: 4828 - 4838, DOI: 10.1109/JSEN.2016.2550659

- "A PWM temperature controller for themoelectric generator characterization", G. Andria, G. Cavone, C. Guarnieri Calò Carducci, M. Spadavecchia, A. Trotta, *IEEE Metrology for Aerospace (MetroAeroSpace)*, Pages: 291 - 296, DOI: 10.1109/MetroAeroSpace.2016.7573229

- "Fast Thermal Characterization of Thermoelectric Modules Using Infrared Camera", F. Attivissimo, A. Di Nisio, C. Guarnieri Calò Carducci, M. Spadavecchia, *IEEE Transaction on Instrumentation and Measurement*, 2016, in press, DOI: 10.1109/TIM.2016.2631818

- "An Extensive Unified Thermo-Electric Module Characterization Method", F. Attivissimo, A. Di Nisio, C. Guarnieri Calò Carducci, M. Spadavecchia, *Sensors 2016*, DOI: 10.3390/s16122114

Chapter V
EXPERIMENTAL VALIDATION

The chlorophyll-*a* sensor described in the previous chapter has gone through a fully metrological characterization. Obtained results are reported in the following divided in two sections referred to the two designing stages. Whereas for the first prototype results are obtained from a characterization process that involved the use of a chlorophyll-*a* sample to derive the sensitivity of the sensor, for the improved sensor the results of the electrical characterization have been simply extended since the measurement setup and related experimental coefficients did not change.

V.1 PRELIMINARY RESULTS

The characterization process of the first prototype was conducted in collaboration with the Department ARPA Puglia (D.A.P. Lecce), which prepared and provided the chlorophyll-*a* samples with a known and certified concentration by means of spectrophotometric methods.

Nevertheless, since spectrophotometry is not able to measure extremely low concentrations such those of in-vivo chlorophyll-*a*, the specimens were preliminarily prepared by filtering some samples of seawater, collected in Porto Cesareo (LE), by means of a 0.2 μm micro-porous Sartorious filter to increase the local concentration of phytoplankton by a known factor. Subsequently, the specimen was placed in acetone for 24 h at 4 °C for the extraction of the chlorophyll-*a* contained inside the microalgae cells. Finally, the chlorophyll-*a* concentration was measured and certified by spectrophotometry.

The characterization results of the sensor are reported in Fig. 62 for 82 concentration values, obtained dissolving 2.5 µl increments in pure water by means of an Eppendorf® Research® 0.5-10 µl pipette. As expected from mathematical relations reported in IV.1.1, a clear linear trend exists between the chlorophyll-*a* concentration and the output voltage.

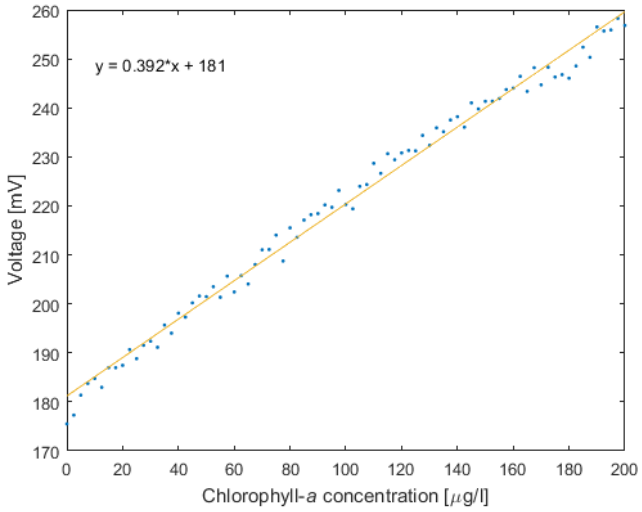

Fig. 62 First prototype test characterization result

This trend was identified by linear regression with a determination coefficient $R^2 = 0.9902$, obtaining a sensor sensitivity of $S_C = 0.392\ \mathrm{mV}/\frac{\mu g}{l}$ and an offset calibration parameter $C \approx 181\ \mathrm{mV}$ that must be subtracted from measured values.

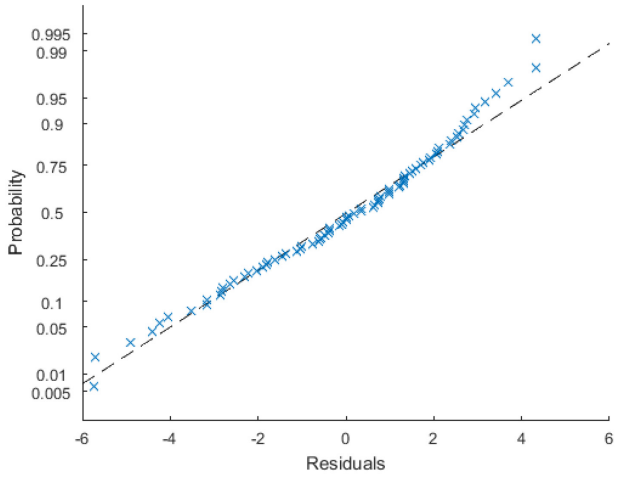

Fig. 63 Normal probability plot of residuals

Once verified the Gaussian distribution of the residuals by means both of visual inspection (Fig. 63) and χ^2 test that reported $p = 33\%$, and the uncorrelation of the same (Fig. 64), the uncertainty referred to the sensitivity u_S and to the calibration factor u_C with coverage factor to 95%, can be expressed [31] as the product of the relative standard deviations for a t-Student distribution with n-2 degrees of freedom:

$$u_S = t_{0.025,n-2} \cdot \sigma_S = t_{0.025,n-2} \cdot \frac{s_{y,x}}{\sqrt{SS_x}} = 1.9900 \cdot 0.0042 =$$
$$= 0.0083 \rightarrow u_{S\%} = 2.11\%$$

$$u_C = t_{0.025,n-2} \cdot \sigma_C = t_{0.025,n-2} \cdot s_{y,x} \sqrt{\left(\frac{1}{n} + \frac{\bar{x}^2}{SS_x}\right)} = 1.9900 \cdot 0.5064 =$$
$$= 1.0078 \rightarrow u_{C\%} = 0.55\%$$

[31] Douglas C. Montgomery, George C. Runger, "Applied Statistics and Probability for Engineers", John Wiley & Sons, Inc., pp. 379-384

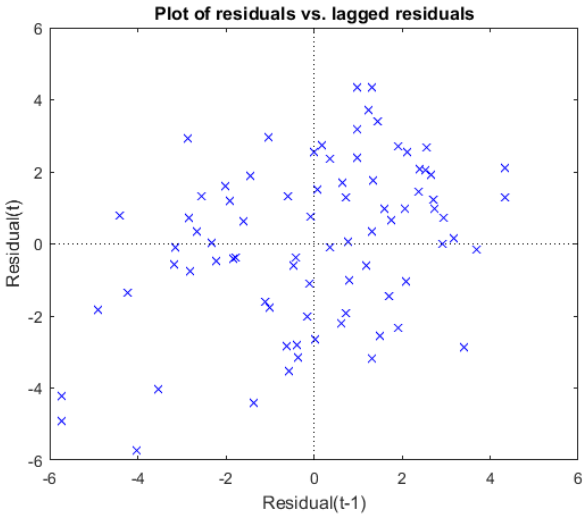

Fig. 64 Plot of residuals vs. lagged residuals

Therefore, the detectivity D may be derived as the ratio of the error standard deviation $s_{y,x}$ (RMSE), to the sensitivity S, leading to a value that is almost three times bigger than the one requested by Italian regulations of 2 μg/l and that requested the electronic improvements described in IV.1.3

$$D = \frac{s_{y,x}}{S_C} = 5.95 \ \frac{\mu g}{l}.$$

V.2 FINAL RESULTS

Using the values of the design parameters found at the end of IV.1.3, a prototype (Fig. 65) of the circuit in Fig. 44 was created to perform the experimental tests. A careful design was adopted to reduce any current leakage using guard rings connected to the Op-Amp non-inverting input, which surround the inverting input and the related connected traces.

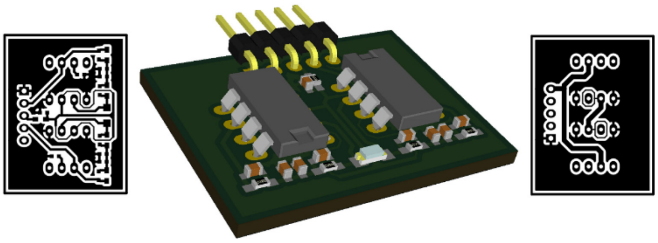

Fig. 65 – 3D model of DUT (center), PCB front (left) and back (right) layer masks.

Since the high circuit impedances are sensitive to RF noise pickup, all the tests described in the following have been performed inside a shielded room that uses the Faraday cage principle to attenuate unwanted RF interferences. In addition, the Device Under Test was also put in a box to protect it from any light source.

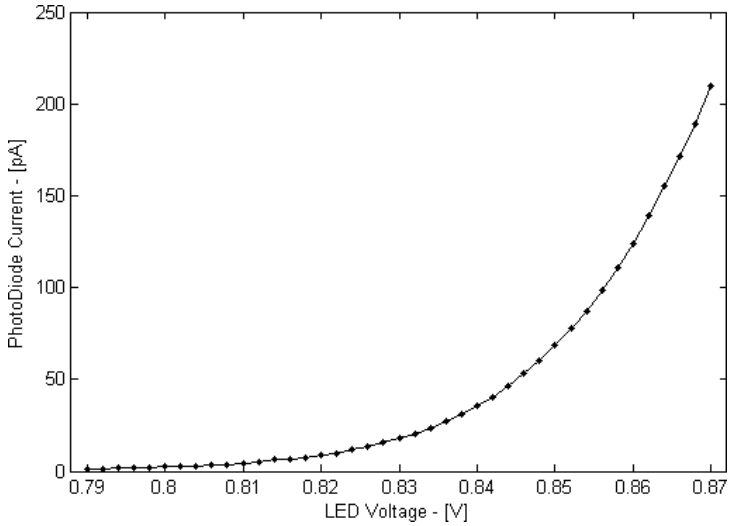

Fig. 66 – Photo-generated current relation with the LED DC driving voltage for the given setup.

The first step consisted in an accurate measurement of the generated photo-current by a DC stimulus signal coming from a high-efficiency red LED placed 5 cm aside from the photodiode and driven by an Agilent 33220A waveform generator. After applying a zero-voltage supply to the two Op-Amps, an Agilent

3458A digital multimeter was connected directly to the photodiode.

The multimeter's resolution of 1 pA in the lowest range (from 1 pA to 100 nA) was sufficient for an accurate measurement, providing the values shown in Fig. 66 after averaging with an integration time of 6 s, corresponding to a Number of Power Line Cycles NPLC $= 300$.

The probe was then removed and a NI USB-6361 X Series DAQ board by National Instruments was used to provide the 5 V power supply and the 2.5 V reference voltage for the non-inverting input of the Op-Amps. By means of a fully differential 16-bit input channel of the DAQ board, 10 s of the resulting output noise for zero input was acquired at the sampling frequency $f_s = 1\,\mathrm{MS/s}$. After computing noise statistics, a standard deviation $V_{N_{rms}} = 12.9\,\mathrm{mV}$ was found and a mean value $O = 314.73\,\mu\mathrm{V}$ (equal to 2 LSBs in the DAQ range [-5, 5]), which is an offset due to asymmetries of the designed differential amplification stage.

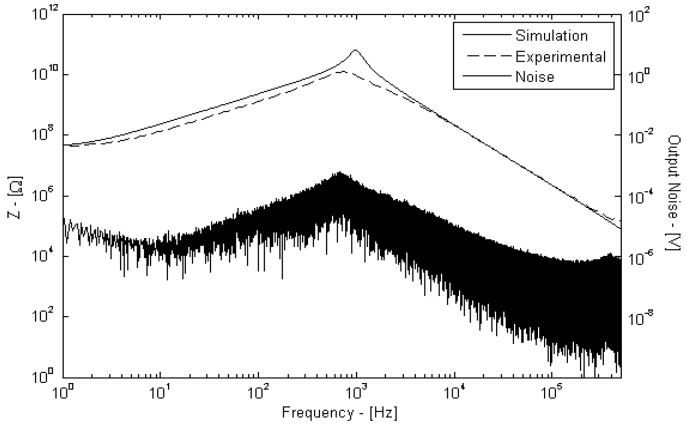

Fig. 67 – Single-side output noise amplitude spectrum (right scale) and comparison of computed/experimental TFs (left scale).

The FFT of the output noise (Fig. 67) is the result of the composition of all noise sources, each one shaped by its input-

output transfer function. A frequency response test was also performed over 200 frequency values using a square wave stimulus. For each frequency, the FFT of the output was computed and the amplitude of the fundamental harmonic was measured, multiplying it by $\pi/2$ to take into account the reduced amplitude with respect to a sine stimulus.

A good matching between measurement results and numerical simulations is found (Fig. 67), but a small deviation of the prototype circuit behavior from the desired resonant frequency at 1 kHz and a consequent reduced gain at the same frequency is present, affecting adversely both S and D in TABLE VII

In all likelihood, since the design process using symbolic solution has shown to have a perfect matching with the one obtained using widely adopted PSpice tools, these differences may be ascribed to parasitic effects or to manufacturing tolerances of the handmade circuit as well as to the quality of adopted passive

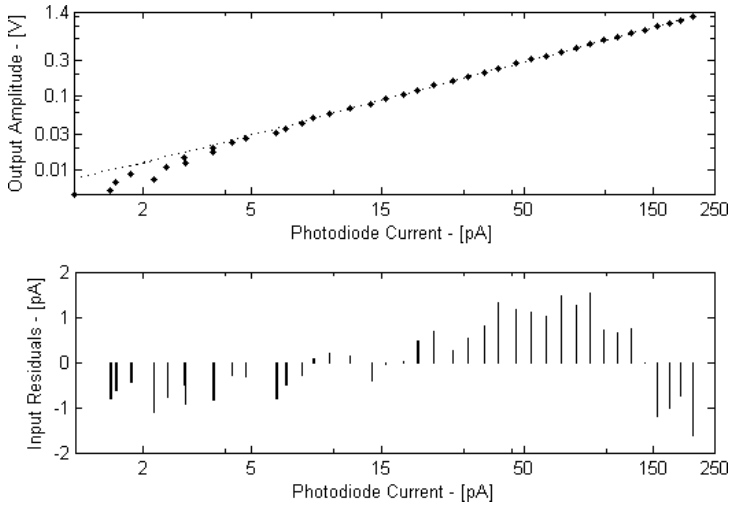

Fig. 68 – Output amplitude due to a modulating square wave at 1 kHz and linear fitting equation (top); input current residuals (bottom).

components or even to load effects of the DAQ input circuitry on the feedback network, all factors that become very critical when dealing with such small currents.

At last, the amplitude of the fundamental harmonic at $f_i = 1$ kHz was measured as a function of the driving voltage of the LED, in the same range considered in Fig. 66. The results, shown in Fig. 68, demonstrate a clear linear relation between the photodiode generated current i_s and the output voltage $v_o = 5.75 \cdot 10^9 \, i_s + 0.0011$. However, the measured peak gain is reduced as compared to the expected one as evinced by Fig. 67, whereas the offset is consistent with the value of the noise floor at the same peak frequency, which is much smaller than rms noise and leads to a detectivity $D = 0.0011/5.75\text{e}9 = 191$ fA @ 1 kHz. This provides an interesting indication of potential performance attainable using frequency domain signal processing techniques.

A final comparison of the resulting parameters with the expected ones is given in TABLE VII. The expected sensitivity and detectivity values are computed respectively in (49) and (48), conversely measured ones are derived using the linear fitting slope and sampled rms noise $V_{N_{rms}}$.

TABLE VII.
EXPECTED AND MEASURED PARAMETERS

Symbol	Description	Expected	Measured
S	Sensitivity [mV/pA] [(a)]	40.1	5.75
D	Detectivity [fA] [(b)]	543	1428
$V_{N_{rms}}$	Rms Output Noise [mV]	34.2	12.9
e_{NL}	Max Non Linearity Error [pA]	-	1.626

[(a)] Sensitivity refers to a square wave stimulus at 1 kHz with $\delta = 50\%$

[(b)] Computed with respect to corrected gains using $D = V_{N_{rms}} / \left(\frac{\pi}{2} S\right)$

As noted above, since the measurement setup did not change but only the involved electronics, the current values in the

characterization of the final prototype were converted in the equivalent chlorophyll-*a* concentration values using a coefficient $K = 0.812\ \frac{\mu g}{l}/\mathrm{pA}$ derived from the first prototype.

The characterization result for 41 intensity values of the light stimulus, reported in Fig. 69, shows extremely performing values ($G' = 9\ \mathrm{mV/pA} \approx 200\ \mathrm{dB\Omega}$), achieved exclusively with the use of a single amplification stage and using largely and commonly available passive components. The trend was identified by linear regression with a determination coefficient $R^2 = 0.9998$, obtaining a sensor sensitivity referred to photo-induced current of $S_A = 5.745\ \mathrm{mV/pA}$ and a chlorophill-*a* referred one $S'_C = {G'}/{G}\, S_C \approx 7\ \mathrm{mV}/\frac{\mu g}{l}$, whereas the offset calibration parameter is almost negligible.

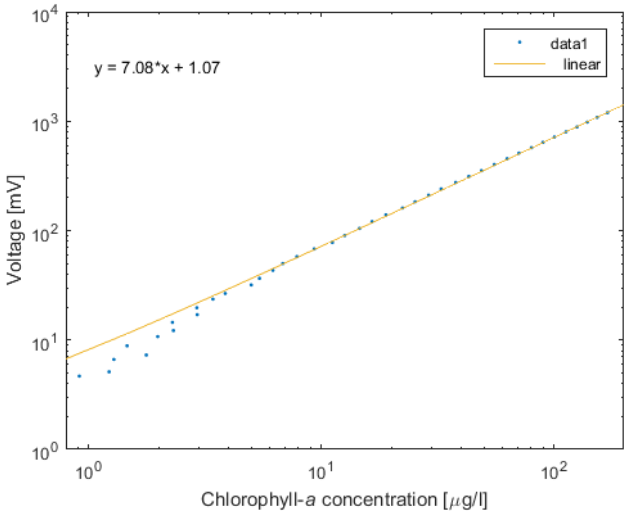

Fig. 69 – Final prototype test characterization result

Once verified the Gaussian distribution of the residuals by means both of visual inspection (Fig. 70) and χ^2 test that reported a $p = 33.1\%$, and the uncorrelation of the same, the uncertainty referred to the sensitivity u_S and to the calibration factor u_C with

coverage factor to 95%, can be expressed as the product of the relative

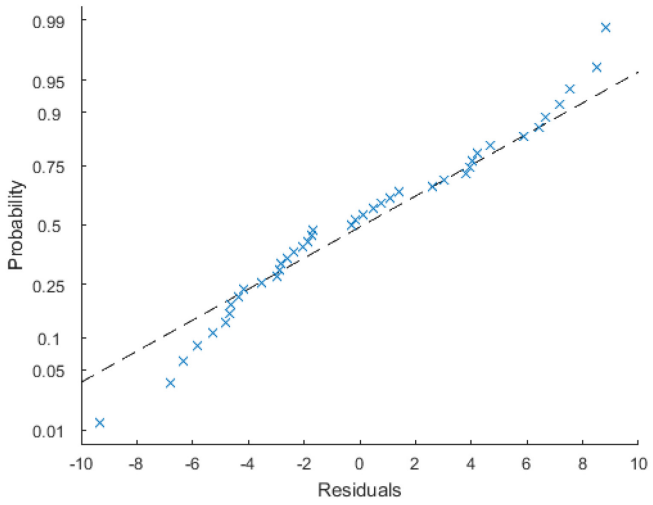

Fig. 70 Normal probability plot of residuals

standard deviations for a t-Student distribution with n-2 degrees of freedom:

$$u_S = t_{0.025,n-2} \cdot \sigma_S = t_{0.025,n-2} \cdot \frac{s_{y,x}}{\sqrt{SS_x}} = 2.0226 \cdot 0.0159 =$$

$$= 0.0322 \rightarrow u_{S\%} = 0.45\%$$

$$u_C = t_{0.025,n-2} \cdot \sigma_C = t_{0.025,n-2} \cdot s_{y,x} \sqrt{\left(\frac{1}{n} + \frac{\bar{x}^2}{SS_x}\right)} = 2.0226 \cdot 0.9558 =$$

$$= 1.9334$$

Computing the detectivity D as the ratio of the error standard deviation $s_{y,x}$ (RMSE) to the sensitivity S, a new estimation may be derived

$$D = \frac{s_{y,x}}{S_C} = 0.673 \ \frac{\mu g}{l}$$

that is expected to be further reduced by improving the quality of components used in the amplification stage.

CONCLUSIONS

The proposed work has led to a design framework to be used to implement Wireless Sensor Networks for coastal monitoring in oceanographic applications. This framework was defined in all aspects, starting from the definition of the network architecture, going through the required standards that are able to provide high versatility to transducer networks, both in terms of a unified command language and in the flexibility of reconfigurable networks.

The network coverage and its robustness in harsh environments, have been deeply investigated both using an analytical approach and by means of numerical simulations, demonstrating the feasibility of the proposed architecture.

Although many biological and non-biological indicators are used in oceanographic applications, the focus of the thesis was on the detection and the measurement of the chlorophyll density in seawater, since its concentration is the only parameter recognized by Italian regulations as trophic status indicator of seawater.

A novel electronic design technique was used to implement a low-cost sensor for in-vivo chlorophyll detection, using only one signal amplification stage with extremely high gain. The sensor was fully characterized from the metrological point of view confirming its ability to measure chlorophyll concentration values such as those reported in regulations.

A hardware architecture for energy self-sufficient buoys is finally presented. Its power consumption was deeply characterized and the possibility for energy harvesting by means of thermoelectric modules was fully investigated.

LIST OF PAPERS

INTERNATIONAL JOURNALS

- "A Portable Optical Sensor for Sea Quality Monitoring", F. Attivissimo, C. Guarnieri Calò Carducci, A. M. L. Lanzolla, A. Massaro, M. R. Vadrucci, *IEEE Sensors Journal*, 2015, Volume: 15, Issue: 1, Pages: 146 - 153, DOI: 10.1109/JSEN.2014.2340437

- "A Smart Sensor Network for Sea Water Quality Monitoring", F. Adamo, F. Attivissimo, C. Guarnieri Calò Carducci, A. M. L. Lanzolla, *IEEE Sensors Journal*, 2015, Volume: 15, Issue: 5, Pages: 2514 - 2522, DOI:10.1109/JSEN.2014.2360816

- "A MATLAB-Based Method for Designing High-Gain Resonant Transimpedance Amplifiers", F. Adamo, F. Attivissimo, C. Guarnieri Calò Carducci, C. Marzocca, *IEEE Sensors Journal*, 2016, Volume: 16, Issue: 12, Pages: 4828 - 4838, DOI: 10.1109/JSEN.2016.2550659

- "High Dynamic Range Power Consumption Measurement in Microcontroller-Based Applications", A. Di Nisio, T. Di Noia, C. Guarnieri Calò Carducci, M. Spadavecchia, *IEEE Transactions on Instrumentation and Measurement*, 2016, Volume: 65, Issue: 9, Pages: 1968 - 1876, DOI:10.1109/TIM.2016.2549818

- "Fast Thermal Characterization of Thermoelectric Modules Using Infrared Camera", F. Attivissimo, A. Di Nisio, C. Guarnieri Calò Carducci, M. Spadavecchia, *IEEE Transaction on Instrumentation and Measurement*, 2016, in press, DOI: 10.1109/TIM.2016.2631818

- "An Extensive Unified Thermo-Electric Module Characterization Method", F. Attivissimo, A. Di Nisio, C. Guarnieri Calò Carducci, M. Spadavecchia, Sensors 2015, DOI: 10.3390/s16122114

- "An improved DAQ based method for ferrite characterization", F. Attivissimo, R. Giannetti, C. Guarnieri Calò Carducci, Mirko

Marracci, B. Tellini, submitted to *IEEE Transaction on Instrumentation and Measurement*

NATIONAL JOURNALS

- "Il Fluorimetro e Turbidimetro low-cost", F. Attivissimo, C. Guarnieri Calò Carducci, G. Cavone, A. M.L. Lanzolla, TUTTO MISURE, vol. XVII, p. 181-184, ISSN: 2038-6974

INTERNATIONAL CONFERENCE

- "Monitoring Apulia region coastline: A case study", F. Adamo, F. Attivissimo, C. Guarnieri Calò Carducci, A. M. L. Lanzolla, 2014 *IEEE Workshop on Environmental Energy and Structural Monitoring Systems (EESMS)*, pp. 1 - 5, DOI:10.1109/EESMS.2014.6923270

- "New Technologies and Perspectives for Laboratory Practices in Measurement Science", F. Adamo, F. Attivissimo, G. Cavone, C. Guarnieri Calò Carducci, A. M. L. Lanzolla, 2015 *IEEE International Instrumentation and Measurement Technology Conference (I2MTC)* Proceedings, pp. 1 - 6, DOI:10.1109/I2MTC.2015.7151230

- "Design of a low cost multipurpose wireless sensor network", A. Di Nisio, T. Di Noia, C. Guarnieri Calò Carducci, M. Spadavecchia, *2015 IEEE International Workshop on Measurements & Networking (M&N)*, pp. 1 - 6, DOI: 10.1109/IWMN.2015.7322986

- "A PWM temperature controller for themoelectric generator characterization", G. Andria, G. Cavone, C. Guarnieri Calò Carducci, M. Spadavecchia, A. Trotta, *2016 IEEE Metrology for Aerospace (MetroAeroSpace)*, Pages: 291 - 296,
DOI: 10.1109/MetroAeroSpace.2016.7573229

NATIONAL CONFERENCE

- Adamo F, Attivissimo F, Guarnieri Calò Carducci C., Lanzolla AML, Trotta A (2015). "Nuove pratiche e tecnologie educative per il laboratorio misure". In: XXXII Congresso Nazionale GMEE. p. 67-68, ISBN: 9788891612144, Lecco, 10-12 Settembre

- Andria G, Adamo F, Guarnieri Calò Carducci C., Lanzolla Aml, (2015). "Rete di sensori per il monitoraggio della qualità dell'acqua marina". In: XXXII Congresso Nazionale GMEE. p. 123-124, ISBN: 9788891612144, Lecco, 10-12 Settembre

- Adamo F.; Cavone G.; Di Nisio A.; Guarnieri Calò Carducci C.; Savino M.; Spadavecchia M. (2106). "Misurazione accurata ad ampia banda del consumo di energia di nodi wireless e di sistemi a microcontrollore" In: Atti del XXXIII Cong. Nazionale 2016 GMEE. p. 129-130, ISBN: 978-88-940453-6-9, Benevento, 19-21 settembre 2016

- Attivissimo F., Andria G., Cavone G., Guarnieri Calò Carducci C, Spadavecchia M., Trotta A. (2016). "Controllo della temperatura per la caratterizzazione di moduli termoelettrici". In: Atti del XXXIII Cong. Nazionale 2016 GMEE. p. 171-172, ISBN: 978-88-940453-6-9, Benevento, 19-21 settembre 2016

- Attivissimo F., Guarnieri Calò Carducci C., Marzocca C. (2016). "Un metodo efficiente basato su Matlab per la progettazione di amplificatori in transinpedenza risonanti ad elevato guadagno". In: Atti del XXXIII Cong. Nazionale 2016 GMEE. p. 215-216, ISBN: 978-88-940453-6-9, Benevento, 19-21 settembre 2016

- Adamo F., Attivissimo F., Guarnieri Calò Carducci C., Lanzolla A. (2016). "Misura e monitoraggio della qualità dell'acqua marina". In: Atti del XXXIII Cong. Nazionale 2016 GMEE. p. 307-315, ISBN: 978-88-940453-6-9

BIBLIOGRAPHY

[1]. The European Union Water Framework Directive: Integrated River Basin Management for Europe, WFD 2000/60/IEC

[2]. Review of the methods, criteria and limit values for the assessment of Eutrophication as developed in the framework of the Intercalibration Exercise of the MED GIG Water Framework Directive 2000/60 EC, UNEP(DEPI)/MED WG.365/Inf.7, 4 November 2011, p. 29

[3]. Decreto Ministeriale 260/2010, Tabella 4.3.1: www.reteambiente.it/repository/normativa/14566all1_2.pdf

[4]. http://www.lagazzettadelmezzogiorno.it/news/home/568591/-litorale-barese--l-alga-tossica-fa-gia-prime-vittime.html

[5]. A.R.P.A. Puglia, Monitoraggio Ostreopsis: http://www.arpa.puglia.it/web/guest/monitoraggiostreopsis

[6]. OECD LEED Policy Review on: Sustainable Tourism and Local Development in Apulia Region, 2010

[7]. IEEE, The Institute of Electrical and Electronics Engineers, "IEEE Standard for a Smart Transducer Interface for Sensors and Actuators - Transducer to Microprocessor Communication Protocols and Transducer Electronic Data Sheet (TEDS) Formats, IEEE Standard 1451.2"–1997, Inc., NY, 1997.

[8]. D. Wobschall "Networked sensor monitoring using the universal IEEE 1451 Standard" Instrumentation & Measurement Magazine, IEEE, vol. 11, no. 2, pp 18-22, 2008.

[9]. J. Wiczer, "Smart Interfaces for Sensors", Proceeding Sensor Expo – Smart Sensor Session, Chicago, IL, 2001

[10]. J. Popelka, P. Paces, "Performance of smart sensors standards for aerospace applications", Electrical Review, vol. 88, pp. 229-232, 2012.

[11]. L.de Montera, M. Jouini, S. Verrier, S. Thiria, M. Crepon, "Multifractal analysis of oceanic chlorophyll maps remotely sensed from space", Ocean Science Discussions, Vol. 7 no.2, pp.219-229, 2011.

[12]. European Parliament, “Directive 2000/60/EC of the european parliament and of the council establishing a framework for the community action in the field of water policy,” CELEX-EUR Official J., vol. 327, pp. 1–72, Dec. 2000.

[13]. Theodore S. Rappaport, “Wireless Communication: Principles and Practice”, Prentice Hall, 2 edition, January 10, 2002.

[14]. Lee, W. C. Y., “Mobile Communications Engineering”, McGraw Hill Publications, New York, 1985.

[15]. R. C. Gonzalez, R. E. Woods , “Digital Image Processing,” 3rd ed, Prentice Hall, 2008.

[16]. F. Attivissimo, A. Di Nisio, A.M.L Lanzolla, M. Paul, "Feasibility of a photovoltaic–thermoelectric generator: performance analysis and simulation results," IEEE Trans. on Instr. & Meas., vol.64, no.5, pp.1158,1169, May 2015.

[17]. Joseph R. Lakowicz “Principles of Fluorescence Spectroscopy” Springer, 2006.

[18]. W. Kester, “Practical Design Techniques for Sensor Signal Conditioning”, Analog Devices Technical Reference Books, vol. 5, pp. 1-40, 1999.

[19]. W. Kester, “Practical Design Techniques for Sensor Signal Conditioning”, Analog Devices Technical Reference Books, vol. 5, pp. 1-40, 1999

[20]. S. Rosenstark, “Feedback amplifier principles”, Macmillan Press USA, 1986

[21]. Keithley, “Low Level Measurements Handbook”, Keithley Instruments Inc, 2004

[22]. C. Sanchez-Lopez, E. Tielo-Cuautle, “Behavioral model generation for symbolic analysis of analog integrated circuits”, ISSCS 2005, doi: 10.1109/ISSCS.2005.1509920

[23]. E. Tlelo-Cuautle, L.A. Sarmiento-Reyes, “A Pure Nodal-Analysis Method Suitable For Analog Circuits Using Nullors”, Journal of Applied Research and Technology, vol. 1, num. 3, october, 2003, pp. 235-247

[24]. E. Tlelo-Cuautle, J. Cid-Monjaráz, “Computing symbolic transfer functions from SPICE files using nullors”, Proceedings of WSEAS International Conferences, 2002, Mexico, pp. 1641-1646

[25]. Norms for Signal and Systems, online: http://www.cds.caltech.edu/~macmardg/courses/cds110b/dft/dft92-ch2.pdf

[26]. K. Hee Seok, L. Weishu, C. Gang, C. Ching-Wu, R. Zhifeng, “Physics Relationship between thermoelectric figure of merit and energy conversion efficiency”, Proc Natl Acad Sci U S A. 2015 Jul 7; 112(27): 8205–8210. doi: 10.1073/pnas.1510231112

[27]. R. J. Buist, “Methodology for testing thermoelectric materials and devices”, in CRC Handbook of Thermoelectrics, D. M. Rowe, Ed. Boca Raton, FL: CRC, 1995, pp. 189–209.

[28]. S. Lineykin and S. Ben-Yaakov, "Modeling and Analysis of Thermoelectric Modules," in IEEE Transactions on Industry Applications, vol. 43, no. 2, pp. 505-512, March-april 2007. doi: 10.1109/TIA.2006.889813

[29]. T. A. Ajiwiguna, A. Ismardi, S. Y. Kim, “Measurement System for Thermoelectric Module”, IEEE I2MTC 2015 Proceedings, 2015

[30]. Douglas C. Montgomery, George C. Runger, “Applied Statistics and Probability for Engineers”, John Wiley & Sons, Inc., pp. 379-384

[31]. Douglas C. Montgomery, George C. Runger, “Applied Statistics and Probability for Engineers”, John Wiley & Sons, Inc., pp. 379-384